UNIVERSITÀ DEGLI STUDI DI ROMA
"TOR VERGATA"

Facoltà di Scienze Matematiche, Fisiche e Naturali

Tesi di Dottorato di Ricerca in Fisica

Forward-backward asymmetry measurement in $pp \rightarrow Z/\gamma^* \rightarrow \mu^+\mu^-$ events at $\sqrt{s} = 7$ TeV with the ATLAS experiment at the LHC

Candidato:
GIORDANO CATTANI

Relatore:
Prof.ssa ANNA DI CIACCIO

Coordinatore:
Prof. MAURIZIO DE CRESCENZI

Ciclo XXIV

A. A. 2010/2011

to my family

Contents

List of Tables

List of Figures

Introduction

The Large Hadron Collider (LHC) at CERN in Geneva (Switzerland) is presently the highest energy proton-proton accelerator. It has been designed to answer many open questions in the field of Elementary Particle Physics. In November 2009 LHC started to deliver the first collisions at the center of mass energy of 900 GeV. In 2010 and 2011 the accelerator was running at a collision energy of 7 TeV and it has delivered a total integrated luminosity of more than 5 fb^{-1}.

Four main experiments are currently taking data at LHC: ALICE [1], LHCb [2], ATLAS [3] and CMS [4]. The ALICE experiment is specialized in the study of heavy ion collisions (Pb-Pb), LHCb is a single forward arm experiment studying mainly the properties of beauty quarks while ATLAS and CMS are general purpose detectors with an almost 4π acceptance and therefore suitable for a wider physics program. These two experiments have already published plenty of results, "rediscovering" the Standard Model (SM) of Particle Physics [5–7] and, at the same time, starting the search for New Physics signatures.

The SM is a quantum field theory that describes all elementary particles and their interactions except gravity. It includes the $SU(3)_C$ color symmetry of strong interaction and the $SU(2)_W \times U(1)_Y$ weak isospin and hypercharge symmetry of the electroweak interaction. A fundamental parameter of the

model is the Weinberg or weak mixing angle, θ_W, and its value varies as a function of the momentum transfer, Q^2. This is a key prediction of the electroweak theory. In practice, the quantity $\sin^2\theta_W$ is more frequently used. At leading order it can be measured by the ratio between the W and Z boson masses, namely $\sin^2\theta_W = 1 - \left(\frac{m_W}{m_Z}\right)^2$. If higher-order radiative (either purely electromagnetic and electroweak) corrections to the Born-level neutral current are taken into account, an effective weak mixing angle, $\sin^2\theta_{eff}$, is obtained. The most precise measurement of this quantity has been carried out in electron-positron collider experiments at the LEP collider [8] and in experiments at the Tevatron $p\bar{p}$ accelerator [9].

Despite being the most successful theory of Particle Physics to date, the SM looks still incomplete. There are a number of open questions for which it does not give an adequate explanation: e.g. origin of mass, matter anti-matter asymmetry, dark matter and dark energy existence, neutrino oscillations and, as previously mentioned, gravity. In order to give a possible answer to these open questions, many theoretical models extending the SM have been proposed.

The search and the possible discovery of the Higgs Boson, a crucial element of the Standard Model explaining the origin of mass, and the search for physics Beyond Standard Model (BSM) represent the most important physics goals of the ATLAS experiment. Many are the possible signatures in which New Physics could be observed: the measurement of asymmetries represents one of the most promising [10].

The Drell-Yan process in which $q\bar{q}$ annihilate to intermediate γ^* or Z vector bosons that decay into lepton pairs (e.g. $\mu^+\mu^-$) is particularly useful in

searching for new interactions at large momentum transfers, $Q^2 = m_{ll}^2$, where m_{ll}^2 is the invariant mass of the lepton pair.

Drell-Yan lepton pairs, produced in $q\bar{q}$ annihilations, display a forward-backward asymmetry (A_{fb}) due to the interference between photon and Z boson exchange. The A_{fb} would be significantly modified by new resonances (e.g. additional heavier Z' boson) or new interactions at large mass scales, giving a sizable evidence of these processes with respect to, for example, the signal that would be observed in the di-lepton invariant mass spectrum.

This thesis is focused on the measurement of the forward-backward asymmetry with the ATLAS experiment, using $pp \to Z/\gamma^* \to \mu^+\mu^-$ events at $\sqrt{s}$ = 7 TeV. The analysis searches for the decays of the Z/γ^* bosons into two muons, since this process provides a relatively clean signature which can be easily discriminated from background processes.

In Chap. 1 a basic description of the SM theory and a detailed insight on the A_{fb} measurement is given. Chap. 2 and Chap. 3 are dedicated to the description of the LHC accelerator and of the ATLAS detector respectively. Chap. 4 is focused on the data and Monte Carlo (MC) samples used in this analysis and on the Z/γ^* candidate selection criteria. In Chap. 5 the muon performance (trigger and reconstruction efficiencies) for high-p_T muons, which are relevant for the A_{fb} measurement, are reviewed. In Chap. 6 a detailed description of the analysis to measure the A_{fb} is given. This work, to which I am giving the major contribution, represents the first study of the Z forward-backward asymmetry in the muon channel in the ATLAS experiment. From the fit of the A_{fb} as a function of the di-muon mass around the Z pole, after a further correction to extend the A_{fb} measurement outside the fiducial vol-

ume defined by the Z/γ^* candidates event selection, a direct measurement of $\sin^2\theta_{eff}$ could be performed. I have discussed this method that I am presently using to extract the weak mixing angle in the last paragraph of Chap. 6.

Chapter 1

Theoretical Background

1.1 The Standard Model of Particle Physics

One of the main goals of particle physics is to understand what matter is made of and what are the forces through which matter interacts. Our current understanding of the fundamental forces is contained in the description of the gravitational, the strong, the weak and the electromagnetic interactions. The last three forces are transmitted by specific fields or particles which are equivalent concepts in relativistic quantum field theory.

In the 1960s, S.L. Glashow, A. Salam and S. Weinberg unified the electromagnetic and weak interactions into the electroweak theory [11], which, together with Quantum Chromodynamics (the theory of the strong interaction) [12], forms the Standard Model (SM) of particle physics. The SM is a quantum field theory that includes $SU(3)_C$ color symmetry of strong interaction and $SU(2)_W \times U(1)_Y$ weak isospin doublet and hypercharge symmetry of electroweak interaction. The SM provides a very elegant theoretical framework

and it has successfully passed very precise tests [13].

Both electroweak and QCD theories are gauge field theories, meaning that they model the forces between fermions by coupling them to bosons which mediate the forces. The eight massless gluons, g_α, mediate strong interactions among quarks. The massless photon, γ, is the exchange particle in electromagnetic interactions, and the three massive weak bosons, $W^\pm$ and Z, are the corresponding intermediate bosons that mediate the weak interaction. Tab. 1.1 summarizes the fundamental forces and the properties of their gauge bosons [14].

Force	**Boson Name**	**Symbol**	**Charge ($\|e\|$)**	**Spin**	**Mass (GeV/c^2)**
Strong	Gluon	g	0	1	0
Electromagnetic	Photon	γ	0	1	0
Weak	W-boson	$W^\pm$	±1	1	80.423 ± 0.039
	Z-boson	Z^0	0	1	91.1876 ± 0.0021
Gravitational	Graviton	G	0	2	0

Table 1.1: Fundamental forces and the corresponding gauge bosons

Matter is organized in lepton and quark doublets, with a total of six leptons and six quarks. The six leptons are electron (e), muon (μ), tau (τ) and the corresponding neutrinos; the six quarks are up, down, charm, strange, top and bottom quarks. These six leptons and six quarks are fermions of spin s = 1/2 and can be grouped into three generations (also called families) as shown in Tab. 1.2.

Generation	Leptons (spin = $\frac{1}{2}$)		
	Flavors	**Charge ($\|e\|$)**	**Mass (MeV/c^2)**
1	e	-1	0.511
	ν_e	0	$< 3\times10^{-6}$
2	μ	-1	105.66
	ν_μ	0	< 0.19
3	τ	-1	1776.99 ± 0.29
	ν_τ	0	< 18.2
Generation	Quarks (spin = $\frac{1}{2}$)		
	Flavors	**Charge ($\|e\|$)**	**Mass (MeV/c^2)**
1	u	+2/3	1.5 - 5
	d	-1/3	3 - 9
2	c	+2/3	$(1.0 - 1.4) \times10^3$
	s	-1/3	60 - 170
3	t	+2/3	$(178.0 \pm 4.3) \times10^3$
	b	-1/3	$(4.0 - 4.5) \times10^3$

Table 1.2: Generations of elementary particles.

1.2 The Forward-Backward Asymmetry

Because the weak interactions violate parity, as will be further discussed in 1.2.1, collider processes that can involve the weak interactions typically exhibit asymmetries in the distributions of the final-state particles. These asymmetries are typically sensitive to the difference in the interaction between particles and antiparticles, or between left-handed and right-handed particles. They can thus be used as a sensitive measurement of differences in interaction strength and/or to distinguish a small asymmetric signal from a large but symmetric background.

1.2.1 Parity Violation in Electroweak Interaction

Weak charged current interaction is parity-violating and connects, taking the first generation of leptons as an example, the left-handed (LH) states of neutrino and electron. On the other hand the electromagnetic interaction is parity-

conserving and involves both LH and right-handed (RH) states of the electron. Hence we have to assign the lepton states to a LH doublet and a RH singlet, as follows

$$\begin{aligned} R_e &= (e)_R \\ L_e &= \begin{pmatrix} \nu_e \\ e^- \end{pmatrix}_L \end{aligned} \tag{1.2.1}$$

where the LH and RH components of a field Ψ are defined by

$$\begin{aligned} \Psi_R &= \frac{1+\gamma_5}{2}\Psi \\ \Psi_L &= \frac{1-\gamma_5}{2}\Psi \end{aligned} \tag{1.2.2}$$

where γ_5 is the chirality operator. In Tab. 1.3 the LH doublets and RH singlets for each lepton generation are reported.

Generation	**Parity**	
	LH	**RH**
1	$\begin{pmatrix} \nu_e \\ e^- \end{pmatrix}_L$	$(e)_R$
2	$\begin{pmatrix} \nu_\mu \\ \mu^- \end{pmatrix}_L$	$(\mu)_R$
3	$\begin{pmatrix} \nu_\tau \\ \tau^- \end{pmatrix}_L$	$(\tau)_R$

Table 1.3: LH and RH states for each lepton family.

The charged currents are thus defined as

$$J^+_\mu = \bar{\nu}\gamma_\mu \frac{1-\gamma_5}{2} e = \bar{\nu}_L \gamma_\mu e_L = \bar{\Psi}_L \gamma_\mu \tau^+ \Psi_L \tag{1.2.3}$$

and

$$J_\mu^- = \bar{e}\gamma_\mu \frac{1-\gamma_5}{2}\nu = \bar{e}_L\gamma_\mu\nu_L = \bar{\Psi}_L\gamma_\mu\tau^-\Psi_L \tag{1.2.4}$$

where $\tau^\pm = \frac{1}{2}(\tau_1 \pm i\tau_2)$ are the Pauli operators suitable for describing I = 1/2 systems:

$$\tau^+ = \begin{pmatrix} 0 & 1 \\ 0 & 0 \end{pmatrix}, \qquad \tau^- = \begin{pmatrix} 0 & 0 \\ 1 & 0 \end{pmatrix}$$

and γ_μ are Dirac matrices. The neutral current will be

$$J_\mu^{(3)} = \bar{\Psi}_L\gamma_\mu\frac{1}{2}\tau_3\Psi_L = \bar{\Psi}\gamma_\mu\frac{1+\gamma_5}{2}I_3\Psi = \frac{1}{2}(\bar{\nu}_L\gamma_\mu\nu_L - \bar{e}_L\gamma_\mu e_L) \tag{1.2.5}$$

We have thus constructed an "isospin" triplet of weak currents,

$$J_\mu^{(i)} = \bar{\Psi}_L\gamma_\mu\frac{1}{2}\tau_i\Psi_L, \qquad \text{with } i = 1,\, 2,\, 3 \tag{1.2.6}$$

The electroweak theory is the unified description of two fundamental interactions: electromagnetic interaction and the weak interaction. These two forces appear very differently at low energies, but above the unification energy, at the order of 100 GeV, they would merge into a single electroweak interaction which has the important feature to be renormalizable [15] [16]. This feature gives the theory a predictive power. It predicts the existence of neutral currents and W and Z gauge bosons. In 1973 Weak Neutral Currents (WNC) were discovered simultaneously by two neutrino experiments at CERN [17] and Fermilab [18], and within a few years the first measurements of $\sin^2\theta_{eff}$ was made [19]. In 1983 the discovery of the W and Z gauge bosons [20] allowed the measurement of their masses with great precision and consequently a stringent

comparison of the electroweak theory with experimental results.

The electroweak interaction is based on an SU(2) group of "weak isospin", T, and a U(1) group of "weak hypercharge", Y. The model consists of an isotriplet of vector fields W^i_μ coupled with strength g to the weak isospin current J^i_μ together with a single vector field B_μ coupled to the weak hypercharge current J^Y_μ with strength conventionally taken to be $g'/2$. The basic electroweak interaction is the product of the fermion currents with the fields, and it is therefore [21] [22] [23]

$$L = -igJ_\mu W_\mu + -i\frac{g'}{2}J^Y_\mu B_\mu \tag{1.2.7}$$

where J_μ and J^Y_μ represent the isospin and the hypercharge currents of the fermions respectively and g and g' are the couplings of fermions to W_μ and B_μ. If we define the weak hypercharge as Y = 2(Q - T_3), where Q is the electric charge and T_3 is the third component of the weak isospin, then the corresponding relation among the current is

$$J^Y_\mu = 2\left(J^{em}_\mu - J^{(3)}_\mu\right) \tag{1.2.8}$$

where J^{em}_μ is the electromagnetic current, coupling to the charge Q and $J^{(3)}_\mu$ is the third component of the isospin current J_μ.

The Lagrangian is thus

$$\begin{aligned} L &= -igJ_\mu W_\mu - i\frac{g'}{2}J_\mu^Y B_\mu \\ &= -ig\left(J_\mu^{(1)}W_\mu^{(1)} + J_\mu^{(2)}W_\mu^{(2)}\right) - ig\left(J_\mu^{(3)}W_\mu^{(3)}\right) \\ &\quad -ig'\left(J_\mu^{em} - J_\mu^{(3)}\right)B_\mu \end{aligned} \tag{1.2.9}$$

where $W_\mu^{(i)}$ with $i = 1, 2, 3$ are the weak bosons of the $\mathrm{SU}(2)_L$ group and B_μ is the hypercharge boson of the $\mathrm{U}(1)_Y$ group. The physical bosons consists of the charged $W_\mu^\pm$ and the neutrals Z_μ and A_μ particles. The latter are taken as linear combination of $W_\mu^{(3)}$ and B_μ. Thus if we set

$$W_\mu^\pm = \frac{1}{\sqrt{2}}\left(W_\mu^{(1)} \mp iW_\mu^{(2)}\right) \tag{1.2.10}$$

then

$$\begin{aligned} L &= \frac{g}{\sqrt{2}}\left(J_\mu^- W_\mu^+ + J_\mu^+ W_\mu^-\right) + J_\mu^{(3)}\left(gW_\mu^{(3)} - g'B_\mu\right) + J_\mu^{em}g'B_\mu \\ &= \frac{g}{\sqrt{2}}\left(J_\mu^- W_\mu^+ + J_\mu^+ W_\mu^-\right) + \frac{g}{\cos\theta_W}\left(J_\mu^{(3)} - \sin^2\theta_W J_\mu^{em}\right)Z_\mu + g\sin\theta_W J_\mu^{em}A_\mu \\ &= L_{CC} + L_{NC} + L_{em} \end{aligned} \tag{1.2.11}$$

where $J_\mu^\pm = J_\mu^{(1)} \pm iJ_\mu^{(2)}$ and $g'/g = \tan\theta_W$.

This equation shows that the interaction contains the weak charge-changing current

$$L_{CC} = \frac{g}{\sqrt{2}}\left(J_\mu^- W_\mu^+ + J_\mu^+ W_\mu^-\right) \tag{1.2.12}$$

a weak neutral current

$$L_{NC} = \frac{g}{\cos\theta_W}\left(J_\mu^{(3)} - \sin^2\theta_W J_\mu^{em}\right) Z_\mu \tag{1.2.13}$$

and the electromagnetic current

$$L_{em} = g\sin\theta_W J_\mu^{em} A_\mu \tag{1.2.14}$$

for which we know the coupling to be e. Hence

$$e = g\sin\theta_W \tag{1.2.15}$$

The angle θ_W is called weak mixing angle (or Weinberg angle).

In Vector and Axial-Vector (V - A) theory, the charged current matrix element is [24]

$$|M| = \frac{G}{\sqrt{2}}\left[\bar{e}\gamma_\mu\left(1-\gamma_5\right)\nu\right]\left[\bar{\nu}\gamma_\mu\left(1-\gamma_5\right)e\right] \tag{1.2.16}$$

where G is the Fermi coupling constant. Compared with the expressions 1.2.3, 1.2.4, 1.2.11, in the limit of $q^2 \ll m_W^2$, we have

$$|M| = \left(\frac{g}{\sqrt{2}}\right)^2 \frac{1}{m_W^2}\left[\bar{e}\gamma_\mu\frac{1-\gamma_5}{2}\nu\right]\left[\bar{\nu}\gamma_\mu\frac{1-\gamma_5}{2}e\right] \tag{1.2.17}$$

so that

$$\frac{G}{\sqrt{2}} = \frac{g^2}{8m_W^2} \tag{1.2.18}$$

It follows that

$$m_W^2 = \left(\frac{\sqrt{2}g^2}{8G}\right)^{1/2} = \left(\frac{\sqrt{2}e^2}{8G\sin^2\theta_W}\right)^{1/2} \tag{1.2.19}$$

Inverting the relations

$$W_\mu^{(3)} = \frac{gZ_\mu + g'A_\mu}{\sqrt{g^2 + g'^2}} \tag{1.2.20}$$

$$B_\mu = \frac{-g'Z_\mu + gA_\mu}{\sqrt{g^2 + g'^2}} \tag{1.2.21}$$

we find

$$Z_\mu = W_\mu^{(3)} \cos\theta_W - B_\mu \sin\theta_W \tag{1.2.22}$$

$$A_\mu = W_\mu^{(3)} \sin\theta_W - B_\mu \cos\theta_W \tag{1.2.23}$$

so that, using the empirical fact that the photon is massless and orthogonal to the Z, we get

$$m_Z = \left(\frac{\sqrt{2}e^2}{8G}\right) \frac{1}{\sin\theta_W \cos\theta_W} = \frac{m_W}{\cos\theta_W} \tag{1.2.24}$$

As input parameters for SM (which should be determined by experiment) conventionally α, G_F, m_Z, m_W and $\sin^2\theta_W$ are chosen. In the current structure, the SM has only three free parameters and the ones most precisely-measured are chosen as input. The mass of W boson is determined thus by the fine structure constant α_{EM} ($g^2 \sin^2\theta_W/4\pi$), the Fermi coupling constant G_F, and Z boson mass m_Z, which are the SM three parameters (not counting the Higgs boson mass, m_H, and the fermion masses and mixing.) The standard set of measurable input parameters is the following

$$\alpha_{EM} = 1/(137.0359895 \pm 0.0000061) \tag{1.2.25}$$

$$G_F = 1.16639(\pm 0.00002) \times 10^{-5} GeV^{-2} \tag{1.2.26}$$

$$m_Z = 91.1884 \pm 0.0022 GeV/c^2 \tag{1.2.27}$$

The fine structure constant is measured from the quantum Hall effect [25]; the Fermi coupling constant is measured from the muon lifetime ($\Gamma(\mu^- \rightarrow e^- \bar{\nu}_e \nu_\mu) = G^2 m_\mu^5 / 192\pi^3$) [25], and m_Z is measured directly by the combined experiments at the CERN e^+e^- collider LEP [26], Tevatron [27] and now at the LHC. With these inputs, $\sin^2\theta_W$ and the W boson mass can be calculated for a given m_t and m_H. Vice versa m_H can be constrained by $\sin^2\theta_W$ and m_W with higher order corrections.

1.2.2 Origin of the Forward-Backward Asymmetry

The forward-backward asymmetry, A_{fb}, is one of the first precision measurements that can be done at the Large Hadron Collider (LHC) [28]. It will improve the knowledge of Standard Model parameters giving a direct insight on the vector (g_V^f) and axial-vector (g_A^f) couplings to the Z/γ^*, and thus to the effective weak mixing angle (Sec. 1.3) and at the same time test the existence of possible New Physics scenarios.

At the LHC the Drell-Yan process is $q\bar{q} \rightarrow Z/\gamma^* \rightarrow \mu^+\mu^-$. The differential

cross section for fermion pair production can be written as:

$$\frac{d\sigma(q\bar{q} \to \mu^+\mu^-)}{d\cos\theta} = C\frac{\pi\alpha^2}{2s}[Q_\mu^2 Q_q^2(1+\cos^2\theta) + Q_\mu Q_q Re(\chi(x))(2g_V^q g_A^\mu(1+\cos^2\theta) + 4g_A^q g_A^\mu \cos\theta) + |\chi(s)|^2((g_V^{q\,2}+g_A^{q\,2})(g_V^{\mu\,2}+g_A^{\mu\,2})(1+\cos^2\theta) + 8g_V^q g_A^q g_V^\mu g_A^\mu \cos\theta)] \quad (1.2.28)$$

where C is the color factor, θ is the emission angle of the lepton(anti-lepton) relative to the quark(anti-quark) in the rest frame of the lepton pair, and

$$\chi(s) = \frac{1}{\cos^2\theta_W \sin^2\theta_W}\frac{s}{s - M_Z^2 + i\Gamma_Z M_Z} \quad (1.2.29)$$

The first and the third terms in Eq. 1.2.28 correspond to the pure γ^* and Z exchange respectively while the second term corresponds to the Z/γ^* interference. The angular dependence of the various terms is either $\cos\theta$ or $(1+\cos^2\theta)$. The $\cos\theta$ terms integrate to zero in the total cross section but induce the forward-backward asymmetry. A simplified version of Eq. 1.2.28 is

$$\frac{d\sigma}{d\cos\theta} = A(1+\cos^2\theta) + B\cos\theta \quad (1.2.30)$$

where A and B are functions dependent of the weak isospin and charge of the incoming fermions and Q^2 of the interaction as can be seen in Eq. 6.8.4 and Eq. 6.8.5

$$A = Q_l^2 Q_q^2 + 2Q_l Q_q g_V^q g_V^l Re(\chi(s)) + (g_V^{l\,2}+g_A^{l\,2})(g_V^{q\,2}+g_A^{q\,2})|\chi(s)|^2 \quad (1.2.31)$$

$$B = \frac{3}{2} g_A^q g_A^l (Q_l Q_q Re(\chi(s)) + 2 g_V^q g_V^l |\chi(s)|^2) \tag{1.2.32}$$

To obtain the forward-backward charge asymmetry an integration over $\cos\theta$ is needed. Events with $\cos\theta > 0$ are called forward events, while events with $\cos\theta < 0$ are called backward events. The integrated cross section for forward events is thus $\sigma_F = \int_0^1 \frac{d\sigma}{d\cos\theta} d\cos\theta$ and the integrated cross section for backward events is $\sigma_B = \int_{-1}^0 \frac{d\sigma}{d\cos\theta} d\cos\theta$. The A_{fb} is defined as

$$\begin{aligned} A_{fb} &= \frac{\sigma_F - \sigma_B}{\sigma_F + \sigma_B} \\ &= \frac{\int_0^1 \frac{d\sigma}{d\cos\theta} d\cos\theta - \int_{-1}^0 \frac{d\sigma}{d\cos\theta} d\cos\theta}{\int_0^1 \frac{d\sigma}{d\cos\theta} d\cos\theta + \int_{-1}^0 \frac{d\sigma}{d\cos\theta} d\cos\theta} \\ &= \frac{N_F - N_B}{N_F + N_B} \\ &= \frac{3B}{8A} \end{aligned} \tag{1.2.33}$$

where N_F and N_B are numbers of forward and backward events.

Fig. 1.1 shows the A_{fb} as a function of the di-muon invariant mass for PYTHIA [29] Monte Carlo simulation. The tree level predictions for A_{fb} for $u\bar{u} \to \mu^+\mu^-$ and $d\bar{d} \to \mu^+\mu^-$ are shown separately.

1.2.3 The Collins-Soper Reference Frame

When the incoming quarks participating in the Drell-Yan process have no transverse momentum relative to their parent baryons, θ is determined unambiguously from the four-momenta of the leptons by calculating the angle that the lepton makes with the proton beam in the center-of-mass frame of

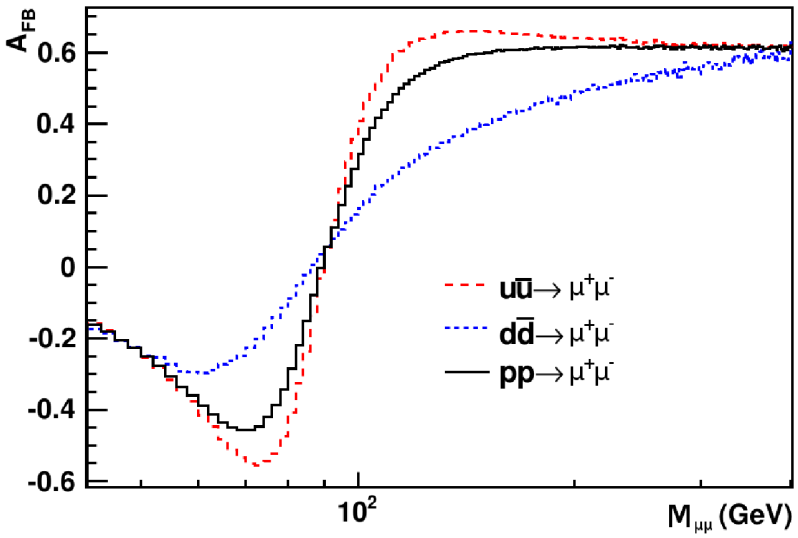

Figure 1.1: The Standard Model tree level A_{fb} prediction as a function of the di-muon invariant mass for $u\bar{u} \rightarrow \mu^+\mu^-$, $d\bar{d} \rightarrow \mu^+\mu^-$ and $pp \rightarrow \mu^+\mu^-$.

the muon pair. When either of the incoming quarks has significant transverse momentum, however, there exists an ambiguity in the four-momenta of the incoming quarks in the frame of the dilepton pair, since one can not determine the four-momenta of the quark and anti-quark individually. The Collins-Soper (CS) formalism [30] is adopted to minimize the effects of the transverse momentum of the incoming quarks. In this formalism, the polar axis is defined as the one bisecting the angle between the momentum of one of the partons and the opposite of the momentum of the second one when they are boosted into the center-of-mass frame of the dilepton pair. The complete mechanism leading to the use of this particular reference frame is shown in Fig. 1.2.

The cosine of the decay angle $\cos\theta^*$ can be written as a function of the lepton momenta in the laboratory reference frame. Let $Q(Q_T)$ be the four momentum (transverse momentum) of the dilepton pair, P_1 and P_2 be the

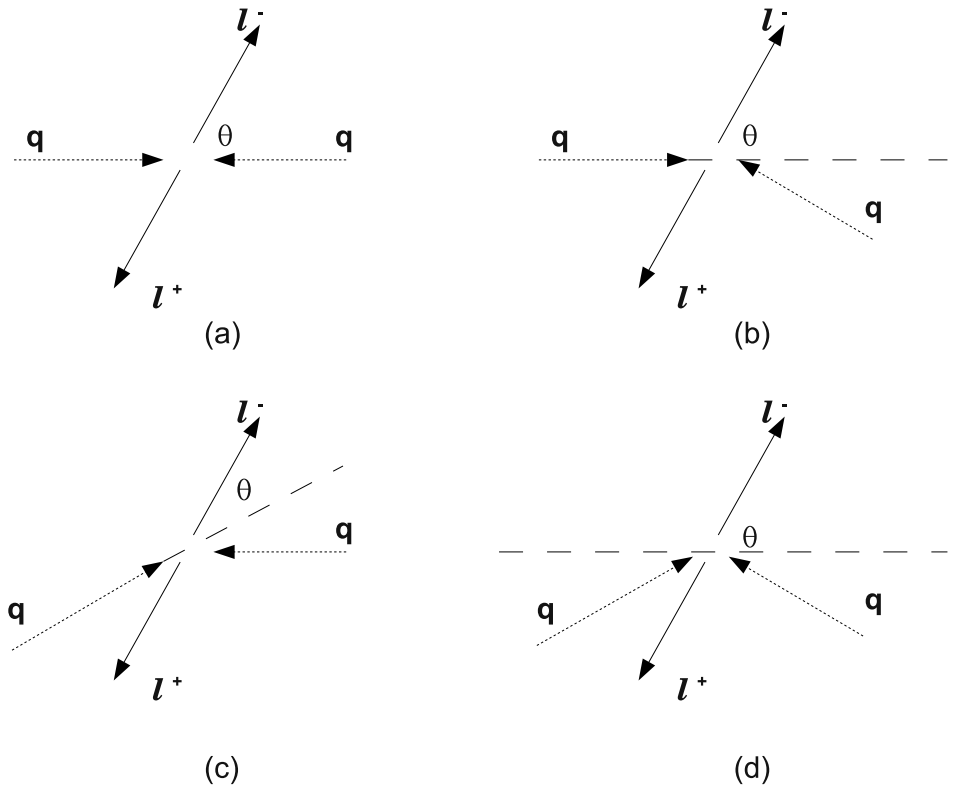

Figure 1.2: The Collins-Soper reference frame. When the incoming partons do not have any transverse momentum, as shown in (a), the angle of the resulting lepton can be uniquely defined. On the other hand, an ambiguity exists in the definition in the case where one of the partons has non-zero transverse momentum, as in (b) and (c). The Collins-Soper reference frame (d) resolves the ambiguity by choosing a symmetric axis between the two incoming partons.

four-momentum of the lepton and anti-lepton respectively, all measured in the lab frame. Then $\cos\theta^*$ is given by

$$\cos\theta^* = \frac{2}{Q\sqrt{Q^2+Q_T^2}}(P_1^+P_2^- - P_1^-P_2^+) \tag{1.2.34}$$

where $P_i^\pm = \frac{1}{\sqrt{2}}(P_i^0 \pm P_i^3)$, with P^0 and P^3 representing the energy and the longitudinal component of the momentum. Fig. 1.3 shows the *true* $\cos\theta^*$

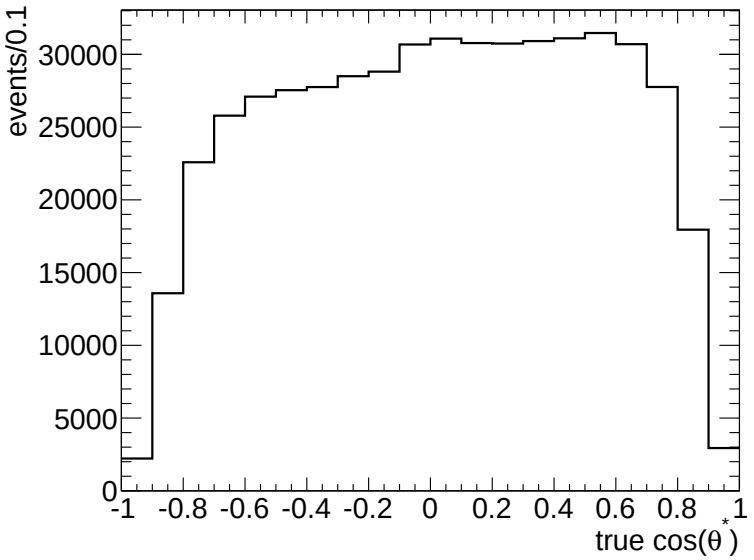

Figure 1.3: *True* $\cos\theta^*$ distribution for PYTHIA $Z/\gamma^* \rightarrow \mu\mu$ Monte Carlo events after the Z/γ^* candidate event selection.

distribution obtained with a PYTHIA $Z/\gamma^* \rightarrow \mu\mu$ Monte Carlo sample with an invariant mass greater than 60 GeV after the Z/γ^* candidate event selection described in Chap. 4 .

1.2.4 Dilution

In order to measure A_{fb}, the quark and anti-quark directions need to be known. However, at the LHC these directions can not be known directly. Since the anti-quark is a sea-quark, on average, the anti quark should have less momentum than the valence quark. Therefore we can assume that the Z boson is boosted in the quark direction and then correct for this effect by properly accounting for misidentification probabilities. The probability that the above assumption is not correct (mistag probability) does also depend on the mass of the di-

muon system. The measured A_{fb} values can be related to the true A_{fb} values through dilution factors. The dilution can be corrected on an event-by-event basis, extracting the mistag probability from Monte Carlo as a function of the di-muon rapidity and mass [31].

1.3 The Weak Mixing Angle

The weak mixing angle is an important parameter of the Standard Model. The value of $\sin^2\theta_W$ depends on the renormalization prescription: according to the different dependence on the m_t and m_H there are various schemes leading to different values, which are shown in Tab.1.4.

Scheme	Notation and Value
On-Shell [32]	$s^2_W = \sin^2\theta_W \sim 0.2231$
NOV [33]	$s^2_{m_z} = \sin^2\theta_W \sim 0.2311$
$\overline{MS}$ [34]	$s^2_Z = \sin^2\theta_W \sim 0.2312$
$\overline{MS}$ ND [35]	$s^2_{ND} = \sin^2\theta_W \sim 0.2314$
Effective	$s^2_f = \sin^2\theta_W \sim 0.2315$

Table 1.4: The weak mixing angle value with different renormalization prescriptions.

In the following the effective weak mixing angle scheme will be considered.

$\sin^2\theta_{eff}$ Scheme

In the SM at tree level, the relationship between the weak and electromagnetic couplings is given by

$$G_F = \frac{\pi\alpha}{\sqrt{2}m_W^2 \sin^2\theta_W^{tree}} \tag{1.3.1}$$

where G_F is the Fermi constant, α is the electromagnetic fine-structure constant, m_W is the W boson mass, and $\sin^2\theta_W^{tree}$ is the electroweak mixing angle at tree level. The relationship between the neutral and charged weak couplings is fixed by the ratio of the W and Z boson masses:

$$\rho_0 = \frac{m_W^2}{m_Z^2 \cos^2\theta_W^{tree}} \tag{1.3.2}$$

The fermions are arranged in the weak-isospin doublets for left-handed particles and weak-isospin singlets for right-handed particles. The interaction of the Z boson with fermions depends on charge Q, and the third component of weak-isospin I_3^f, the left- and right-handed couplings can be written as:

$$g_L^{tree} = \sqrt{\rho_0}(I_3^f - Q_f \sin^2\theta_W^{tree}) \tag{1.3.3}$$

$$g_R^{tree} = -\sqrt{\rho_0} Q_f \sin^2\theta_W^{tree} \tag{1.3.4}$$

For the vector and axial-vector couplings in the tree level:

$$g_V^{tree} = g_L^{tree} + g_R^{tree} = \sqrt{\rho_0}(I_3^f - 2Q_f \sin^2\theta_W^{tree}) \tag{1.3.5}$$

$$g_A^{tree} = g_L^{tree} - g_R^{tree} = \sqrt{\rho_0} I_3^f \tag{1.3.6}$$

There are some radiative corrections to be considered, such as the propagators and vertices corrections. After renormalizing these corrections, ρ_0 is main-

tained and taken to define the on-shell electroweak mixing angle θ_W:

$$\rho_0 = \frac{m_W^2}{m_Z^2 \cos^2 \theta_W} \tag{1.3.7}$$

In the following, $\rho = 1$ is assumed.

The bulk of the electroweak corrections [36] to the couplings at the Z-pole is absorbed into complex form factors, R_f for the overall scale and K_f for the on-shell electroweak mixing angle, resulting in complex effective couplings:

$$\mathcal{G}_V^f = \sqrt{R_f}(I_3^f - 2Q_f K_f \sin^2 \theta_W) \tag{1.3.8}$$

$$\mathcal{G}_A^f = \sqrt{R_f} I_3^f \tag{1.3.9}$$

In terms of the real parts of the complex form factors,

$$\rho_f = \mathcal{R}(R_f) = 1 + \Delta\rho_{se} + \Delta\rho_f \tag{1.3.10}$$

$$k_f = \mathcal{R}(k_f) = 1 + \Delta k_{se} + \Delta k_f \tag{1.3.11}$$

The effective electroweak mixing angle and the real effective couplings are defined as:

$$\sin^2 \theta_{eff}^f = k_f \sin^2 \theta_W \tag{1.3.12}$$

$$g_V^f = \sqrt{\rho_f}(I_3^f - 2Q_f \sin^2 \theta_{eff}^f) \tag{1.3.13}$$

$$g_A^f = \sqrt{\rho_f}(I_3^f) \tag{1.3.14}$$

so that

$$\frac{g_V^f}{g_A^f} = \mathcal{R}\left(\frac{\mathcal{G}_V^f}{\mathcal{G}_A^f}\right) = 1 - 4|Q_f|\sin^2\theta_{eff}^f \tag{1.3.15}$$

The quantities $\Delta\rho_{se}$ and Δk_{se} are universal corrections arising from the propagator self-energies, while $\Delta\rho_f$ and Δk_{se} are flavor-specific vertex corrections.

1.4 Importance of the A_{fb} Measurement

1.4.1 Test of the Standard Model

The forward-backward asymmetry is related to the vector and axial-vector couplings of the quarks and the leptons to the Z/γ^* and is therefore sensitive to the effective weak mixing angle $\sin^2\theta_{eff}$.

The weak mixing angle is an important constant in the electroweak theory that describes the connection between the weak and electromagnetic interactions. This angle, measured from the A_{fb} distribution, can also be used to constraint the Higgs-boson mass as shown in Fig. 1.4. The experimental results from SLAC, LEP [37], Tevatron [38, 39], NuTeV [40] and other experiments including also now the LHC one, have confirmed the SM to unprecedented accuracy, and most electroweak observables gave consistent results with SM.

Currently the results from two measurements are quite far from the SM predictions: the measurement from LEP of $A_{fb}^{0,b}$, the Standard Model prediction of the Z^0 pole forward-backward asymmetry of b quarks produced in $e^+e^- \to b\bar{b}$

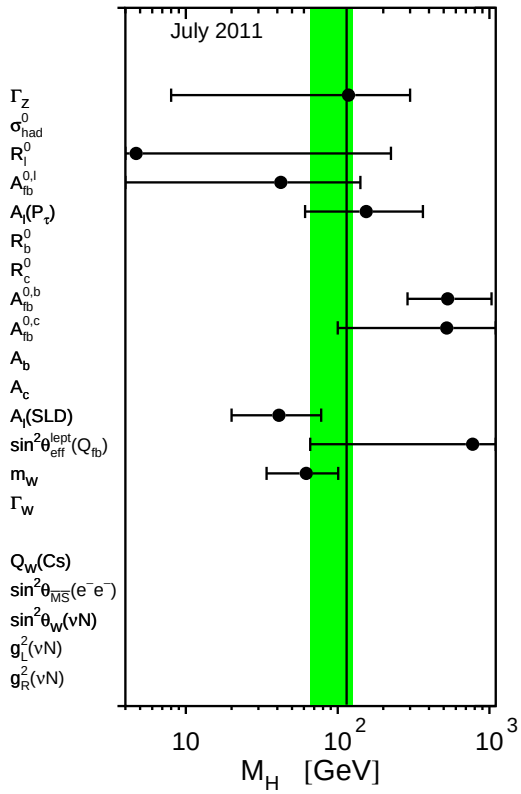

Figure 1.4: Constraint on the Higgs mass determined for each observable with a global fit on the SM parameters. The vertical green band denotes the overall constraint on the Higgs mass derived from the fit to all data. The vertical black line denotes the limit on the Higgs mass obtained from the direct search at LEP-2.

events, is 2.4 σ from the fit [37], which is shown in Fig. 1.5. And the NuTeV measurement of $\sin^2\theta_{eff}$ is 2.9 σ from the fit [40].

1.4.2 Beyond the Standard Model

The A_{fb} measurement can be used not only to confirm the SM Z/γ^* interference which dominates around the Z pole region, but also to investigate possible new phenomena which may alter A_{fb} such as new neutral Z' gauge bosons or

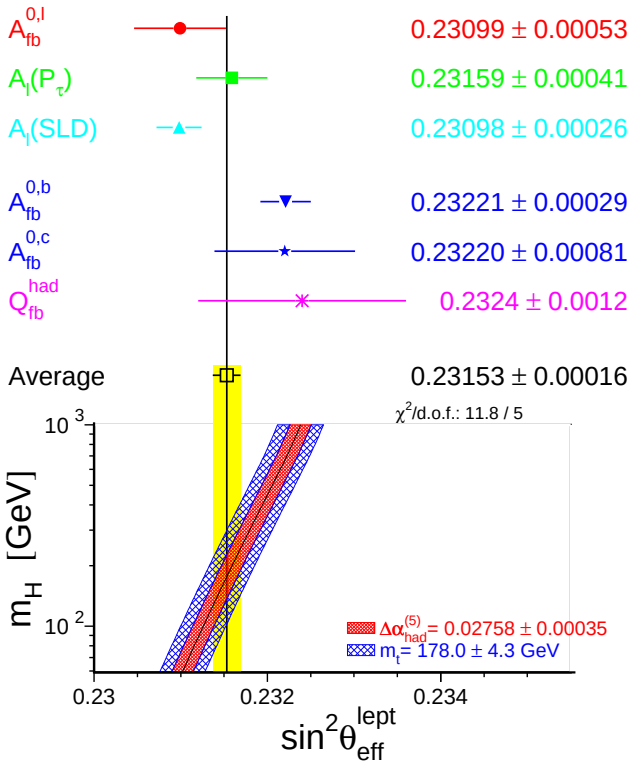

Figure 1.5: Comparison of the effective electroweak mixing angle $\sin^2\theta_{eff}$ from LEP and SLD. Also shown is the SM prediction for $\sin^2\theta_{eff}$ as a function of m_H. The additional uncertainty of the SM prediction is shown as bands.

large extra dimensions.

Many theorists are looking for symmetries beyond the SM that will solve the problems related to the theory, attempting to incorporate gravity. Many of these extensions to the SM predict the existence of a new neutral gauge heavy boson, Z' [41]. The existence of a Z' could lead to deviations of the A_{fb} and the cross section from that predicted in the SM. If a Z' is in the family of grand unified theories (GUT), which attempt to unify the three interactions at the unification energy (typically 10^{15} GeV), SU(2), U(1), and SU(3) symmetries

could be incorporated into a more global gauge symmetry, SU(5) [42]. SU(5) has no additional neutral gauge bosons, and is also excluded by precision data [42]. SU(5) may be part of a larger SO(10) gauge group which does not contradict current experimental data, and predicts at least one extra neutral gauge boson [43]. Some string-theory models [44] suggest further embedding into an E6 gauge group [45]. One of the possible breaking scenarios is

$$E_6 \rightarrow SO(10) \times U(1)_\Psi \rightarrow SU(5) \times U(1)_\chi \times U(1)_\Psi \tag{1.4.1}$$

The most general Z' within E_6 can be written as

$$Z' = Z'_\Psi \cos\theta + Z'_\chi \sin\theta \tag{1.4.2}$$

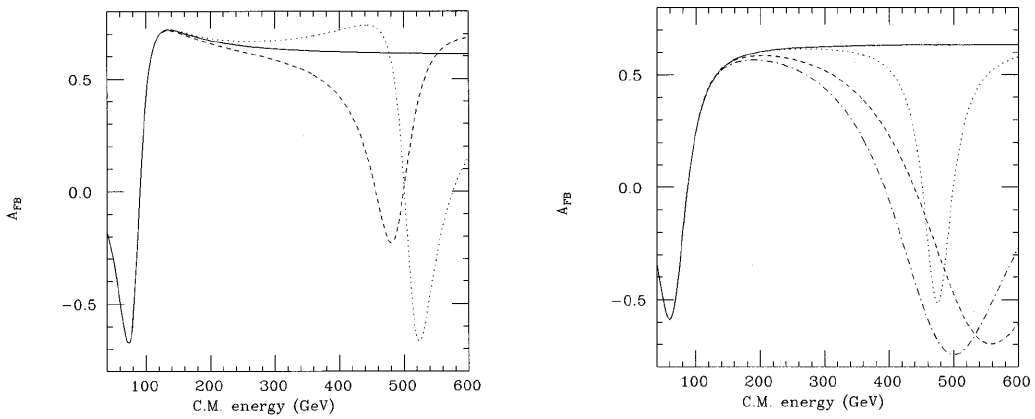

Figure 1.6: Parton-level forward-backward asymmetries for $u\bar{u}/d\bar{d} \rightarrow \mu\mu$ when adding Z' with different mixing angles from an E_6 gauge group [46]. Solid line: Standard Model. Dashed line: 500 GeV Z'_χ added. Dotted line: 500 GeV Z'_Ψ added. Dot-dashed line: 500 GeV Z'_I added.

where θ is the mixing angle of Z'. Fig. 1.6 shows the A_{fb} when adding a 500 GeV Z' with different mixing angles. For $\theta = \arctan(5/3)$, E_6 may also

break down to $SU(6) \times SU(2)_I$, where the subscript stands for "inert", since all gauge bosons of $SU(2)_I$ are neutral. The $I_{3I} = 0$ member of the $SU(2)_I$ triplet is called Z_I.

If there is a new high mass gauge boson such as Z' that can interfere with Z and γ^*, it will change the predicted A_{fb} values at high mass region, so this explain the interest to extend the measurement to events with $m_{Z/\gamma^*} < 1000$ GeV.

Chapter 2

The Large Hadron Collider

The head-on collisions of particles (mainly pp, $p\bar{p}$, e^+e^-) provide the largest center of mass energy, which is available for the creation of new particles. The Large Electron Positron (LEP) collider, which was in operation at CERN from the year 1989 to 2000, accelerated electrons and positrons to an energy of ~ 105 GeV, which results in a maximum available collision energy of ~ 210 GeV [47]. The highest energy of the electron and positron colliders is limited by the synchrotron radiation which is emitted by the accelerated charged particles.

The acceleration of protons overcomes this problem, since the radiated power is proportional to $1/m^4$, where m is the mass of the accelerated particle. The prize to pay are the QCD interactions during a collision of protons, which lead to large background processes and no clean final states. Moreover, the initial energy and the momentum of the colliding partons is unknown. Thus hadron colliders reach higher energies and, therefore, may create new particles, but precision measurements are more demanding.

It is technically much easier to produce and accelerate a large number

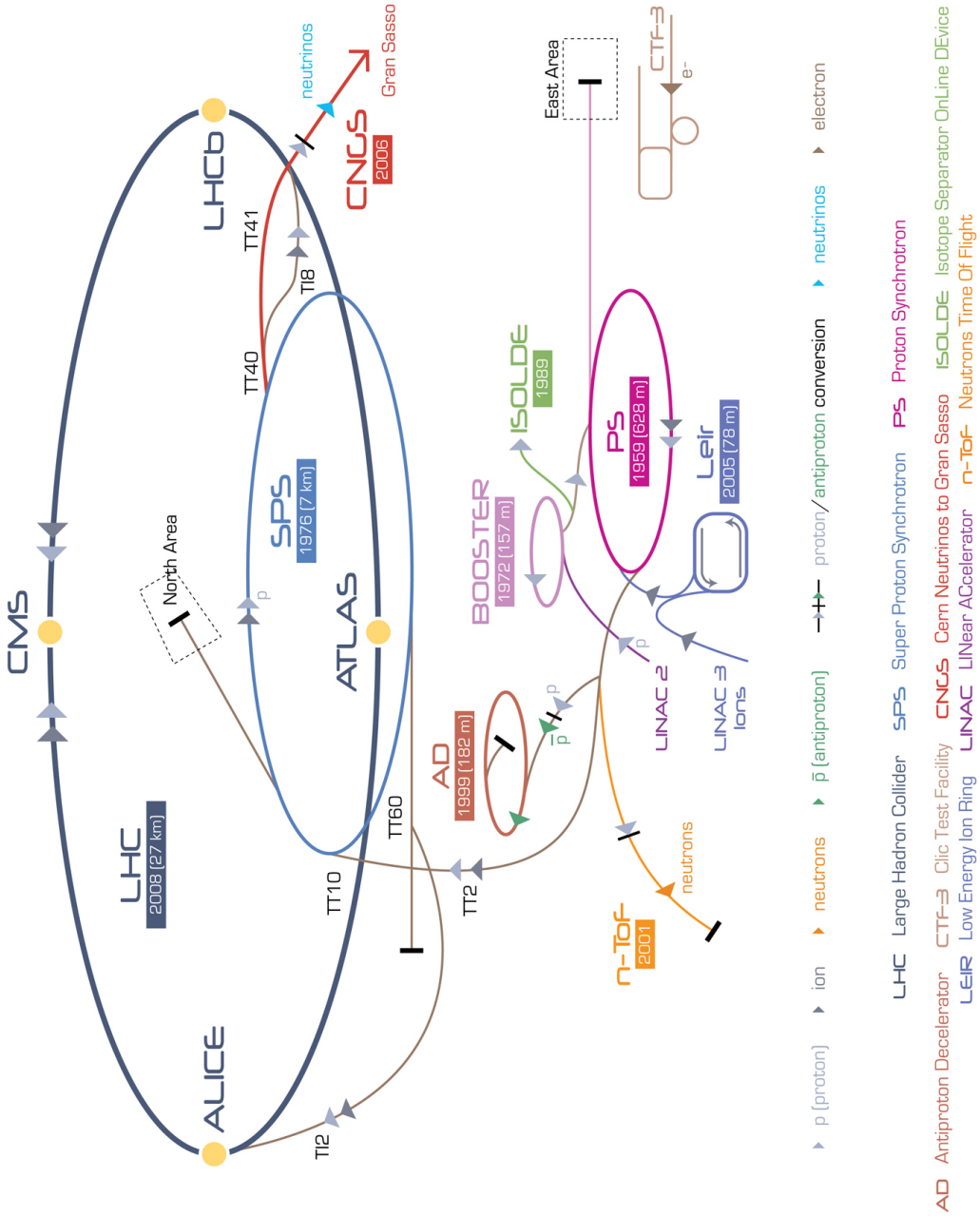

Figure 2.1: CERN accelerator complex.

of protons, than an equal amount of anti-protons. Hence, colliding protons at high energies offers high luminosities ($\mathcal{L}$), i.e. the expected rate of proton-proton collisions per second and per square centimeter, at high energies, which were the basic arguments for the design of the successor of the LEP collider: the Large Hadron Collider (LHC) [28].

The LHC, is a proton-proton collider with a designed center of mass energy of 14 TeV. It is built in the tunnel of the former LEP collider, which has a circumference of 26.7 km (Fig.2.1). Super conducting magnets are the basic technology of the LHC and are used for bending and focusing the counter rotating proton beams. A designed instantaneous luminosity of $10^{34}\text{cm}^{-2}\text{s}^{-1}$ is reached, by accelerating of 2835 proton bunches per direction, consisting of 10^{11} particles, with a bunch length of 7.5 cm and a time between the collisions of 25 ns. The luminosity lifetime is expected to be in the order of ten hours.

The beam-pipe of the LHC (Fig.2.2) contains two separate beam-lines for the opposite direction of the two proton beams, which also makes an opposite magnetic field for both beam-lines necessary. The solution to this technical problem are so-called twin-bore magnets, which consist of a set of coils. The advantage of this approach is that the whole structure can use the same cooling infrastructure within the same beam-pipe

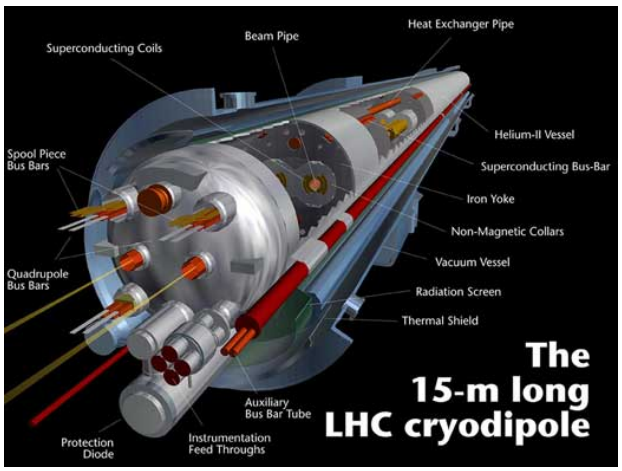

Figure 2.2: One of the 1232 LHC cryodipole.

(Fig.2.2). The cooling of 1232 magnets with a field strength of 8.33 Tesla and 392 quadrupoles is achieved by super-fluid Helium at a temperature of $\sim$ 2 K.

Before injecting the proton beams into the LHC, they traverse several other acceleration steps. The protons are extracted from hydrogen gas and accelerated in bunches of $\sim 10^{11}$ protons by the Linac accelerator to 50 MeV. These bunches are further accelerated by the PS booster to 1.4 GeV, followed by the Proton Synchrotron (PS) and the Super Proton Synchrotron (SPS) which accelerate the proton bunches to 26 GeV and finally up to an injection energy of 450 GeV, respectively. Some periods of the LHC running are dedicated to the acceleration of lead nuclei up to an energy of 1150 TeV with a luminosity of $\mathcal{L} = 10^{27}$ cm^{-2} s^{-1}.

Four particle detectors are currently installed at the LHC: ATLAS[1] (cfr. Chap. 3) and CMS[2] are general purpose detectors, which cover a broad field of experimental studies. The ALICE[3] experiment is designed to study the quark gluon plasma, i.e. a state of matter in which the quarks and gluons can be considered as free particles. The LHCb[4] experiment is dedicated to B-meson physics and will study CP-violation to high precision.

[1] A Toroidal LHC ApparatuS
[2] Compact Muon Solenoid
[3] A Large Ion Collider Experiment
[4] Large Hadron Collider beauty

Chapter 3

The ATLAS Experiment

The ATLAS (A Toroidal LHC ApparatuS) [3,48] detector at the LHC was designed and built for general physics studies of high energy collisions, including measurements of Standard Model (SM) parameters, confirmation or exclusion of the Higgs boson and searches for physics signatures corresponding to phenomena Beyond the SM (BSM). ATLAS is intended to provide a good quality measurement of high-p_T objects including electrons e, photons γ, muons μ, jets, b-quark jets and missing transverse energy E_T^{miss}.

3.1 Overview

An overview of the ATLAS detector and its sub-systems is shown in Fig. 3.1. The detector is comprised of an inner tracking system (inner detector, or ID), surrounded by a superconducting solenoid providing a 2 T magnetic field, electromagnetic and hadronic calorimeters and a muon spectrometer (MS). ATLAS also includes forward detectors whose main goal is to measure the

luminosity: LUCID (LUminosity measurement using Cherenkov Integrating Detector) and ALPHA (Absolute Luminosity For ATLAS). The ID consists of pixel and silicon micro-strip (SCT) detectors, surrounded by a transition radiation tracker (TRT). It provides precision transverse momentum measurements of charged particles up to $|\eta| < 2.5$. The calorimeters are hermetic up to $|\eta| < 4.9$ and are designed to capture the showers of high energy electrons, photons and hadrons. The electromagnetic calorimeter is a lead liquid-argon (LAr) detector in the barrel and the end-cap, while in the forward region copper LAr technology is used. Hadron calorimetry is based on two different detector technologies, with scintillator tiles or LAr as the active media, and with either steel, copper, or tungsten as the absorber material. The muon spectrometer, with coverage up to $|\eta| < 2.7$, is based on three large superconducting toroids, and a system of three stations of chambers for fast trigger and precision tracking measurements. Finally, the ATLAS detector includes a trigger and data acquisition system that collects the most interesting events. The data recorded is distributed world-wide using the LHC Computing Grid for processing and analysis. The overall design choices for ATLAS, including its size, are derived from beam constraints, such as collisions energies and luminosity rates, and the expected physics reach. The harsh LHC collision environment and the operational lifetime of about ten years imposes strict requirements on the detector technologies that should be fast, radiation-hard and experience low rates of aging. Pileup interactions present additional challenges, requiring high granularity in order to reduce the impact of ambiguities that may arise in the overlap between interesting and minimum bias events. The amount of material in the calorimeters is driven by the need to contain 1 TeV electrons (about 30

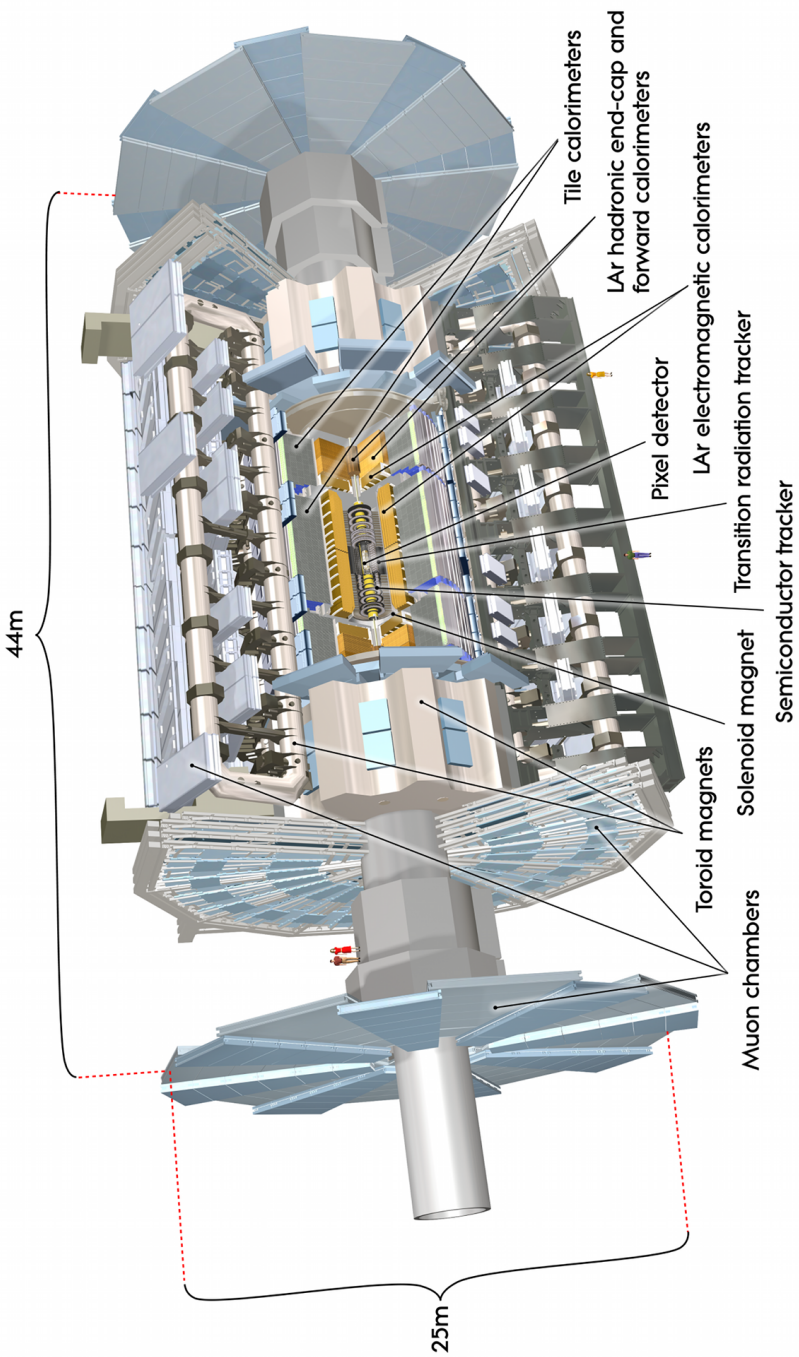

Figure 3.1: Drawing of the ATLAS detector. The dimensions of the detector are 25 m in height and 44 m in length. The overall weight of the detector is approximately 7000 tonnes.

radiation lengths, X_0) and 1 TeV pions (about 11 absorption lengths, λ) and the dimensions of the muon system are imposed by the desire to measure 1 TeV muons, requiring several Tm of bending power. The choice of the magnet system, made up of two components: the solenoid surrounding the ID and the toroid for the MS, gives ATLAS its overall characteristic form.

The main performance goals for each sub-detector, as constrained by Higgs and hypothesized BSM signatures are listed in Tab. 3.1. The inner tracker should reconstruct the trajectory of charged particles with high efficiency and good momentum resolution in order to observe collision vertices, as well as secondary vertices associated with heavy quark decays. It is also crucial for electron, muon and tau identification. The calorimeters are designed to provide very good identification and a high resolution measurement of electrons and photons, important for example to observe a Higgs boson at low mass decaying to two photons. The calorimeters should additionally measure jets and missing transverse energy accurately, which is a requirement for any analysis, such as searches for supersymmetric particles decaying into stable non-interacting particles. The muon detectors are intended to provide reliable identification and good resolution for momenta ranging from a few GeV up to 1 TeV, in order to allow for the observation of new particles, such as heavy gauge bosons W' and Z', with masses in the TeV range and decaying to muons. The detector is designed to be capable of identifying very rare event signatures, in some cases corresponding to 14 orders of magnitude below the total pp cross section. As a result, stringent requirements on the trigger are imposed to provide high efficiency for physics processes of interest while rejecting backgrounds.

Detector Component	Design Resolution	$\|\eta\|$ Coverage	
		Measurement	Trigger
Tracking	$\sigma_{p_T}/p_T = 0.05\% \oplus 1\%$	2.5	
EM Calorimetry	$\sigma_E/E = 10\%/\sqrt{E} \oplus 0.7\%$	3.2	2.5
Hadronic Calorimetry			
Barrel and End-cap	$\sigma_E/E = 50\%/\sqrt{E} \oplus 3\%$	3.2	3.2
Forward	$\sigma_E/E = 100\%/\sqrt{E} \oplus 10\%$	3.1 - 4.9	3.1 - 4.9
Muon Spectrometer	$\sigma_{p_T}/p_T = 10\%$ at $p_T = 1$ TeV	2.7	2.4

Table 3.1: ATLAS performance goals. The units for E and p_T are GeV.

Coordinate System

The origin of the ATLAS coordinate system is defined as the nominal interaction point (IP), located in the geometrical center of the detector. The beam direction defines the z-axis, the x-axis points to the center of the LHC ring and the y-axis points towards the surface, as a right-handed coordinate system. The detector is symmetric in positive and negative z, called sides A and C respectively. The azimuthal angle ϕ is measured in the x-y plane around the beam axis, and the polar angle θ corresponds to the angle from the beam axis. The pseudorapidity is defined from θ as $\eta = -ln(\tan\theta/2)$. In the case of objects with large mass, the rapidity is used $y = 1/2ln[(E + p_z)/(E - p_z)]$. The distance ΔR in the η - ϕ angle space is defined as $\Delta R = \sqrt{\Delta\eta^2 + \Delta\phi^2}$. Finally, it may be noted that the transverse momentum p_T , the transverse energy E_T and the missing transverse energy E_T^{miss} are defined in the transverse x-y plane.

3.2 Inner Detector

The inner detector (shown in Fig. 3.2) is comprised of high-resolution semiconductor pixel and strip detectors (SCT) in the inner part, covering the region

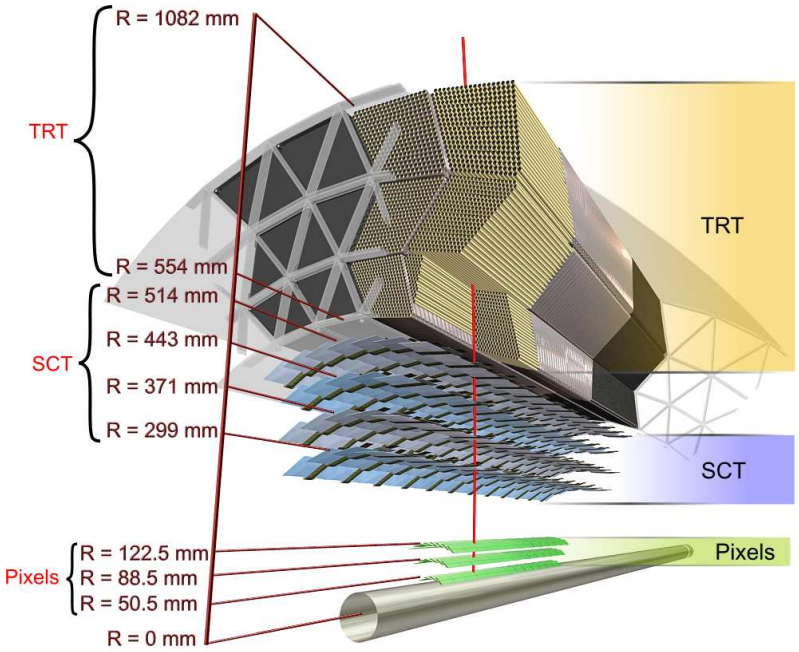

Figure 3.2: Drawing showing the sensors and structural elements of the inner detector

$|\eta| < 2.5$, and straw-tube tracking detectors (TRT) in the outer part, covering the region $|\eta| < 2.0$. The 2 T magnetic field is provided by a superconducting solenoid magnet extending over a length of 5.3 m with a diameter of 2.5 m. The ID performs momentum and vertex measurements for charged particles. The active tracking detector elements record the position of charged particles traversing it, and this information is used to reconstruct the particle's trajectory as a track. The charged particles bend in the presence of the magnetic field, and the radius of curvature determined by the tracking is used to derive the transverse momentum of the particle using the relation

$$p_T \text{ [GeV]} = 0.3 \times B \text{ [T]} \times R \text{ [m]} \tag{3.2.1}$$

where B is the magnetic field and R the bending radius. The hit efficiency for the trackers is very high, about 99% in the silicon detectors, and typically about 3 pixel, 4 SCT and about 36 TRT measurements are provided per track. The limitations arise from the constraints imposed by the detector coverage and disabled detector modules.

Pixel Detector

The pixel modules are arranged around the beam axis in three concentric cylinders for the barrel region (at radii of 50.5, 88.5, and 122.5 mm) and in three disks (at $|z|$ positions of 495, 580 and 650 mm) for each end-cap, providing coverage in the range $|\eta| < 2.5$. The pixels are the highest granularity subsystem and the innermost pixel layer is mounted on the beam pipe in order to provide the best possible vertex resolution. Given the large radiation doses, it may be noted that the innermost layer is expected to survive five years at most, after which it is expected to be replaced after the 2013-2014 shutdown. The pixels are doped silicon detectors to which a bias voltage is applied. When a charged particle traverses the semiconductor, it creates sufficient electron-hole pairs to travel to the surface and produce a measurable signal.

The pixel detector is segmented in $R-\phi$ and z with size in $R-\phi \times z$ of 50×400 μm^2. Given the fine segmentation of the pixel modules, a traversing particle results in a signal in multiple contiguous pixels, forming "clusters". Each track originating in the IP typically traverses three layers. The intrinsic spatial resolution is 10 μm ($R-\phi$) and 115 μm (z) in the barrel and 10 μm ($R-\phi$) and 115 μm (R) in the disks. The alignment constraints are 10 μm

in R, 20 μm (barrel) or 100 μm (end-cap) in z and 7 μm in $R-\phi$. The pixel detector has approximately 80.4 million readout channels, corresponding to close to 90% of the total number of ATLAS channels.

Semiconductor Tracker

The silicon strip tracker surrounding the pixel detector is arranged in four concentric cylinders for the barrel (at radii of 299, 371, 443, and 514 mm) and in six end-cap disks on both sides of the IP (at $|z|$ positions of 890, 1091, 1350, 1771, 2115 and 2608 mm), also providing coverage in the range $|\eta| < 2.5$. The basic unit is a silicon strip with a mean pitch of 80 μm, placed parallel to the beam in the barrel and radially in the end-cap, thus providing a precision measurement in $R-\phi$. The barrel cylinders and the first, third and sixth end-cap disks include "stereo-strips", where a second module is attached to the first one at an angle of 40 mrad. These improve the resolution in the non-precision coordinate. A charged particle track typically traverses eight strip sensors corresponding to four space points. The intrinsic resolutions per module are 17 μm ($R-\phi$) and 580 μm (z) for the barrel and 17 μm ($R-\phi$) and 580 μm (R) for the end-cap disks. The alignment constrains the position of the strips to be known to 100 μm in R, 50 μm (barrel) or 200 μm (end-cap) in z, and 12 μm in $R-\phi$. The total number of readout channels in the SCT is approximately 6.3 millions.

Transition Radiation Tracker

The TRT surrounding the SCT is comprised of 4 mm diameter straw tubes that provide about 36 hits per track with coverage in the range $|\eta| < 2.0$. The tubes are placed parallel to the beam in the barrel region ($|\eta| < 1.0$) and radially in wheels in the end-cap region ($0.8 < |\eta| < 2.0$), providing a measurement in $R - \phi$ with an intrinsic precision of 130 μm per tube. The alignment tolerance is 30 μm. The tubes are filled with a gaseous mixture of carbon dioxide and xenon and operate in a similar manner to the drift tubes used in the MS (see Sec. 3.4). Charged particles traversing the TRT also produce transition radiation that is used to distinguish between electrons and pions. The total number of TRT readout channels is approximately 351000.

3.3 Calorimeter System

The ATLAS calorimeter system (shown in Fig. 3.3) is comprised of multiple technologies that provide electromagnetic and hadronic energy measurements. The electromagnetic (EM) calorimeter is a liquid-argon (LAr) sampling calorimeter with high granularity covering the range $|\eta| < 3.2$. The calorimeter has over 22 radiation lengths (X_0) in the barrel and over 24 X_0 in the end-caps, allowing it to contain the showers of electrons and photons up to about 1 TeV and about 2/3 of most hadronic showers. The hadronic calorimeter comprises a scintillator-tile calorimeter with lead absorbers covering the central range $|\eta| < 1.7$ and LAr calorimeters with lead, copper or tungsten absorbers covering the end-cap range $1.5 < |\eta| < 3.2$ (hadronic end-cap calorimeter or HEC) and forward region which extends the coverage up to $|\eta| = 4.9$ (forward

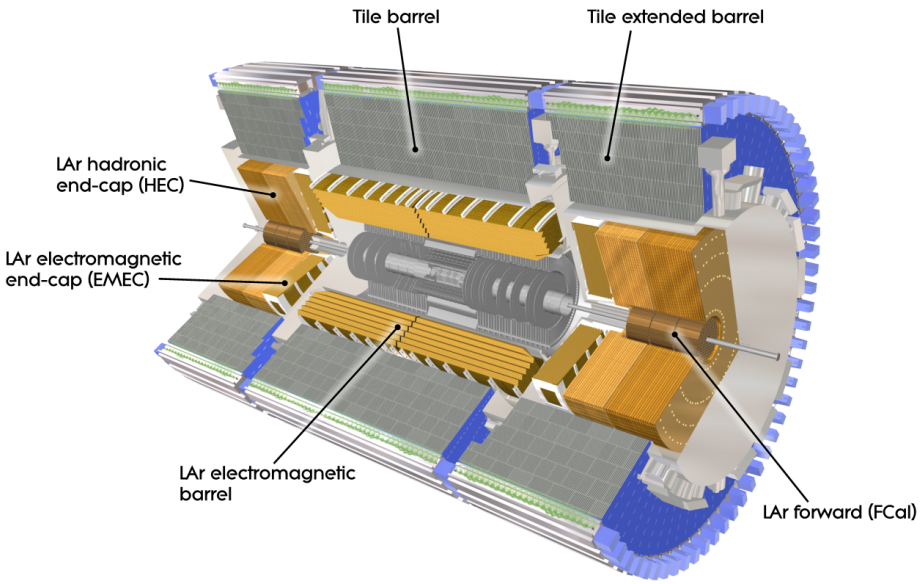

Figure 3.3: Overview of the ATLAS calorimeter system showing the electromagnetic calorimeter and the hadronic calorimeter.

calorimeter or FCal). The depth of the hadronic calorimeters is about 9.7 interaction lengths (λ) of active calorimeter in the barrel and about 10λ in the end-caps, providing good resolution for high-energy jets. The presence of additional passive material (indicated by the last layer in Fig. 3.4), increasing the thickness to over 11 λ, greatly reduces punch-through to the MS, with levels below those from prompt and decay muons. The thickness and large $|\eta|$-coverage of the calorimeters provide a good mismeasurement of the E_T , which is important for many physics signatures including the measurement of W bosons.

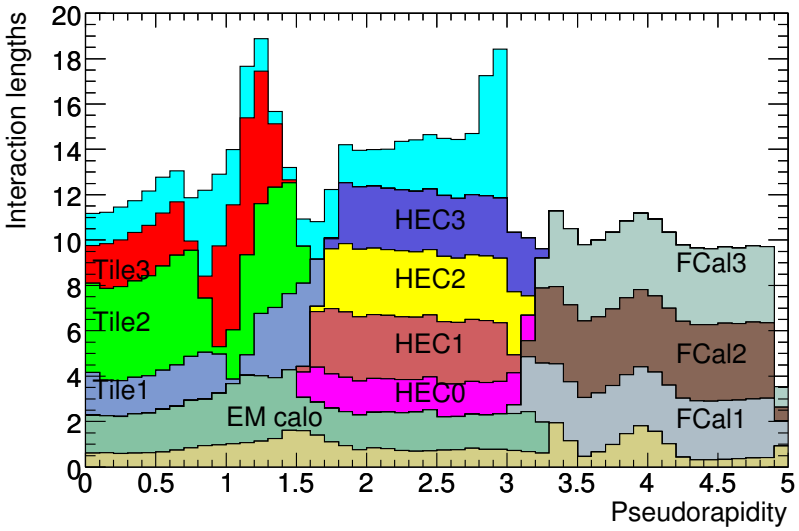

Figure 3.4: Cumulative amount of material, in units of interaction length, as a function of $|\eta|$, in front of the electromagnetic calorimeters, in the electromagnetic calorimeters themselves, in each hadronic layer, and the total amount at the end of the active calorimetry. Also shown for completeness is the total amount of material in front of the first active layer of the muon spectrometer (up to $|\eta| < 3.0$).

Electromagnetic Calorimeter

The EM calorimeter is a LAr detector with lead absorber plates in an accordion geometry that provides uninterrupted $|\phi|$ coverage. As particles traverse the calorimeter they ionize the LAr and the charge deposits are collected in the presence of an electric field by Kapton electrodes mounted on the accordion plates. The calorimeter is divided into three regions: a barrel section covering the range $|\eta| < 1.475$ and an end-cap and forward section on each side covering the ranges $1.375 < |\eta| < 3.2$ and $3.1 < |\eta| < 4.9$ respectively. The choice of LAr as the active detector medium is given by its intrinsic properties of linear behavior, stable response over time and radiation hardness. In

order to maintain the argon in liquid state, it is cooled to about 87 K, so the calorimeters are located in cryostats composed of two concentric aluminum vessels, an inner cold vessel and an outer warm vessel. The barrel and end-cap/forward calorimeters are enclosed in separate cryostats to allow access to the inner detector and space for services. Scintillators are installed in the region between the cryostats, but the range $1.37 < |\eta| < 1.52$ remains poorly instrumented, making the precise measurement of electrons and photons difficult. In order to minimize the amount of inactive material present, the solenoid magnet and the barrel EM calorimeter share the same vacuum vessel isolating the cryostat. The thickness of the lead absorber plates is optimized for energy resolution performance, resulting in thicknesses of 1.53 mm for the range $|\eta| < 0.8$ and 1.13 mm for the range $|\eta| > 0.8$ in the case of the barrel, and 1.7 mm for the range $|\eta| < 2.5$ and 2.2 mm for the range $2.5 < |\eta| < 3.2$ for the end-cap. In addition, the calorimeter is segmented in depth, with three sections for the range $|\eta| < 2.5$ and two sections in the rest of the end-cap, where each section has increasingly coarser segmentation in η - ϕ. Finally, it may be noted that there is significant material before the calorimeter, in the inner detector itself, corresponding to a thickness of about 1-4 X_0 , and in the cryostat. A LAr presampler layer of 1.1 or 0.5 cm thickness in the barrel and end-cap regions covering the range $|\eta| < 1.8$, is used to provide an additional shower sampling inside the cryostat, where significant energy is lost in the material before reaching the EM calorimeter.

Hadronic Calorimeter

Tile calorimeter

The hadronic calorimeter, surrounding the EM calorimeter, covers the range $|\eta| < 1.7$ and is comprised of scintillating tiles alternating with steel absorbers. As the shower traverses the tiles, scintillation light is produced and the light signal from the two sides of the tiles is collected by wavelength shifting optical fibers that transport it to photomultiplier tubes. The tile calorimeter is divided into a barrel region covering the range $|\eta| < 1.0$ and two end-caps covering the range $0.8 < |\eta| < 1.7$. The thickness of the rectangular scintillating tiles is 3 mm thick, oriented parallel to the beam and divided into 64 modules in ϕ, and the surrounding absorber is 4-5 mm thick. In the radial direction, the tile calorimeter, extending in radius from 2.28 m to 4.25 m, is segmented into three regions with about 1.5, 4.1 and 1.8 λ each for the barrel region and 1.5, 2.6, and 3.3 λ for the end-cap region, with a total depth of 9.7 λ at $\eta = 0$. A steel yoke surrounding the tile calorimeter provides a support structure and the return for the solenoid field. The tile calorimeter is calibrated with Cesium sources installed throughout the active volume and with test laser pulses.

LAr hadronic end-cap calorimeter

The hadronic end-cap calorimeter covers the range $1.5 < |\eta| < 3.2$ and is comprised of two wheels per side within the same cryostat as the end-cap EM calorimeter. In order to increase the material coverage, the HEC overlaps with the tile calorimeter in the region $1.5 < |\eta| < 1.7$ and with the forward calorimeter in the range $3.1 < |\eta| < 3.2$. The front and back wheels made up

of 24 copper plates of 25 mm thickness for the front wheel and 16 plates of 50 mm thickness for the wheel further away, with LAr as the active medium filling the 8.5 mm gaps between the plates. Each wheel is divided into 32 wedge sections in ϕ and in two sections in depth, providing 4 independently read out segments in total.

LAr forward calorimeter

The forward calorimeter covers the range $3.1 < |\eta| < 4.9$ and is comprised of one EM and two hadronic components, enclosed in the end-cap cryostats. The active material is LAr and the absorber is copper for the first EM module and tungsten for the two subsequent hadronic modules. The modules are made up of copper or tungsten plates held together in a matrix by regularly spaced rods inside tubes of the same material that are placed parallel to the beam. The gaps between the rods and tubes, of size 0.269, 0.376 and 0.508 mm in each of the sections, are filled with LAr and the ionization signal is readout from the rods. Overall, the FCal has about 10 λ of depth.

3.4 Muon Spectrometer

The muon spectrometer (MS) [49] is designed to provide a precise standalone measurement of the muon momentum and a momentum-selective trigger down to a few GeV. The air-core toroid magnet system, comprised of a barrel and two end-cap magnets, provides a field integral in the range 2-8 Tm for the detector region $|\eta| < 2.7$. The superconducting coils comprising the toroid are arranged in eight-fold symmetry around the calorimeters. The field integral at

two azimuthal angles as a function of $|\eta|$ is shown in Fig. 3.5. The magnetic field provides good field integral up to $|\eta| \sim 2.6$ and poor coverage in the range $|\eta| \sim$ 1.4-1.6, corresponding to the transition region between the barrel and end-cap fields, where the fields largely cancel each other out.

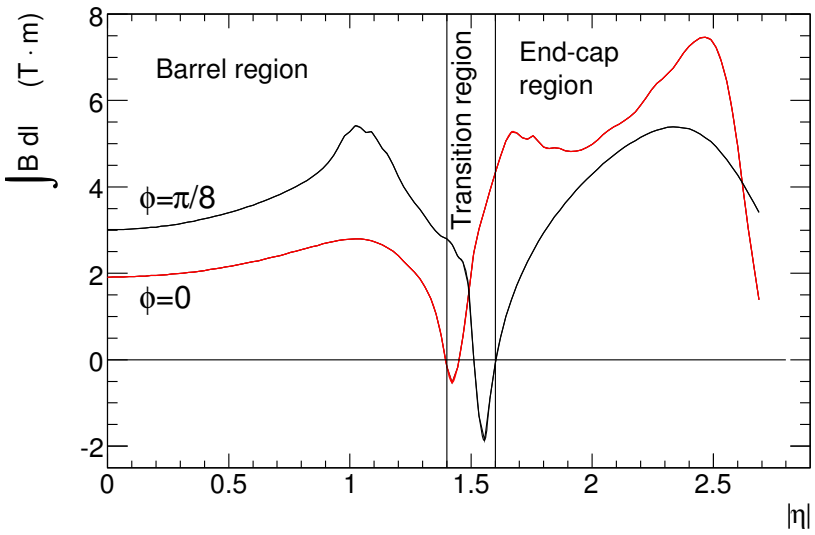

Figure 3.5: Predicted field integral as a function of $|\eta|$ from the innermost to the outermost MDT layer in one toroid octant, for infinite-momentum muons. The curves correspond to the azimuthal angles $\phi = 0$ (red) and $\phi = \pi/8$ (black).

Chamber Layout

The layout of the MS, including an $x-y$ view of the barrel region and an $R-z$ view of a quadrant is shown in Fig. 3.6. The muons typically traverse three chamber stations positioned along their trajectory from the IP. The momentum is determined from the sagitta of the track curvature as the particle bends in the magnetic field. Monitored Drift Tube (MDT) chambers cover most of the acceptance, where the wires are positioned parallel to the magnetic field, in

order to provide a measurement in the bending coordinate (z in the barrel and R in the end-cap). In the region $|\eta| > 2.0$, the precision measurement in the innermost layer is provided by Cathode Strip Chambers (CSC) that have higher rate capability and improved time resolution. In the barrel region, the three chamber layers form coaxial cylinders, while in the end-cap region they form disks centered along the beam axis. The three stations are called "Inner", "Middle" and "Outer", with their increasing distance from the IP. For the barrel these are referred to as BI (radius $R \sim 5$ m), BM ($R \sim 7.5$ m) and BO ($R \sim 10$ m) and for the end-cap as EI ($|z| \sim 7.4$ m), EM ($|z| \sim 14$ m) and EO ($|z| \sim 21.5$ m). The MS is divided into 16 sectors in the $x - y$ or ϕ plane, with 8 "large" sectors (odd numbers) and 8 "small" sectors (even numbers) that alternate the coverage in ϕ, as can be seen in Fig. 3.6. The input to the first level of muon trigger (see Sec. 4.2.1), based on the selection of muons pointing to the IP with p_T above a programmable threshold, is provided by fast tracking detectors. The trigger technologies have good time resolution for bunch-crossing identification and also provide measurement of the non-precision ϕ coordinate, along the MDT wire, with a resolution of 1 cm. Resistive Plate Chambers (RPC) cover the barrel region ($|\eta| < 1.05$) and Thin Gap Chambers (TGC) cover the end-cap region ($1.05 < |\eta| < 2.4$ for the trigger and $1.05 < |\eta| < 2.7$ for the readout). Two RPC chambers surround each MDT BM chamber, providing the low-p_T trigger, while a third chamber, mechanically attached to the MDT BO chamber, provides additional information for the high-p_T threshold triggers. In the case of the TGCs, seven detector layers arranged in order from the IP into one triplet and two doublets surround the MDT EM layer, providing the high-p_T and low-p_T threshold

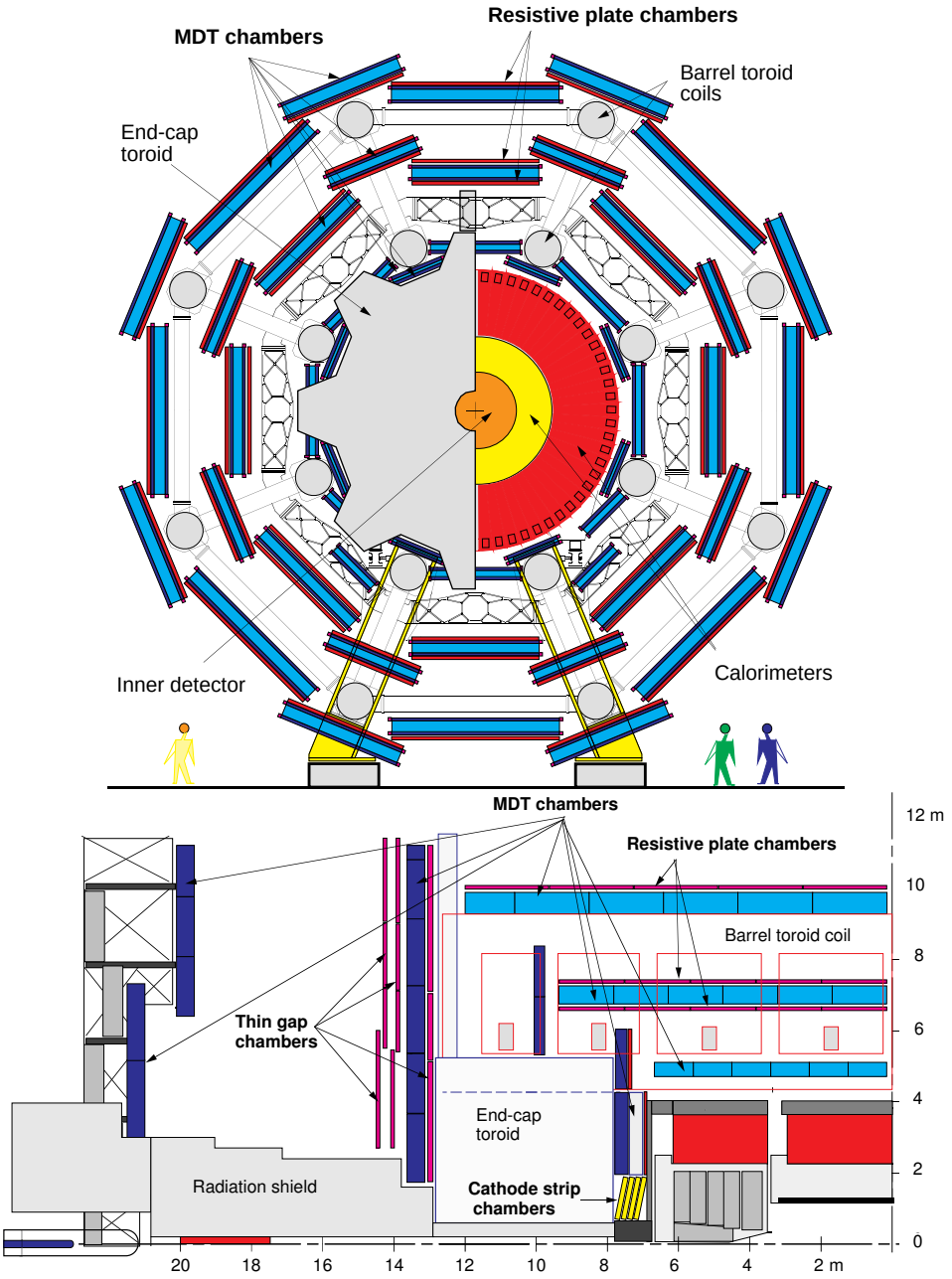

Figure 3.6: $x - y$ (top) and $R - z$ (bottom) view of the ATLAS Muon Spectrometer system.

triggers. Another layer of TGC chambers is located next to the MDT EI layer to provide an additional measurement of the non-precision or second coordinate, but is not used in the trigger.

Monitored Drift Tubes

A typical MDT chamber is composed of two multilayers (ML) of three or four layers of tubes. The chambers are rectangular in the barrel region and trapezoidal in the end-caps. The dimensions vary depending on the position, in order to maximize coverage. All drift tubes, made of an aluminum encasing, are 30 mm in diameter, with a gold-plated tungsten anode wire of 50 μm in diameter set at a voltage of 3080 V running along the center. The tubes are filled with a gaseous mixture of argon (93%), carbon dioxide CO_2 (7%) and a trace of water vapor held at a pressure of 3 bar. 150 MDT chambers (656 in the barrel and 494 in the end-cap) comprise 354000 tubes and cover an area of 5500 m^2. The operating principle of the drift tube, is based on the ionization of the gas mixture due to a traversing muon.

Cathode Strip Chambers

The CSC chambers are multiwire proportional chambers based on a cathode strip read out. When the muon traverses the chamber, electron-ion pairs are created in the gas, and a signal is measured from the charge induced in the strips. The charge information from adjacent strips is interpolated, combining them into a signal that provides a spatial resolution of about 50 μm in the radial coordinate and about 5 mm in ϕ. The technology allows for fast signal

readout, with a time resolution of 7 ns. The CSC chambers have 30700 readout channels.

Resistive Plate Chambers

An RPC chamber is composed of two plates of resistive material (plastic laminate), placed 2 mm apart and filled with a mixture of $C_2H_2F_4$/Iso-C_4H_{10}/SF_6 gas in the proportions (94.7/5/0.3)%. A muon traversing the plates experiences an average electric field of 4.8 kV/mm, creating an avalanche that is read out by two metallic strip planes mounted outside the resistive plates. Two layers of strips are placed orthogonally, providing a measurement in both the z and ϕ coordinates, with a spatial resolution of about 10 mm. The time resolution is 1.5 ns, allowing for good bunch identification. It may be noted that in the range $|\eta| < 1.05$, the geometrical coverage of the RPC chambers in η - ϕ is about 80% due to spatial constraints in the middle chamber layer, particularly from gaps for services and support structures of the toroid magnets, and the "feet" at the base of the detector. The total number of RPC channels is 359000.

Thin Gap Chambers

The design of the TGC chambers is driven by a need for a finer granularity compared to that afforded by the RPC chambers, in order to withstand higher rates and to achieve the same p_T resolution as in the barrel. A TGC chamber is also a multiwire-wire proportional chamber comprised of anode wire planes, cathode planes and strip planes held together by honeycomb support struc-

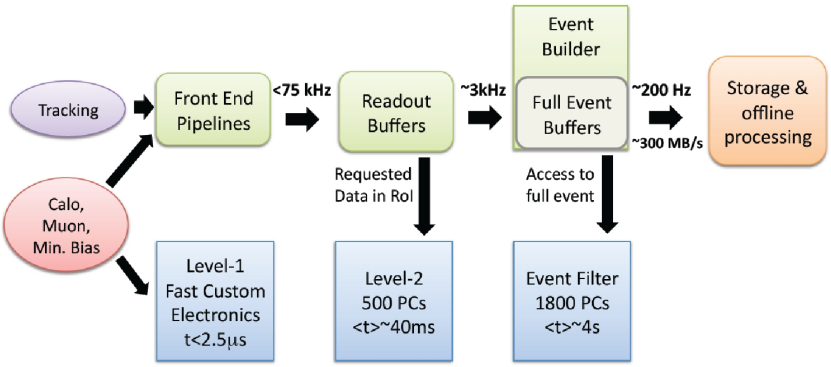

Figure 3.7: Overview of the TDAQ system showing the nominal parameters.

tures. The chamber is filled with a highly-quenching gas mixture of CO_2 and n-C_5H_{12} (n-pentane). The anode-cathode distance is smaller than the distance between adjacent anode wires and the electrodes are held at a potential of 3.1 kV, ensuring fast signal generation. The anode wires are placed parallel to the MDT tubes, while the cathode strips are arranged radially providing a ϕ measurement. The geometrical coverage of the trigger in the end-caps is about 99%. The spatial resolution of the TGCs is 2-6 mm in R and 3-7 mm in ϕ (depending on R) and the timing resolution is 4 ns. The total number of TGC channels is 318000.

3.5 Trigger and Data Acquisition

The Trigger and Data Acquisition (TDAQ) systems are designed to record approximately 200 Hz of the LHC's design 40 MHz bunch-crossing rate. An overview of the TDAQ system is shown in Fig. 3.7. The trigger system has three levels: the first level (L1) is based on limited hardware information from

the calorimeters and the MS, while the second (L2) and third (Event Filter, EF) levels (collectively called the High Level Trigger or HLT) are based on software and use increasing amounts of information from the full detector. The trigger checks each bunch-crossing for certain programmed conditions (triggers), and at each subsequent level refines the decision of the previous level by applying progressively more selective criteria. The L1 trigger provides a decision in < 2.5 μs, reducing the output rate to < 75 kHz. Upon a L1 trigger accept, the data acquisition system receives the data from each sub-detector and stores it in buffers. The data acquisition system moves data for processing and additionally allows for the configuration, control and monitoring of the hardware and software units that provide the data-taking functionality. After the final trigger decision is made, the data is written out to disk at a nominal rate of about 200 Hz with an event size of 1.3 Mbyte.

Trigger System Overview

The triggers apply criteria designed to identify physics signatures such as high-p_T electrons, photons, muons, taus, jets (including heavy flavor jets), missing transverse energy E_T^{miss} and large summed energy $\sum E_T$. The L1 trigger is based on information from a subset of the detectors. The muon trigger uses trigger chamber information from the barrel and end-cap regions of the MS. The calorimeter triggers use coarse information from all calorimeter components. The L1 muon and calorimeter triggers are processed by the Central Trigger Processor (CTP) that additionally implements a trigger "menu" that includes combinations of trigger selections. The trigger menu is reconfigured

over time in order to optimize the use of the available bandwidth as the luminosity and background conditions change. Data from events satisfying the L1 trigger are transferred to the data acquisition system for further processing. The L1 defines at least one Region-of-Interest (RoI) corresponding to a region of the detector in η - ϕ where the trigger has identified interesting features (e.g. a high-p_T muon candidate). The full granularity and precision detector information associated with the RoI is used by the L2 to further refine the selection (about 2% of data), reducing the rate to about 3.5 kHz, with an average event processing time of about 40 ms. Finally, the EF uses the same procedures as for offline analysis to reduce the final rate to about 200 Hz, with an average event processing time of about 4 s.

Muon Trigger

The L1 muon trigger is provided by a hardware-based system that selects muon candidates and identifies the corresponding bunch-crossing by processing information from the fast muon trigger detectors: RPCs in the barrel ($|\eta| < 1.05$) and TGCs in the end-cap ($1.05 < |\eta| < 2.4$). The main requirement imposed is a p_T threshold that ranges from 6 to 40 GeV. The architecture allows for up to 6 thresholds to be defined, separated into 3 low-p_T thresholds with p_T range 4-10 GeV and 3 high-p_T thresholds with $p_T > 10$ GeV. A schematic overview of the muon L1 trigger is shown in Fig. 3.8. The RPCs and TGCs use a coincidence condition in η and ϕ in two or three trigger chambers[1], depending

[1]All RPC chambers (RPC1, RPC2 and RPC3) are comprised of two detector layers, providing up to four measurements in η and ϕ. This is also the case of TGC2 and TGC3 (doublets). The chambers in TGC1 provide up to two measurements in ϕ and three in η (triplet).

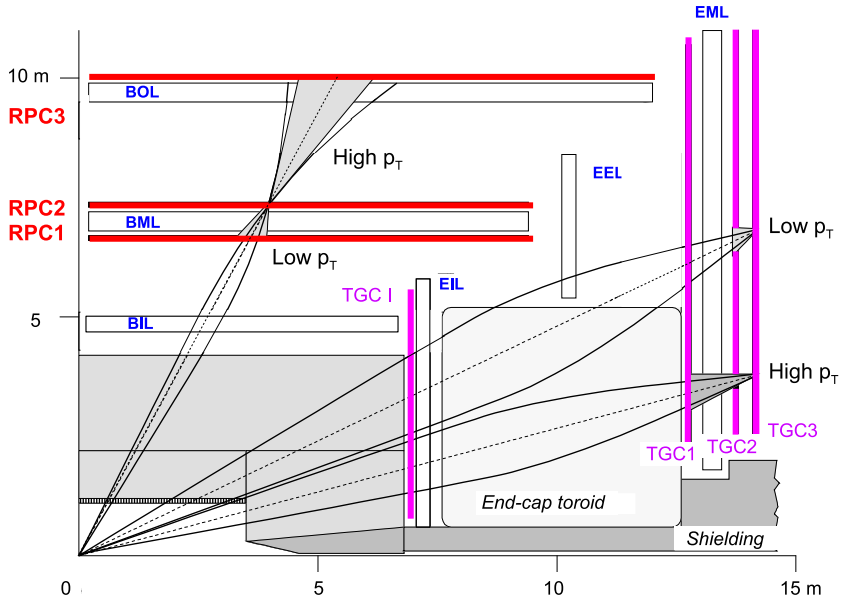

Figure 3.8: Schematic view of the muon trigger system. The triggering schemes for high-p_T and low-p_T tracks are indicated.

on the p_T of the track. The trigger logic starts with a hit in the "pivot" plane (RPC2 or TGC3) and searches for hits in the low-pT plane (RPC1 or TGC2) in a defined "trigger" associated to the same bunch-crossing. A trigger road is essentially an η - ϕ region that contains the trajectories of muons traveling from the IP with p_T above a particular threshold.

If a corresponding hit coincidence is found, based on hits in at least three out of the four trigger detector layers in η and ϕ, a low-p_T trigger is issued. The logic then searches for additional hit coincidences in the third high-p_T plane (RPC3 or TGC1), checking for at least one additional hit in the case of the RPC and one ϕ hit and two out of three η hits for the TGC. If the coincidence requirements are satisfied, a high-pT trigger is issued. The coincidences in η and ϕ are issued separately, and combined to produce the final RPC or TGC

trigger result. Overlaps between the RPC and TGC triggers are subsequently addressed in additional trigger logic in the CTP.

Data Acquisition

The data acquisition system works together with the trigger and is tasked with the movement of data from the detector to mass storage. When a L1 trigger accept is issued, the data from the front-end pipelines are transferred to the Read Out Drivers (ROD). The RODs, which are specific to each sub-detector, gather the data from several front-end streams, buffering and multiplexing it, formatting it to conform to the general ATLAS format, and subsequently sending it to the Readout Buffers (ROB). Subsets of the data, associated with the RoIs, are requested by the L2 trigger and sent to a L2 processing farm. The events accepted by the L2 are sent to the Event Builder and subsequently the EF decision is made. If an event is accepted, it is transmitted for permanent storage at the CERN computer center.

Chapter 4

Data Samples and Event Selection

4.1 Data Sample and Integrated Luminosity

Before the description of the collision data and of the procedure to select muons produced in the Z/γ^* boson decay, it is worth to have a deeper look on how the Z/γ^* boson is produced at the LHC.

4.1.1 Z/γ^* Boson Production at the LHC

The main Z/γ^* boson production mechanism at the LHC is the Drell-Yan process $Z/\gamma^* \rightarrow \mu\mu$, as illustrated in Fig. 4.1. This process may or may not involve initial-state gluon radiation. Higher-order processes with multiple radiated gluons in the final state have a small contribution.

Fig. 4.3 shows the production cross-sections for various Standard Model processes as a function of the center-of-mass energy, calculated to NLO accu-

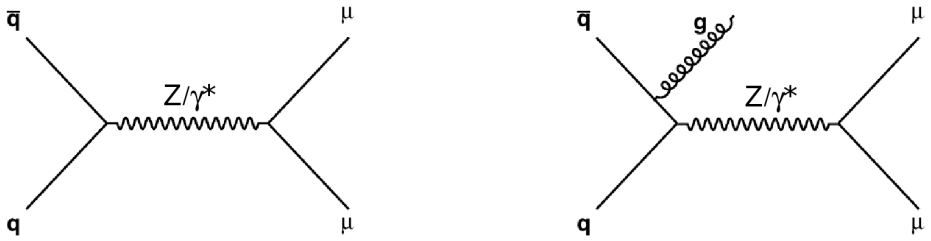

Figure 4.1: *Left*: Z/γ^* boson production through the Drell-Yan channel, *i.e.*, $q\bar{q}$ annihilation. *Right*: Drell-Yan Z/γ^* boson production accompanied by initial-state gluon radiation. This is an NLO process.

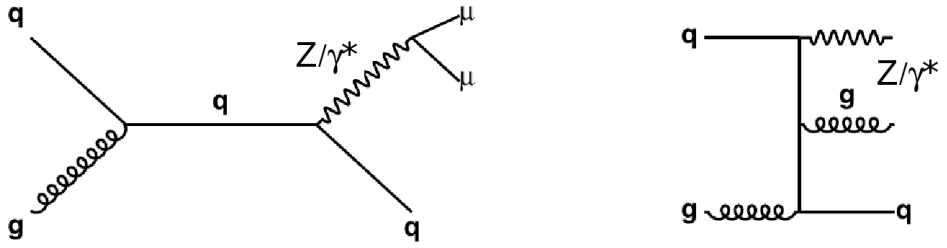

Figure 4.2: *Left*: Z/γ^* boson production through gluon Compton scattering. This is a $Z/\gamma^* + 1$ jet event. *Right*: A $Z/\gamma^* + 2$ jet event. This is a NNLO process.

racy in perturbative QCD [50].

As can be seen from Fig. 4.3, the total Z/γ^* production cross-section at a collision energy of 7 TeV is $\sim$ 30 nb. The branching fraction of the decay $Z/\gamma^* \rightarrow \mu\mu$ is $\sim$ 3.366% [14], which gives a cross-section of $\sim$ 1 nb for the inclusive decay mode $Z/\gamma^* \rightarrow \mu\mu + X$, where X represents any other final state particle/s.

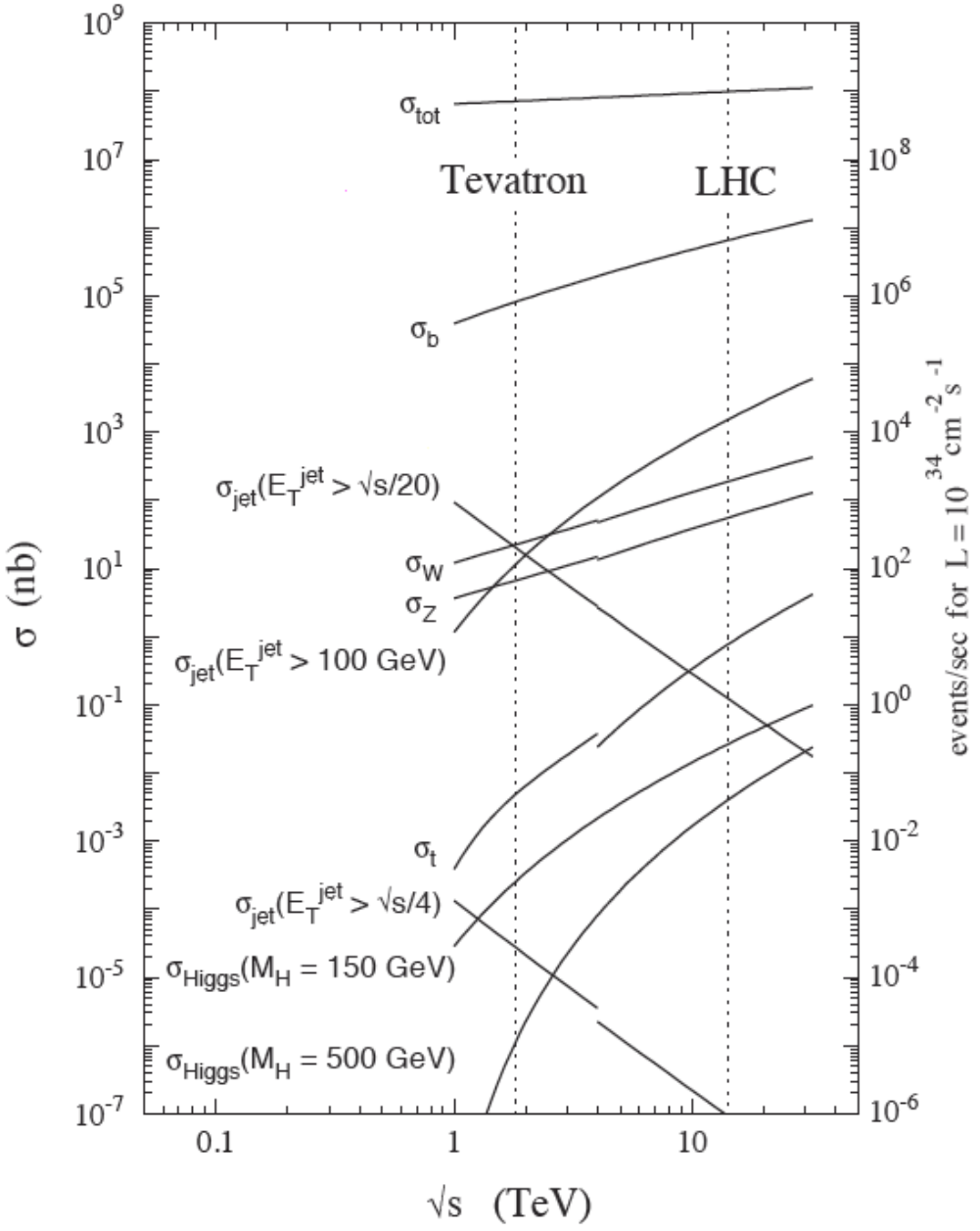

Figure 4.3: Total cross-sections for a number of SM processes at the Tevatron and at the LHC at respective nominal collision energies of 1.8 TeV and 14 TeV. The right axis shows the number of events expected per second at an instantaneous luminosity of $10^{34}\text{cm}^{-2}\text{s}^{-1}$.

4.1.2 Collision Data

The LHC started operating on September 10th, 2008, when first proton beams were successfully circulated in the main ring of the LHC for the first time, but 9 days later operations were halted due to a serious fault.

On November 20th, 2009 they were successfully circulated again, with the first recorded proton-proton collisions occurring 3 days later at the injection energy of 450 GeV per beam. After the 2009 winter shutdown, the LHC was restarted and the energy was ramped up to 3.5 TeV per beam.

On March 30th, 2010, the first planned collisions took place between two 3.5 TeV beams, a new world record for the highest-energy man-made particle collisions. The ATLAS experiment collected about 40 pb^{-1} of collision data. After another shutdown on December 6th, 2010 new runs with proton beams begun on March 13th, 2011: this thesis is based on proton-proton collision data collected until the 2011 winter shutdown on December 8th.

Fig. 4.4(a) shows the cumulative luminosity versus day delivered to (green) and recorded by (yellow) ATLAS during stable beams and for proton-proton collisions at 7 TeV centre-of-mass energy in 2011. The delivered luminosity accounts for the luminosity delivered from the start of stable beams until the LHC requests ATLAS to turn the sensitive detectors off to allow a beam dump or beam studies. The plot shows the luminosity as determined from counting rates measured by the luminosity detectors. These detectors have been calibrated with the use of the *van-der-Meer* (*vdM*) beam-separation method, where the two beams are scanned against each other in the horizontal and vertical planes to measure their overlap function [51]. At the end of proton-proton

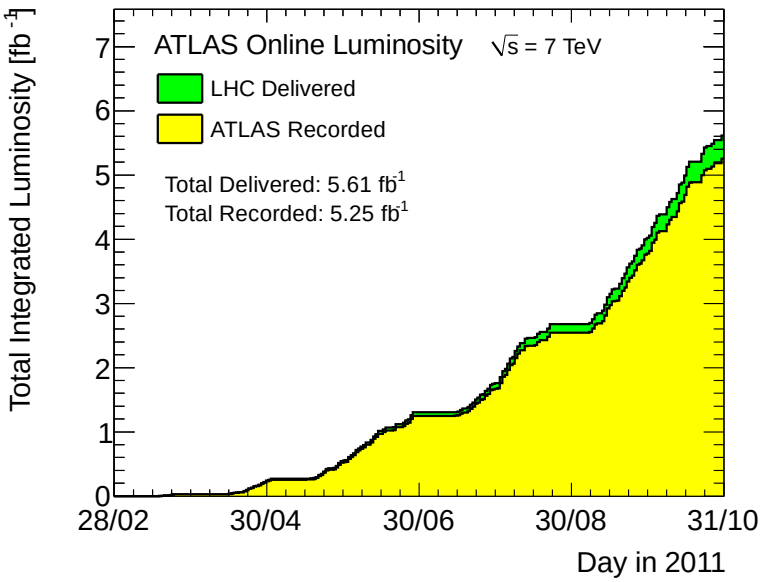

(a) Total integrated luminosity in 2011 in proton-proton run

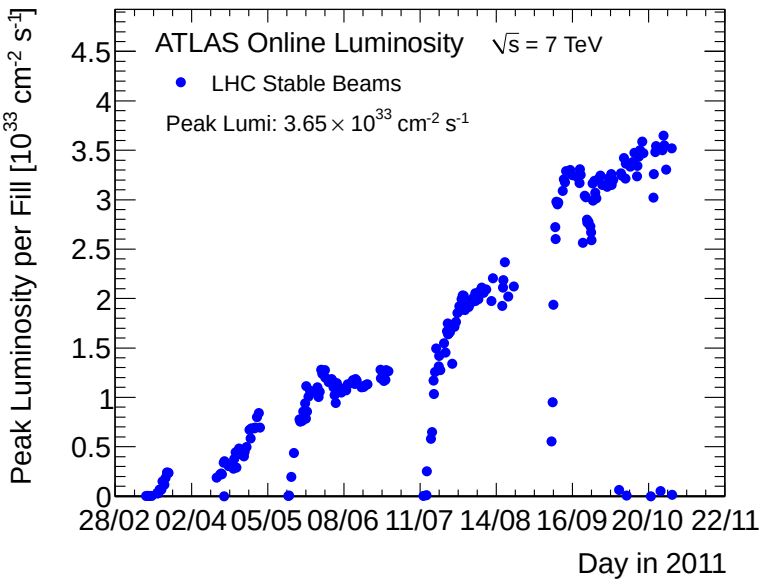

(b) Peak luminosity in 2011 in proton-proton run

Figure 4.4: Total (a) and peak (b) luminosity versus day in 2011 proton-proton run.

operations the total integrated luminosity collected by the ATLAS detector is 5.25 fb^{-1} with an overall data taking efficiency with respect to the total LHC delivered luminosity of about 93 %. The relative uncertainty on the luminosity scale applied to the 2011 proton-proton data at $\sqrt{s} = 7$ TeV, including the extrapolation of the *vdM* scan calibration to the entire 2011 data sample, is found to be $\delta\mathcal{L}/\mathcal{L} \pm 3.7$ % [51].

This analysis uses data taken in the year 2011 with proton beam energies of 3.5 TeV. The analyzed luminosity is lower with respect to the one reported above because data quality requirements have been applied to the full 2011 sample. Net of these requirements, the available luminosity is about 5.1 fb^{-1} as shown in Tab. 4.1, where the whole 2011 data sample is grouped in data periods[1] with the corresponding integrated luminosity.

Fig. 4.4(b) shows the maximum instantaneous luminosity versus day delivered to ATLAS. The luminosity determination is the same as described above for the integrated luminosity. The peak luminosity during stable beam periods is shown and the peak value is $3.65 \times 10^{33}\text{cm}^{-2}\text{s}^{-1}$, more than one third of the design luminosity (cfr. Chap. 2).

4.1.3 Simulated Monte Carlo Samples

Simulated ATLAS Monte Carlo samples are used to model the properties of our signal and backgrounds, as well as to correct for several experimental effects, as detailed in Chap. 6.

The main signal event sample for Z/γ^* production is generated using the

[1] A data period is defined as a set of data taken with stable detector conditions and LHC operating parameters.

Data Period	Number of Runs	Run Number Range	Integrated Luminosity (fb^{-1})
B	03	178044 - 178109	0.013
D	23	179710 - 180481	0.183
E	05	180614 - 108776	0.052
F	15	182013 - 182519	0.154
G	28	182726 - 183462	0.562
H	13	183544 - 184169	0.276
I	26	185353 - 186493	0.403
J	09	186516 - 186755	0.233
K	19	186873 - 187815	0.665
L	45	188921 - 190343	1.468
M	32	190608 - 191933	1.106
Total	218		5.119

Table 4.1: Data periods for analysis and corresponding integrated luminosity

Pythia event generator. All generators are interfaced to Photos [52] to simulate the effect of final state QED radiation. Passage of particles through the ATLAS detector is modeled using GEANT4 [53].

The effect of multiple interactions per bunch crossing ("pileup") is modeled by overlaying simulated minimum bias events over the original hard-scattering event (cfr. Sec. 4.4 below).

Tab. 4.2 summarizes the simulated Monte Carlo samples used in this thesis and their main properties.

4.2 Muon Trigger, Reconstruction and Identification

4.2.1 Muon Trigger

The muon trigger consists in 3 stages called Level 1 (L1), Level 2 (L2) and Event Filter (EF), the first being fully hardware based, while the remaining

Process	Data set	Generator	$\sigma\cdot$ BR $\cdot\epsilon_{filter}$ [nb]	N_{evt} [10^6]
$Z/\gamma^* \to \mu\mu$	106047	PYTHIA	0.99±0.05	5
$Z/\gamma^* \to \tau\tau$	106052	PYTHIA	0.99±0.05	2
$W \to \mu\nu$	106044	PYTHIA	10.46±0.52	7
$W \to \tau\nu$	107054	PYTHIA	10.46±0.52	2
$b\bar{b}$	108405	PYTHIAB	73.9	4.4
$c\bar{c}$	106059	PYTHIAB	28.4	1.5
$t\bar{t}$	105861	POWHEG PYTHIA	(0.16±0.01)·0.555	1
WW	105985	HERWIG	$44.9 \cdot 0.389 \cdot 10^{-3}$	0.25
WZ	105987	HERWIG	$18.5 \cdot 0.310 \cdot 10^{-3}$	0.25
ZZ	105986	HERWIG	$6.02 \cdot 0.212 \cdot 10^{-3}$	0.25

Table 4.2: Monte Carlo samples used in this analysis. The cross-sections quoted are the ones used to normalize estimates of expected number of events.

two are software based and provide a more precise reconstruction and tighter trigger selection [48]. A variety of muon triggers are implemented at each stage both for physics studies and monitoring purposes. The L1 trigger is based on Resistive Plate Chambers (RPC) in the barrel ($|\eta| < 1.05$) and Thin Gap Chambers (TGC) in the end-cap ($|\eta| > 1.05$). Additional detectors called Monitored Drift Tubes (MDT) are also used for improving the transverse momentum measurement. To define muon candidates, both detectors apply coincidence of hits in several layers within a region of interest whose size depends on the imposed p_T threshold. Six programmable thresholds are defined at L1 to seed the L2 and EF algorithms. At L2 the candidate from L1 is refined including the precision data from the MDTs. The L2 Muon System (MS) standalone algorithms access the data in a Region-of-Interest (RoI) defined by the L1 candidate and the momentum and track parameters of the muon candidate are refined by fast fitting algorithms and Look-up-tables (LUTs) using the MDT drift times. Additionally, the L2 muon combined algorithm uses the Inner Detector (ID) tracks to combine the muon candidate reconstructed

with data from the MS with tracks from the ID to refine the track parameters resolution and to perform the rejection of muons from in-flight decays of light mesons and from cosmics. At the EF level the full event data are accessible. The muon reconstruction starts from the RoI identified by L1 and L2, reconstructing segments and tracks from the trigger and precision chambers. The track is then extrapolated to the interaction region to form a muon candidate using either data only from the MS (EFMS only trigger) or combined with the ID information to form EF combined muon candidates.

The trigger used for the analysis is EF_mu18_MG, corresponding to a threshold at $p_T = 18$ GeV, for periods D to I. After that, trigger EF_mu18_MG_medium is used. Both triggers are based on the MuonGirl algorithm, requiring a track in the inner-detector matching to a track segment in the internal muon trigger chambers, with the only difference that EF_mu18_MG is seeded by L1_MU10 (L1 trigger with threshold $p_T = 10$ GeV) while EF_mu18_MG_medium by the L1_MU11 L1 trigger.

4.2.2 Muon Reconstruction

4.2.2.1 Muon Type

Muons are identified and reconstructed in ATLAS by exploiting several subdetectors in order to cover a wide range of p_{T} and pseudo-rapidity ($|\eta|<2.7$). Muons can be defined as:

- standalone muons: these are reconstructed using the muon system information only. The reconstruction proceeds from the muon chambers by searching for straight segments in the bending plane and requiring that

candidates to be pointing to the centre of ATLAS. At least two segments in two different muon stations are required to form a muon track. The track parameters are evaluated and extrapolated to the interaction point, including the effect of multiple scattering and the measurement of the energy loss in the calorimeter and a parametrization of the energy loss in the dead materials;

- combined muons: these are muons for which the standalone track has been associated, via a χ^2-fit of the track parameters, to an inner-detector track including pixel, SCT and TRT information. The track parameters associated to the muon candidate are calculated at the point of closest approach to the beam axis either with a full re-fit of the track (MuId) or from a statistical combination of the track parameters (STACO).

In order to achieve the best possible muon resolution and a high fake-muons rejection, only combined muons are used which guarantee an optimal muon reconstruction with a limited loss of reconstruction efficiency (less than 1% of Monte Carlo muons have no combined track). These category of tracks extend up to $|\eta|= 2.5$, limited by the coverage of the Inner Detector. However since the muon trigger system extends only to $|\eta|= 2.4$, also the reconstructed tracks are selected up to that value of pseudo-rapidity to assure full trigger coverage. Moreover the STACO algorithm has been adopted for the track parameters evaluation, although the results obtained with the alternative MuId algorithm were also studied and final results are found to be consistent.

Once the muons have been selected, this analysis uses their kinematic quantities as measured by the inner tracker. This is meant to make the result less

dependent on relative misalignment between MS and ID, which would affect the combined measurement.

Charge misidentification for muons is expected to be very low, and its effect on this analysis is therefore not considered at this stage.

4.2.2.2 Muon Quality

Quality cuts are applied to the associated inner-detector tracks in order to ensure the best reconstruction. These are:

- if hits in the *b*-layer are geometrically expected, then the muon track must have at least one *b*-layer hit;
- $N_{PIX} + N_{DEAD-PIX} > 1$, where N_{PIX} is the number of pixel hits and $N_{DEAD-PIX}$ is the number of crossed dead pixel sensors;
- $N_{SCT} + N_{DEAD-SCT} \geq 6$, where N_{SCT} is the number of SCT hits and $N_{DEAD-SCT}$ is the number of crossed dead SCT sensors;
- $N_{DEAD-PIX} + N_{DEAD-SCT} < 2$;
- a successful TRT extension is required in the eta acceptance of the TRT. If $N_{TRT-HITS}$ denote the number of TRT hits on the muon track, $N_{TRT-OUTLIERS}$ the number of TRT outliers on the muon track, and $N_{TRT} = N_{TRT-HITS} + N_{TRT-OUTLIERS}$, then
  - in the interval $|\eta| < 1.9$: $N_{TRT} > 5$ and $N_{TRT-OUTLIERS}/N_{TRT} < 0.9$ is required;
  - in the interval $|\eta| > 1.9$: if $N_{TRT} > 5$ then $N_{TRT-OUTLIERS}/N_{TRT} < 0.9$ is required, otherwise the muon is accepted.

4.2.2.3 Extrapolation to Beam Axis

In addition to the listed quality cuts, muons are required to be compatible with coming from the primary vertex from which the Z/γ^* is expected to emerge. This cut is mainly aimed to suppress the background from cosmics. We require the z coordinate of the maximum approach of the muon to the beam axis to be compatible with the corresponding coordinate of the primary vertex within 10 mm ($|z_{extr} - z_{PV}| < 10$ mm).

4.2.2.4 Muon Isolation

Muons from Z/γ^* decay are expected to be isolated from other tracks and in particular from jets, in contrast to some of the main background sources due to heavy-hadrons decays. Moreover background muons can come from in-flight decays of pions and kaons. In order to reject these sources of background, an isolation cut is applied to the muons at the inner-detector level. The p_T of all the tracks are summed in a cone of radius $\Delta R = 0.2$ around the muon candidate and a cut on the quantity:

$$I_\mu = \frac{\sum_{tracks} p_T}{p_T^\mu} < 0.1 \tag{4.2.1}$$

is applied. The optimal cone radius $\Delta R = 0.2$ and the isolation cut value were determined by comparing the rejection power for muons from non-prompt sources compared to the efficiency for Z/γ^* decay muons.

4.3 Z/γ^* Candidate Event Selection

Events are required to have at least one primary vertex reconstructed using at least 3 tracks and a cut is applied on the vertex position in order to suppress the background from cosmics. It is required that the z-position of the primary vertex fulfills the following condition: $|z_{vtx}| < 200$ mm. Additional to the vertex cuts, the following selection criteria are applied:

- events are triggered with EF_mu18_MG or EF_mu18_MG_medium depending on data acquisition period;
- at least 2 combined muons must be reconstructed in the selected events;
- the selected muons must have $p_T > 20$ GeV and $|\eta| < 2.4$;
- the selected muons must fulfill the quality requirements described in Sec. 4.2.2.2;
- the selected muons must fulfill the extrapolation to the beam axis requirement described in Sec. 4.2.2.3;
- the selected muon(s) must fulfill the isolation requirement described in Sec. 4.2.2.4;
- only opposite charge pairs are used;
- the di-muon invariant mass must be in the range $60 < m_{\mu\mu} < 1000$ GeV.

In Tab. 4.3 the list of applied cuts for the $Z/\gamma^* \rightarrow \mu\mu$ selection is reported.

Fig. 4.5(a), Fig. 4.5(b), Fig. 4.6(a) and Fig. 4.6(b) show the distributions of several kinematic quantities for the $Z/\gamma^* \rightarrow \mu\mu$ candidates, as selected by

Data Quality Requirements	
Primary Vertex	$N_{vtx} \geq 1$ with $N_{tracks} \geq 3$ and $\lvert z_{PV} \rvert < 200$ mm
Trigger	EF_mu18_MG or EF_mu18_MG_medium
Muon quality	≥ 2 combined muon
p_T and $\lvert\eta\rvert$	$p_T > 20$ GeV; $\lvert\eta\rvert < 2.4$
Muon quality cuts	
z-extrapolation	$\lvert z_{extr} - z_{PV} \rvert < 10$ mm
Isolation	$\frac{\sum_{tracks} p_T}{p_T^{\mu}} < 0.1$ in a cone of $\Delta R = 0.2$
Opposite charge	$c_1 \cdot c_2 < 0$
Invariant mass	$60 < M_{\mu\mu} < 1000$ GeV

Table 4.3: List of cuts applied for the $Z/\gamma^* \to \mu\mu$ selection.

the cuts described above. For comparison, the PYTHIA MC prediction is superimposed.

Tab. 4.4 shows the number of data events surviving the selection described above. For reference, Tab. 4.5 shows the same results, obtained with the signal MC.

4.4 Pile-up Simulation and Re-weighting

Additional proton-proton interactions occurring in the same and previous bunch crossings can produce particles overlapping with the main interaction triggering the event. This is referred to as out-of-time and in-time pileup, respectively. The in-time pileup results in additional reconstructed primary vertexes.

The increased event activity can influence the efficiency of event selection through additional tracks (lepton isolation). To model the pile-up effects on our efficiency for signal and background, we use simulated MC samples with the so called *bunch train pileup-setup*. Here simulated minimum bias interactions are

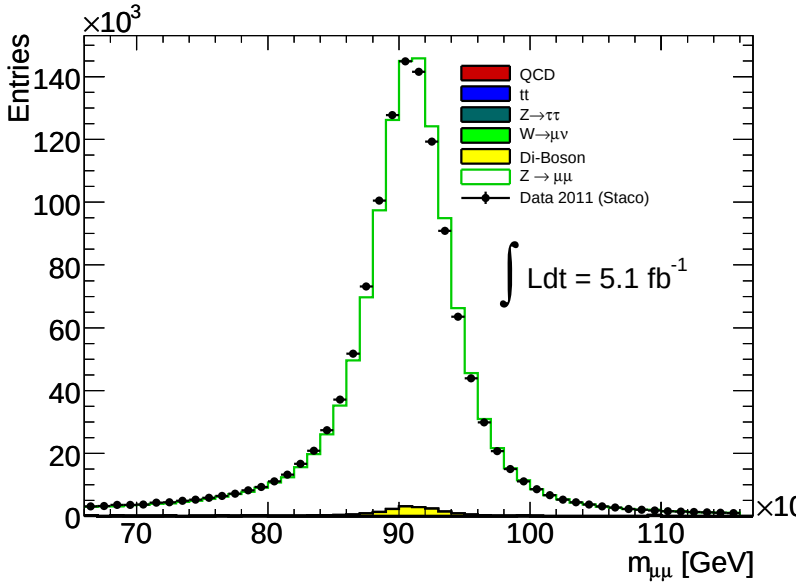

(a)

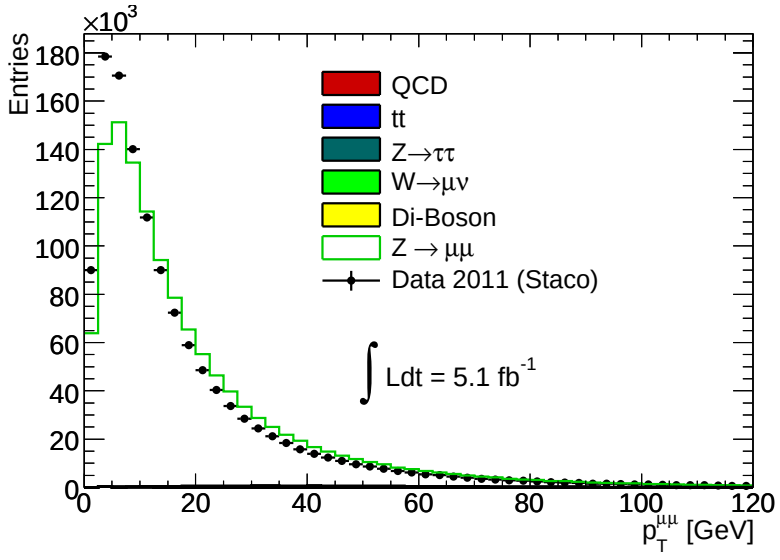

(b)

Figure 4.5: Invariant mass (a) and transverse momentum (b) distributions of candidate Z/γ^* bosons. The simulation is normalized to the data.

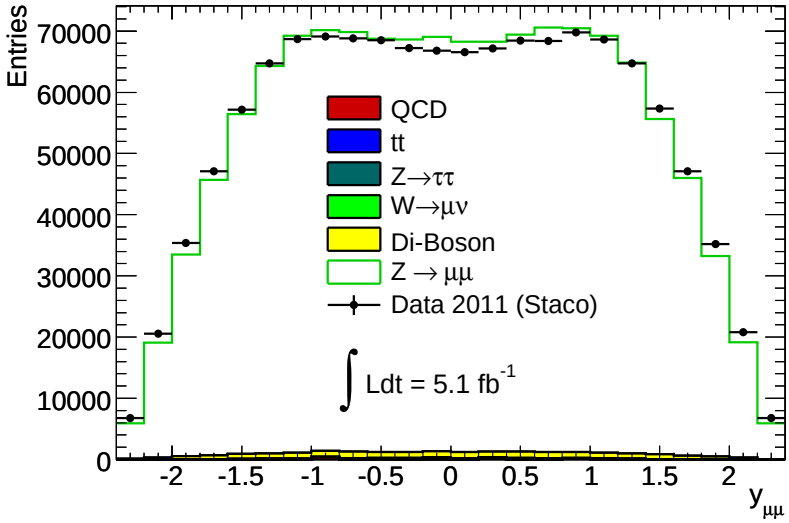

(a)

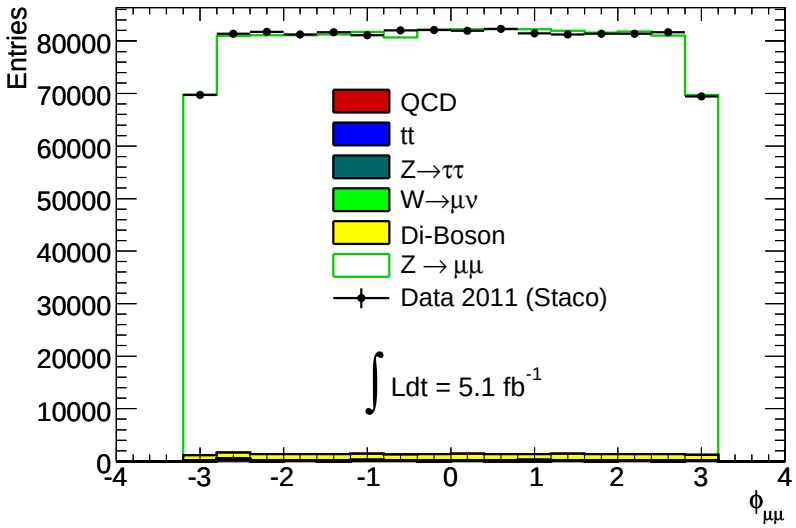

(b)

Figure 4.6: Rapidity (a) and azimuthal angle (b) distributions of candidate Z/γ^* bosons. The simulation is normalized to the data.

Data			
Cut	**Number of Events** [10^6]	**Rel. Efficiency** [%]	**Abs. Efficiency** [%]
All	13.331 ± 0.004	100	100
Good Run List	12.190 ± 0.003	91.441 ± 0.051	91.441 ± 0.051
Trigger	6.643 ± 0.003	54.496 ± 0.037	49.832 ± 0.044
Vertex	6.628 ± 0.003	99.776 ± 0.077	49.721 ± 0.044
Preselection	1.762 ± 0.001	26.586 ± 0.030	13.219 ± 0.035
$\|\eta\| < 2.4$	1.664 ± 0.001	94.409 ± 0.144	12.480 ± 0.035
Quality	1.615 ± 0.001	97.066 ± 0.152	12.113 ± 0.035
$\|z_{extr} - z_{PV}\| < 10$ mm	1.613 ± 0.001	99.861 ± 0.157	12.097 ± 0.035
Isolation	1.403 ± 0.001	86.995 ± 0.142	10.523 ± 0.034
Opposite charge	1.402 ± 0.001	99.943 ± 0.169	10.517 ± 0.034
Z mass window	1.306 ± 0.001	93.180 ± 0.160	9.800 ± 0.034

Table 4.4: Number of events in data sample passing each selection cut. Absolute and relative efficiency of each cut are also shown.

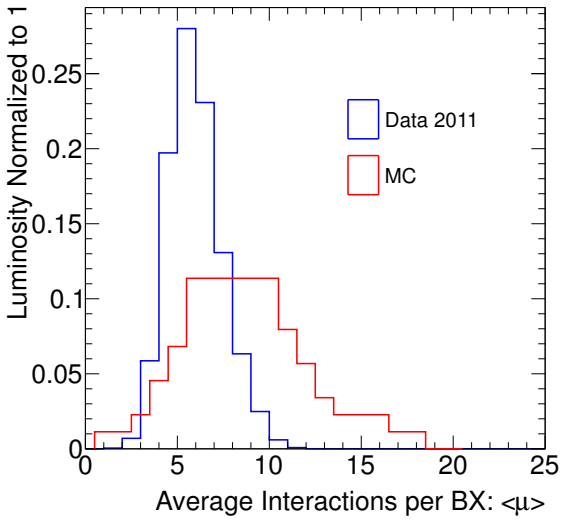

Figure 4.7: Integrated luminosity versus average number of interactions per bunch crossing.

Monte Carlo signal			
Cut	**Number of Events** [$\mathbf{10^6}$]	**Rel. Efficiency** [%]	**Abs. Efficiency** [%]
All	4.708 ± 0.002	100	100
Good Run List	4.708 ± 0.002	100.000 ± 0.092	100.000 ± 0.092
Trigger	3.515 ± 0.002	74.667 ± 0.074	74.667 ± 0.086
Vertex	3.444 ± 0.002	97.977 ± 0.105	73.157 ± 0.086
Preselection	2.003 ± 0.001	58.145 ± 0.072	42.537 ± 0.076
$\|\eta\| < 2.4$	1.883 ± 0.001	94.048 ± 0.135	40.005 ± 0.075
Quality	1.838 ± 0.001	97.603 ± 0.143	39.046 ± 0.075
$\|z_{extr} - z_{PV}\| < 10$ mm	1.836 ± 0.001	99.859 ± 0.147	38.991 ± 0.075
Isolation	1.809 ± 0.001	98.522 ± 0.146	38.415 ± 0.075
Opposite charge	1.809 ± 0.001	99.999 ± 0.149	38.415 ± 0.075
Z mass window	1.755 ± 0.001	97.058 ± 0.145	37.284 ± 0.074

Table 4.5: Number of events in Monte Carlo signal sample passing each selection cut. Absolute and relative efficiency of each cut are also shown.

overlaid on top of the hard-scattering event with the timing structure described below.

During the 2011 LHC running, the machine parameters evolved over time resulting in variations of the number of interactions occurring per bunch crossing and in the distance between consecutive bunches. Once the LHC started running with bunch trains with an in-train bunch separation of 50 ns, also the out-of-time pileup (overlapping signals in the detector from other neighboring bunch crossings) is very important. To account for this effect one needs to use in most analysis cases the average number of pile-up interactions $< \mu >$.

Fig. 4.7 shows the luminosity recorded versus the average number of interactions per bunch crossing. A reweighting dependent on the average number of interactions per bunch crossing is applied to the Monte Carlo.

Chapter 5

Muon Performance

This chapter presents the muon performance in the high-p_T domain which is relevant for the Z/γ^* A_{fb} measurement.

Since A_{fb} is measured correcting detector level distributions using the Monte Carlo prediction, differences between data and simulation need to be accounted for applying proper scale factors (SFs) to correct the Monte Carlo simulation. These factors are derived measuring the muon trigger and reconstruction efficiencies with data-driven techniques (cfr. Sec. 5.1) and comparing with the Monte Carlo expectations.

These results are then used to correct pure Monte Carlo selection efficiencies predictions. Muon momentum scale and resolution are also extracted from data and results are given in Sec. 5.2.

5.1 Muon Efficiencies

The measurement of the muon trigger and reconstruction efficiencies from data is presented in this section and compared to the Monte Carlo expectations. Efficiencies are measured with a "tag-and-probe" technique based on the $Z/\gamma^* \rightarrow \mu\mu$ process. This method is often used for muon performance determination because it has a good background rejection power, due to the strong correlation between the muons coming from a Z/γ^* decay.

5.1.1 $Z/\gamma^* \rightarrow \mu\mu$ "tag-and-probe" method

The method is based on the kinematic and dynamic correlations between the muons coming from the Z/γ^* boson decay. The idea is to tag one of the two muons with tight criteria, then take advantage of the correlation to select the second muon (to be used as probe to test the efficiencies) with high purity, despite never using the system it is meant to test. In particular, the Z/γ^* mass constraint is fundamental in order to guarantee a pure selection and suppress the background. Different kinds of probe tracks are used depending on the efficiency term that is measured. They are defined as:

- *ID-probes*: tracks reconstructed by the inner detector, fulfilling some kinematic and quality requirements to reject the background. The combined reconstruction efficiency is then measured matching these tracks to a combined reconstructed muon, selected with the same cuts used in the Z/γ^* analysis. The efficiency measured is therefore relative to the inner detector one and accounts for the probability of finding a muon in the muon spectrometer and matching it to the inner track to form a

combined muon;

- *MS-probes*: tracks reconstructed by the muon spectrometer, fulfilling some kinematic and quality requirements to reject the background. The inner tracker efficiency is then measured matching these tracks to inner detector ones. It has to be noted this is still a relative efficiency measurement, since small correlations in finding a track in the two sub-detectors can be present;

- *CB-probes*: combined muon tracks, fulfilling kinematic and quality requirements to reject the background as applied for the Z/γ^* analysis.

In order to avoid a large background contamination the ID-probes and MS-probes are required to be isolated.

Naming x the number of successful matches and N the number of trials (e.g. selected probes), in both cases the efficiency is then calculated using a Frequentist approach for a binomial distribution $\epsilon = x/N$, with the Neyman construction to determine the associated statistical uncertainty [54]:

$$\epsilon^{\pm} = \frac{(2\epsilon + 1/N) \pm \sqrt{4\epsilon(1-\epsilon)/N + 1/N^2}}{2(1 + 1/N)}$$

All efficiency measurements are done correcting the Monte Carlo to match the muon momentum resolution that has been measured in data, as explained in Sec. 5.2.

5.1.2 Trigger Efficiency Results

For Z/γ^* A_{fb} measurement, a muon trigger has been used to select the events: EF_mu18_MG which is seeded by the L1_MU10 for the whole 2011 data period. To associate a probe muon with a trigger object, a ΔR cone size of 0.2 has been used. In order to remove bias of the trigger efficiency measurements, tag muons have also been required to match with EF_mu18_MG.

Trigger efficiencies and scale factors have been derived as shown in Figures 5.1.

Data corresponding to an integrated luminosity of 138.5 pb^{-1}, taken in the first months of 2011 has been used to perform these studies.

Results of efficiency measurements with data and Monte Carlo together with the corresponding scale factors are summarized in Table 5.1. These values have been used in the analysis to correct the predictions of simulation.

EF_mu18_MG Efficiency		
Data	MC	SF
0.8125 ± 0.0015	0.7902 ± 0.0002	1.0283 ± 0.0016

Table 5.1: Summary of the overall EF_mu18_MG trigger efficiency for Staco algorithms. The data efficiency is compared to the Monte Carlo expectations and the scale factor is derived. Only statistical uncertainties are reported.

The data/MC scale factor is about 2%, i.e. data efficiency is higher then MC. This reflects the improvements in the detector operation point tuning not yet propagated to the simulation.

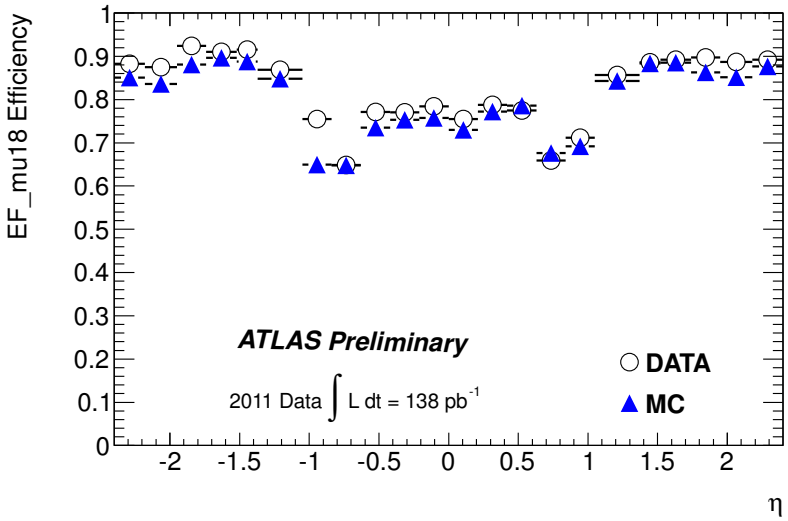

(a) Trigger efficiency in terms of η.

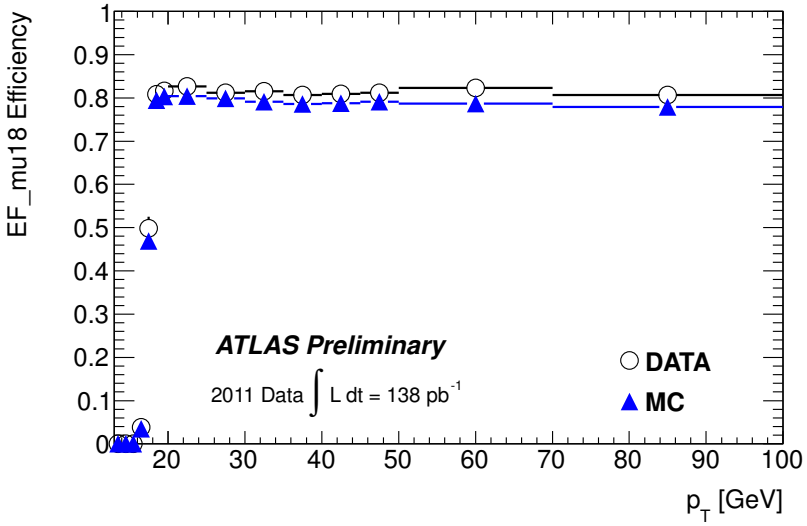

(b) Trigger efficiency in terms of p_{T}.

Figure 5.1: EF_mu18_MG trigger efficiency with respect to Staco combined muon from data, compared to the Monte Carlo expectation.

5.1.3 Reconstruction Efficiency Results

The method used to determine the reconstruction efficiencies is described in details in [55]. The results used correct the Monte Carlo simulation are shown below.

5.1.3.1 Muon spectrometer and ID-MS combination efficiency

According to the description of the "tag-and-probe" method (cfr. Sec. 5.1.1), ID-probes have been selected to measure the reconstruction efficiency of the muon spectrometer tracks plus the combination to ID tracks ($MS + CB$).

To determine the $MS+CB$ reconstruction efficiency, the number of probes which can be matched to a combined reconstructed muon, as selected in the Z/γ^* analysis, has been counted. A probe is considered to match a combined track if it is found within $\Delta R < 0.01$.

$MS + CB$ **Reconstruction Efficiency and SF**			
	Data	MC	SF
$\epsilon_{cb\|id}$	0.9177 ± 0.0021	0.9243 ± 0.0002	0.9929 ± 0.0023

Table 5.2: Summary of the tag-and-probe $MS+CB$ reconstruction efficiencies (as explained in the text). The background subtracted data measurement is compared to the Monte Carlo expectations and the relative SF is derived.

The overall efficiencies measured from data and compared with the expected efficiencies from the $Z/\gamma^* \rightarrow \mu\mu$ Monte Carlo simulation are summarized in table 5.2. The data-MC efficiency comparison shows that a correction SFs close to unity has to be applied to the predicted selection efficiency for the cross-section measurement.

The efficiency, as well as the related SFs, as a function muon pseudorapidity

η is shown in Fig. 5.2. The efficiency dip at $|\eta| \sim 0$ is expected due to the fact that in the centre of the detector a gap in chamber coverage has been left open to allow for services to the solenoid magnet, the calorimeters and the inner detector.

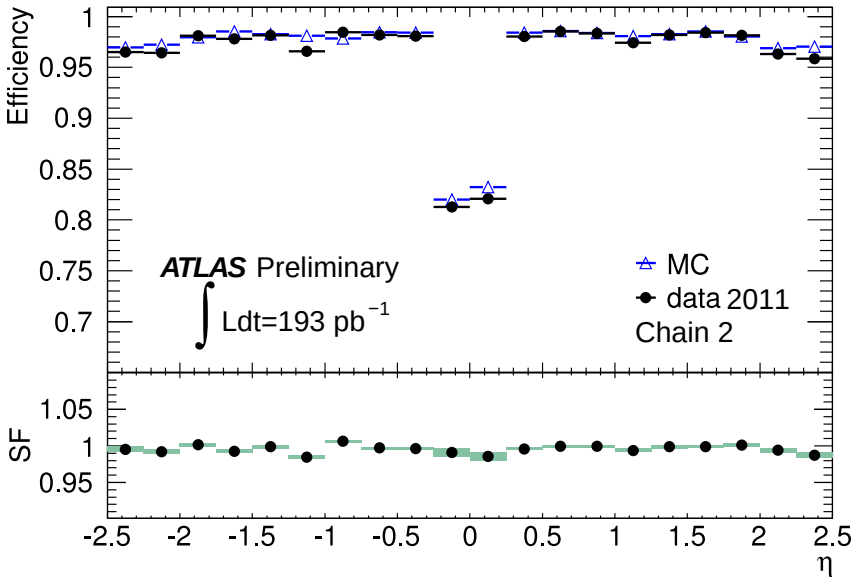

Figure 5.2: Combined muon reconstruction efficiency with respect to the inner tracking efficiency as a function of the pseudorapidity of the muon for muons with $p_T > 20$ GeV. The panel at the bottom shows the ratio between the measured and predicted efficiencies (SFs).

5.1.3.2 Inner detector efficiency

From the analyzed data set, MS-probes are selected to measure the reconstruction efficiency of the inner detector track selection.

To determine the ID reconstruction efficiency, the number of probes which can be matched to a inner detector track, with the same p_T, η selection as applied for the Z/γ^* analysis, has been counted. A probe is considered to

match a ID track if it is found within $\Delta R < 0.01$.

The overall efficiencies measured from data and compared with the expected efficiencies from the $Z/\gamma^* \rightarrow \mu\mu$ Monte Carlo simulation are summarized in table 5.3.

ID Reconstruction Efficiency and SF		
Data	MC	SF
0.9967 ± 0.0005	0.9963 ± 0.0000	1.0004 ± 0.0005

Table 5.3: Summary of the tag-and-probe ID reconstruction efficiencies. The background subtracted data measurement is compared to the Monte Carlo expectations and the relative SF is derived. Only statistic uncertainties are reported.

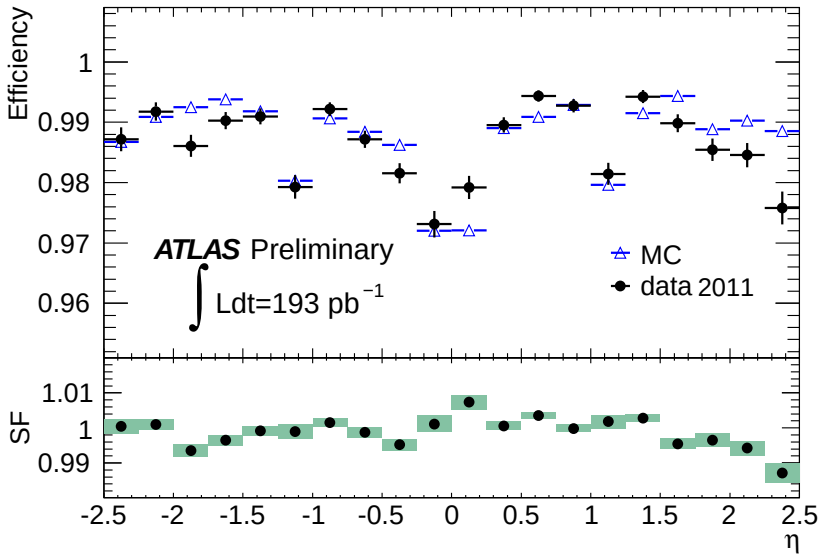

Figure 5.3: Measured inner detector muon reconstruction efficiency for two sets of hit requirements for muons with $p_T > 20$ GeV as a function of the pseudorapidity of the muon. The efficiency dips at $\eta \sim 0$ and $|\eta| \sim 1.2$ are caused by hit requirements imposed on the reconstructed muon.

5.2 Muon Momentum Resolution

The muon momentum resolution depends on several factors: the intrinsic resolution on the single hit in each sub-detector, the detector misalignment, the multiple scattering of the muon going through the detector. In the Monte Carlo simulation these effects are modeled with *a priori* constants and therefore the muon momentum resolution can be different between data and Monte Carlo simulation. For this reason the muon transverse momentum reconstructed in Monte Carlo simulation is corrected (smeared), leading to improved agreement with the shapes measured in data. Fig. 5.4 shows how the correction improves the data/MC agreement.

The procedure adopted to smear the muon p_{T} implies the introduction of correction terms for the p_{T} measurement performed both in the Inner Detector (ID) and in the Muon Spectrometer (MS). The measurements of these various terms for the MS and ID are obtained using a fitting technique with Monte Carlo templates. The templates are varied to find the best match with the distributions obtained from data, as explained in [56]. The distributions used are both the di-muon invariant mass in $Z/\gamma^{*}\rightarrow\ \mu\mu$ events and the MS-to-ID curvature difference weighted by the electric charge ($\frac{Q}{p_T^{ID}} - \frac{Q}{p_T^{MS}}$). For the smearing procedure the detector is divided in four η regions for which different resolutions are expected both in data and Monte Carlo because of the different sub-detectors used.

The weighting by the charge disentangles systematic effects of the curvature due to local misalignments from the overall intrinsic resolution. The η regions in which the corrections are computed are:

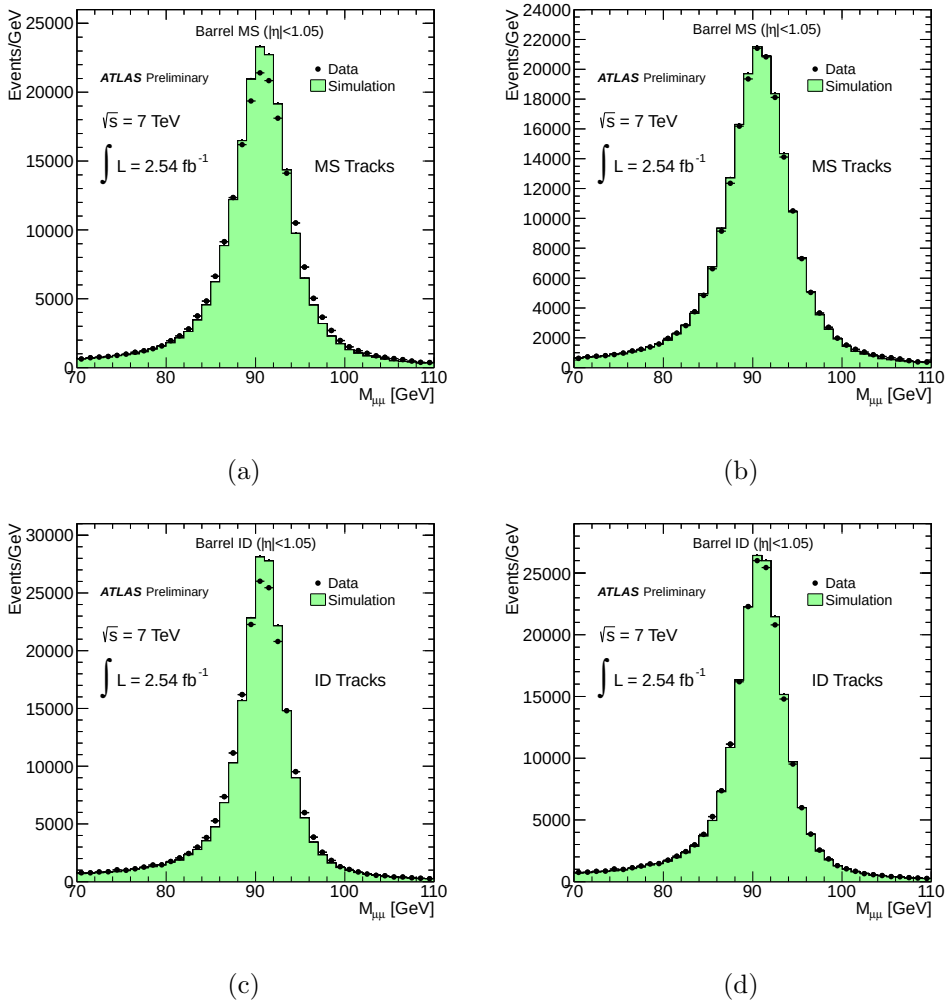

Figure 5.4: Di-muon invariant mass for muon spectrometer (a, b) and inner detector (c, d) muon tracks with $p_T > 15$ GeV in the barrel region ($|\eta| < 1.05$), before (a, c) and after (b, d) the smearing procedure.

- barrel: $0 < |\eta| < 1.05$
- transition region: $1.05 < |\eta| < 1.7$
- end-caps: $1.7 < |\eta| < 2.0$
- CSC/no TRT: $2.0 < |\eta| < 2.5$

The correction terms introduced to smear the muon transverse momentum (see eq. 5.2.1 and 5.2.2) are aimed at computing additional contribution to the multiple scattering and to the intrinsic resolution of the sub-detectors, while the alignment constants are measured directly from data using special runs in which the data are taken without the magnetic field.

$$p'_T(MS) = p_T(MS) \times (1 + \Delta(MS)) \tag{5.2.1}$$

where

$$\Delta(MS) = f(0,1) \times \Delta p_1^{MS} + f(0,1) \times \Delta p_2^{MS} \times p_T$$

$$p'_T(ID) = p_T(ID) \times (1 + \Delta(ID)) \tag{5.2.2}$$

where

$$\Delta(ID) = g(0,1) \times \Delta p_1^{ID} + g(0,1) \times \Delta p_2^{ID} \times p_T \quad (|\eta| < 1.9)$$

$$\Delta(ID) = h(0,1) \times \Delta p_1^{ID} + h(0,1) \times \Delta p_2^{ID} \times p_T / \tan^2(\theta) \quad (|\eta| > 1.9)$$

In the previous equations $f(0,1)$, $g(0,1)$ and $h(0,1)$ are normally distributed random numbers, the $p'_T(ID)$ and $p'_T(MS)$ variables represent the Monte Carlo

η region	MS $\Delta p_1^{MS}(\%)$	MS $\Delta p_2^{MS}(TeV^{-1})$	ID $\Delta p_1^{ID}(\%)$	ID $\Delta p_2^{ID}(TeV^{-1})$
barrel	1.95 ± 0.04	0.10 ± 0.02	0	0.19 ± 0.01
transition	$3.97 \pm 0.06 \pm 0.12$	$0.47 \pm 0.02 \pm 0.08$	0	$0.24 \pm 0.03 \pm 0.03$
MDT end-cap	2.88 ± 0.14	0.20 ± 0.01	0	0.50 ± 0.02
CSC/no TRT	1.82 ± 0.02	0.15 ± 0.05	0	0.02 ± 0.01

Table 5.4: Values of the parameters used to smear the p_{T} in the different η regions.

p_T after the smearing correction; while Δp_1^i and Δp_2^i represent the correction due to multiple scattering and intrinsic resolution respectively in the sub-detector i. The $1/\tan^2(\theta)$ term is use to represent the worsening of the p_T measurement as a function of θ in the ID due to the edge of the TRT. The results obtained for these values are shown in table 5.4. There the first associated uncertainty is statistical and the second systematic.

Chapter 6

A_{fb} Measurement

The measurement of the forward-backward asymmetry, more challenging at the LHC with respect to Tevatron [10], requires the knowledge of the direction of the emitted muon relative to the incoming quark. This direction is measured using a particular reference frame, already described in Sec. 1.2.3, in order to minimize the effect due to the lack of knowledge of the incoming quark transverse momentum. With this change of coordinates the sensible quantity is the $\cos\theta^*$.

Looking back to Eq. 1.2.28 it is also clear that A_{fb} depends on the center-of-mass energy s and it is thus measured as a function of the di-muon invariant mass, $m_{\mu\mu}$.

The choice of the number of invariant-mass bins and their width has been dictated by the distribution of the number of events along the invariant-mass spectrum: where the number of events is relevant (that is around the Z pole) a finer binning has been adopted. The invariant-mass range from 60 to 1000 GeV has been divided into 21 bins. The lower and upper edges of each bin are

the following: 60, 66, 70, 76, 80, 86, 88, 89, 90, 91, 92, 93, 94, 95, 100, 105, 110, 116, 125, 250, 500, 1000 GeV.

Another important aspect of this measurement concerns the corrections that have to be applied to the measured A_{fb} distribution. This quantity is indeed measured as a *reconstructed* quantity, meaning that its value is measured with a finite detector resolution and, in principle, could not correspond to its *true* physical value.

Moreover, other effects influence the shape of the reconstructed A_{fb} distribution: the emission of photons in the final state (Final State Radiation, FSR) can change the reconstructed p_T of the muons, resulting in a bad reconstruction of the Z/γ^* invariant mass and asymmetry.

Finally, the lack of knowledge of the incoming quark direction can lead to a bad identification of a forward(backward) event as a backward(forward) one, resulting in a *dilution* of the asymmetry.

The combined contributions of these effects modify the *true* A_{fb} spectrum resulting in the measured, *raw*, A_{fb} distribution, that have to be corrected to get back to the physical, *true*, distribution.

Therefore, in summary, three main effects are taken into account: radiative corrections, detector resolution and dilution.

The A_{fb} measurement is corrected for these effects by means of a Monte Carlo response-matrix based unfolding. The RooUnfold toolkit [57] is used to perform the unfolding using an iterative Bayesian method [58].

6.1 Radiative and Detector Resolution Corrections

The effect of radiative corrections [60] is mainly to deform the shape of the Z/γ^* mass spectrum. This deformation is particularly pronounced below the Z peak and is thus expected to have an impact on any other observable in this region. Specifically, for what concerns the A_{fb} measurement, QED corrections move events away from the Z peak (i.e. A_{fb} positive and small) towards smaller values of invariant mass, hence reducing significantly the magnitude of the observed A_{fb} in the region 60 $GeV < m_{\mu\mu} <$ 90 GeV. In the high-mass region ($m_{\mu\mu} >$ 90 GeV) the reduction due to radiative corrections is still present, though reduced in magnitude.

Using the available $Z/\gamma^* \rightarrow \mu\mu$ Monte Carlo samples (cfr. Tab. 4.2), the probability is calculated that a forward(backward) event within a given bin of *reconstructed* $m_{\mu\mu}$ belongs to any bin of *true* $m_{\mu\mu}$. The resulting response matrices are shown in Fig. 6.1.

In this approach, the unfolding is also correcting for detector resolution, hence bringing the measurement back to the one at Born level. In the following, the cumulative correction for QED and detector resolution will be referred to as mass bin migration correction.

6.2 Dilution Correction

The second main effect to be accounted for is the A_{fb} dilution, as already discussed in Sec. 1.2.4. As shown in Fig. 6.2, a matrix of the probabilities that

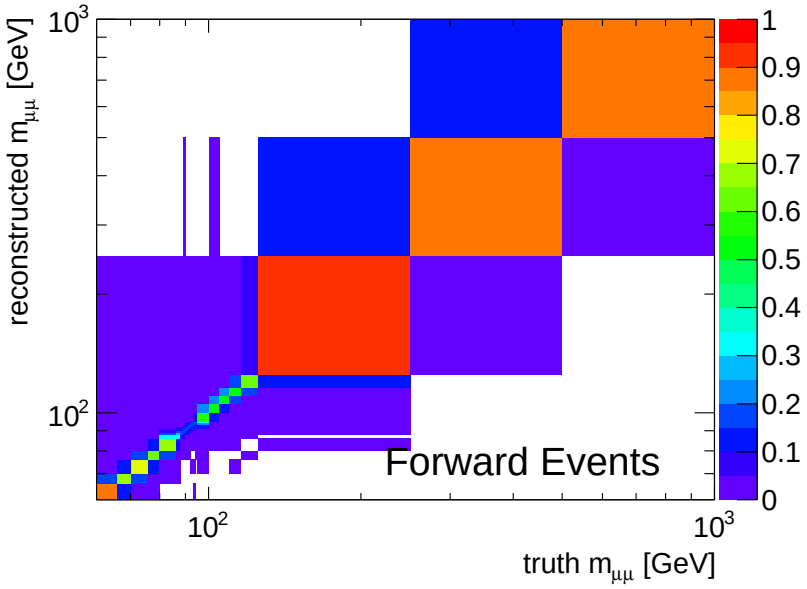

(a)

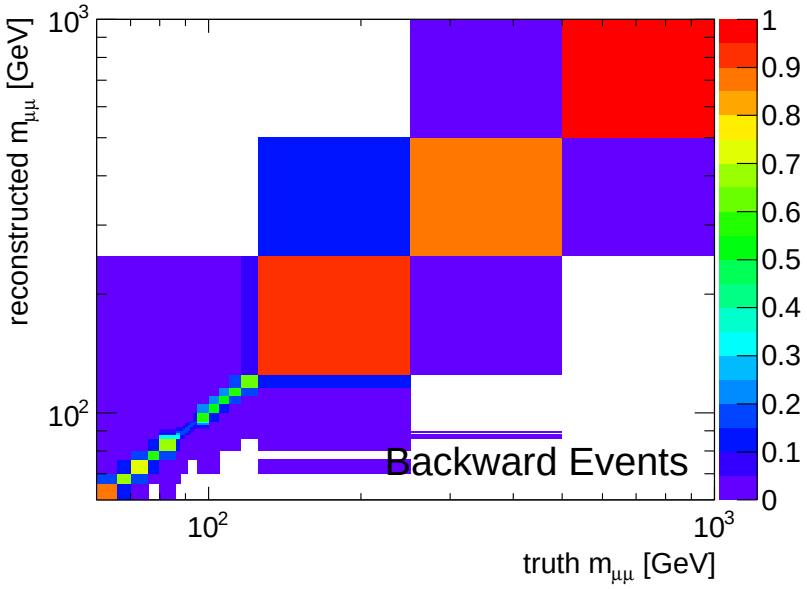

(b)

Figure 6.1: Response matrices to account for mass migration effect for forward (a) and backward (b) events.

an event within a given bin of *reconstructed* $\cos\theta^*$ belongs to any bin of *true* $\cos\theta^*$ has been calculated for each $m_{\mu\mu}$ bin. A similar approach as in the mass bin migration correction is then followed, using a Bayesian iterative method through the RooUnfold toolkit to obtain the *unfolded* distribution.

6.3 Raw A_{fb} Measurement

In order to measure the forward-backward asymmetry, I compute the value of $\cos\theta^*$ for each selected $Z/\gamma*$ event in the collision data sample using Eq. 1.2.34. The resulting distribution is then compared with the one obtained using selected events from Monte Carlo signal and background, as Fig. 6.3 shows for events within the 66-116 GeV mass range. A good agreement between the distributions is observed.

A measurement of the forward-backward asymmetry can now be performed following the steps below:

- divide the mass spectrum in bins as listed above;
- count in each bin the number of forward ($\cos\theta^* > 0$, N_F) and backward ($\cos\theta^* < 0$, N_B) events;
- subtract the number of forward and backward events due to the background;
- compute the A_{fb} value using the relation:

$$A_{fb} = \frac{N_F - N_B}{N_F + N_B} \tag{6.3.1}$$

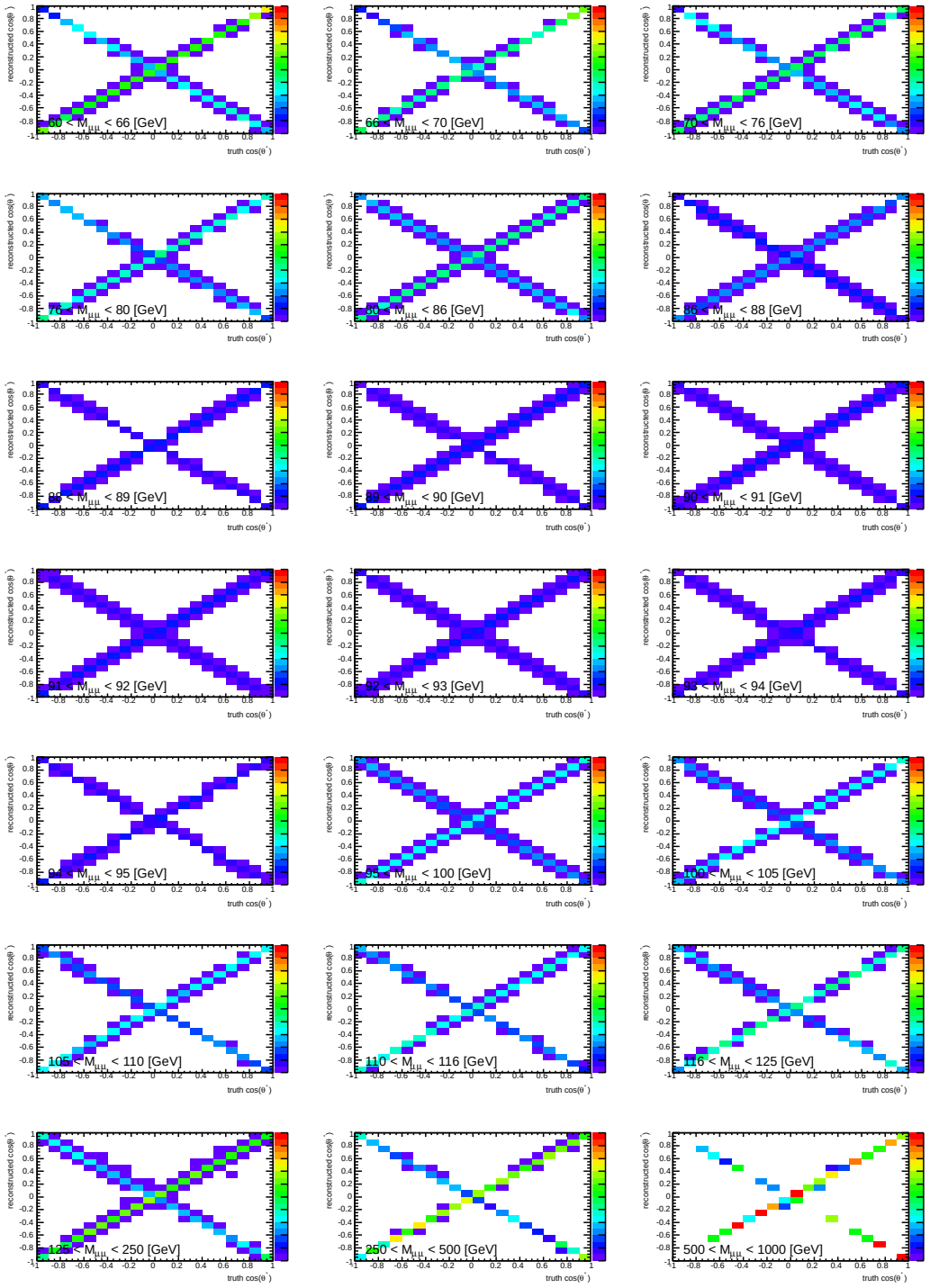

Figure 6.2: Response matrices to account for dilution effect. The color scale is the same as in Fig. 6.1.

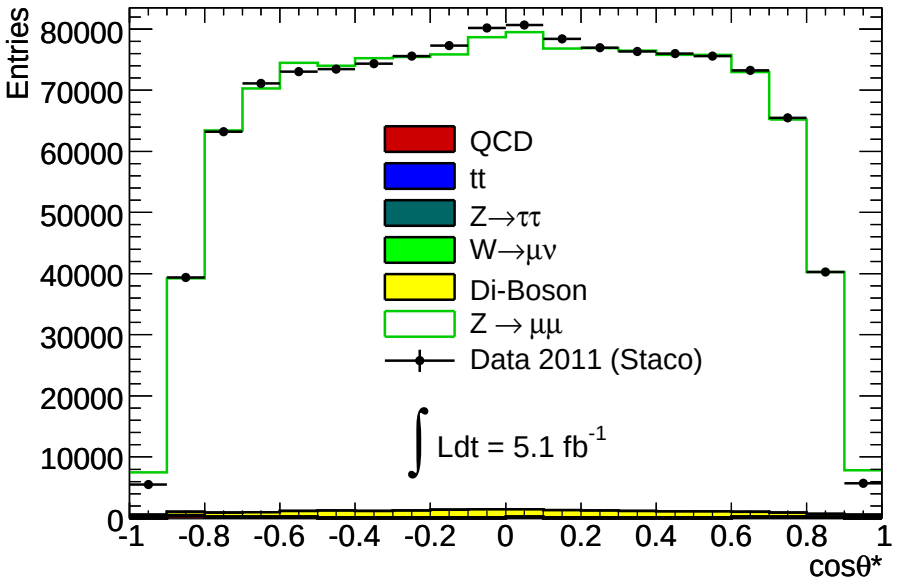

Figure 6.3: Comparison between data and Monte Carlo distribution of $\cos\theta^*$.

Fig. 6.4 shows the resulting *raw* A_{fb} distribution from data, compared with the one obtained from Monte Carlo.

This distribution is then corrected for the effects described in Sec. 6.1 and Sec. 6.2 and the resulting A_{fb} mass spectrum is described in Sec. 6.5.

6.4 Monte Carlo Closure Tests

Before applying the corrections listed in the previous sections on real data, the same techniques have been used to correct the Monte Carlo simulation. The *unfolded* PYTHIA A_{fb} has been compared with the *true* PYTHIA A_{fb} distribution to make sure that the results of the unfolding agree with the original A_{fb} distribution.

In a first test, the Monte Carlo samples described in Sec. 4.1.3 have been

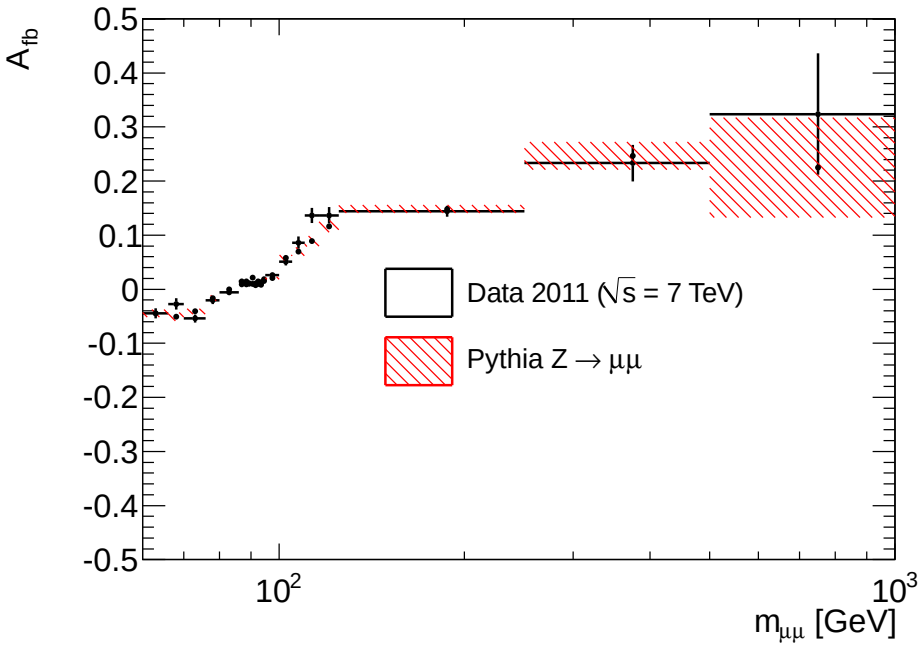

Figure 6.4: *Raw* A_{fb} as a function of di-muon invariant mass. Points with errors refer to data after background subtraction, red boxes refer to MC signal.

used to derive the reconstructed, simulated *raw* A_{fb} spectrum. The same samples were used to derive all response matrices and the unfolding was performed. Results are shown in Fig. 6.5 and Fig. 6.6. As expected, the corrected distributions are in agreement with the *true* Monte Carlo ones.

Since the events to be corrected are the same used to derive the response matrices, this is indeed just a validation of the unfolding method, which ensures the internal consistency of the analysis setup.

Another way to see the agreement between *true* and *unfolded* quantities is to look at the $\cos\theta^*$ distributions, as shown in Fig. 6.7.

A more informative test consists in splitting the available MC sample into two statistically independent subsamples and use the response matrices calcu-

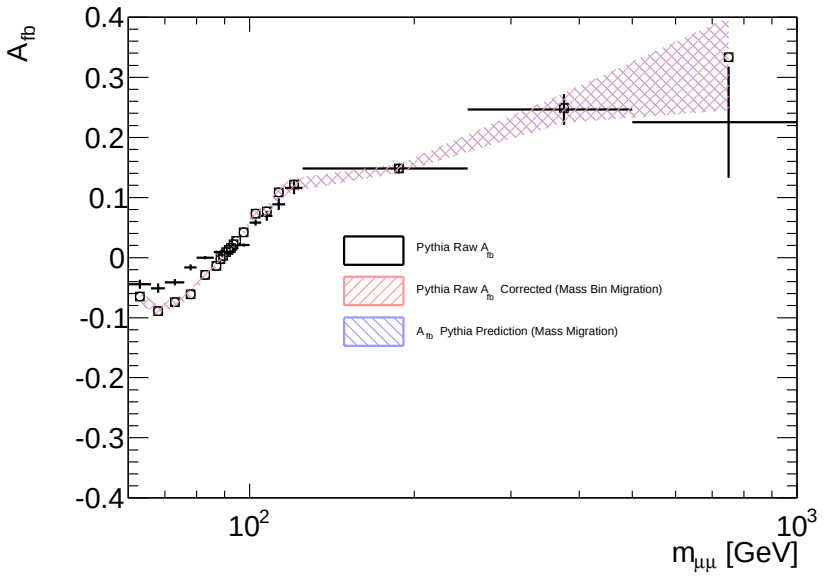

(a)

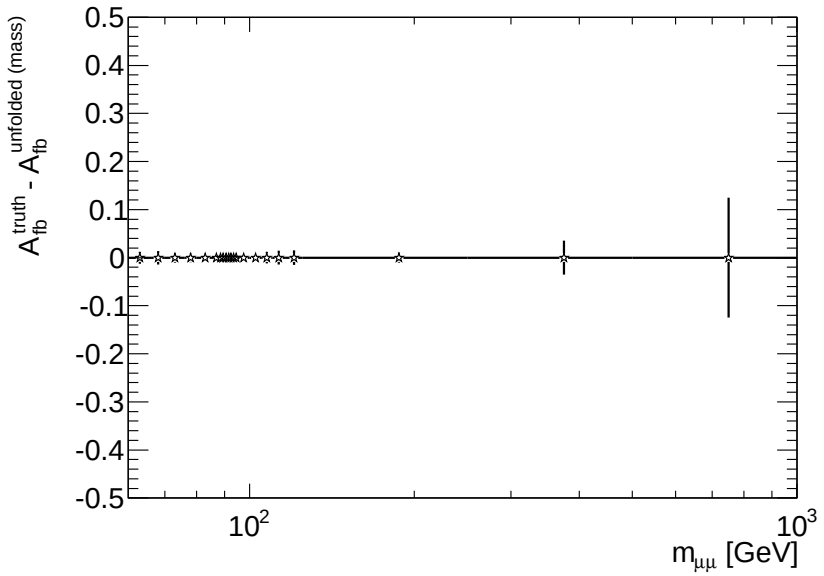

(b)

Figure 6.5: Comparison between PYTHIA *true* and *raw* A_{fb} corrected for mass bin migration (a). Plot in (b) shows the difference between the two.

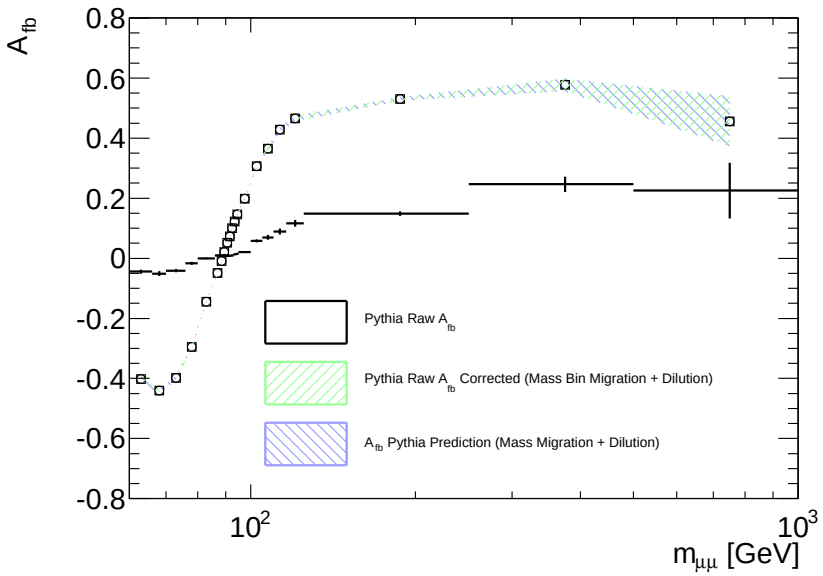

(a)

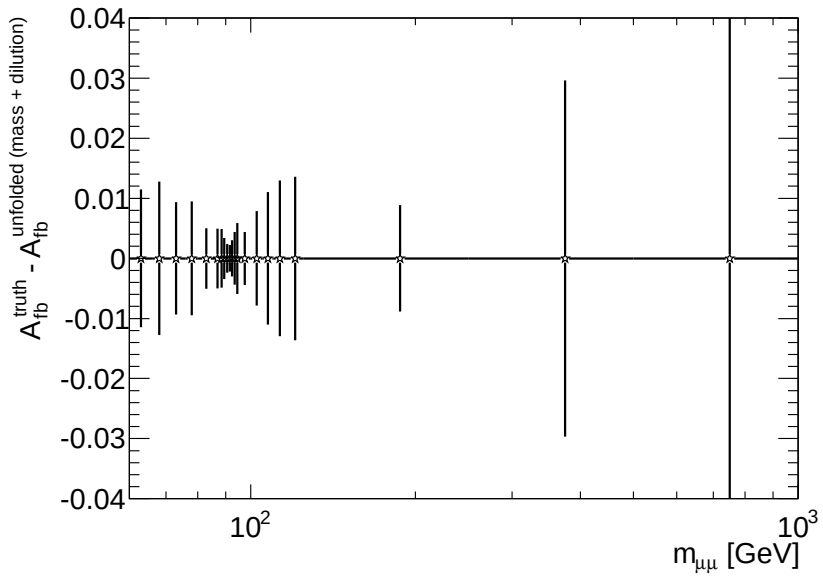

(b)

Figure 6.6: Comparison between PYTHIA *true* and *raw* A_{fb} corrected for mass bin migration and dilution (a). Plot in (b) shows the difference between the two.

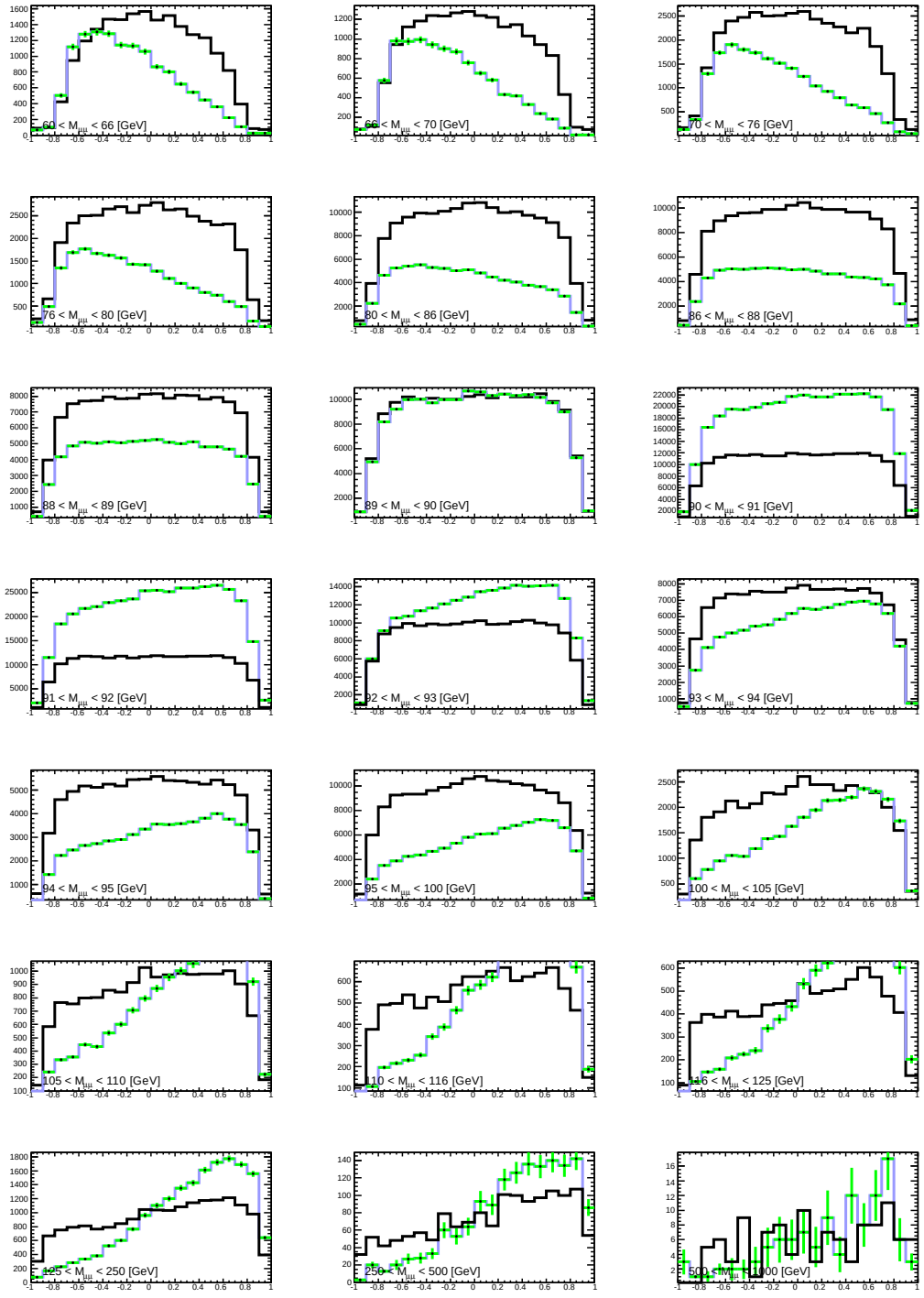

Figure 6.7: Monte Carlo $\cos\theta^*$ distribution for each di-muon invariant mass bin. The *raw* (black), corrected (green) and *true* (blu) A_{fb} distributions are shown.

lated from one of them to correct the A_{fb} spectrum measured from the other one. The results are shown in Fig. 6.8 for the PYTHIA A_{fb} spectrum corrected for mass bin migration and in Fig. 6.9, when also dilution is accounted for. In both cases the *true* PYTHIA prediction is shown as well.

6.5 Correcting the Data

After having validated the unfolding techniques described in Sec. 6.4, the data distribution has been corrected for both mass bin migration and dilution effects. The resulting distribution is shown in Fig. 6.10.

Fig. 6.11 shows the $\cos\theta^*$ distribution for each mass bin before and after all corrections are applied. For reference, the PYTHIA predicted distributions are also shown.

6.5.1 Propagation of the Statistical Error

Propagation of the statistical error on the *raw* spectrum through the unfolding procedure is not straightforward, due to the iterative nature of the method.

For this analysis, an approach based on pseudo-experiments was chosen. The input to the unfolding algorithm (i.e. the *raw* A_{fb}) is randomly fluctuated around its mean value, thus producing pseudo-experiments. Each of the pseudo-experiments is then used to produce an *unfolded* A_{fb} spectrum. The distribution of the A_{fb} obtained from pseudo-experiments is shown in Fig. 6.12.

As expected, the pseudo-experiments peak around the reference value. A Gaussian fit to these distributions yields a standard deviation per mass bin, which is used as statistical error on the *unfolded* A_{fb} value.

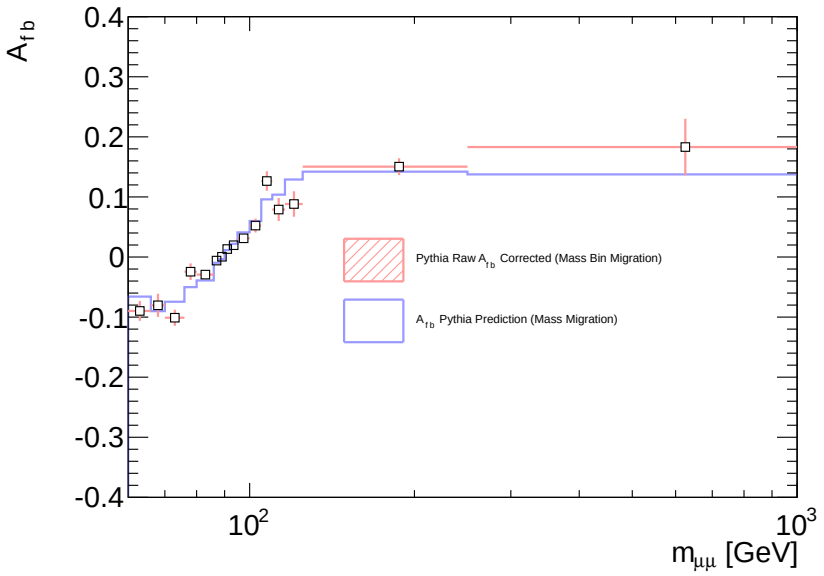

(a)

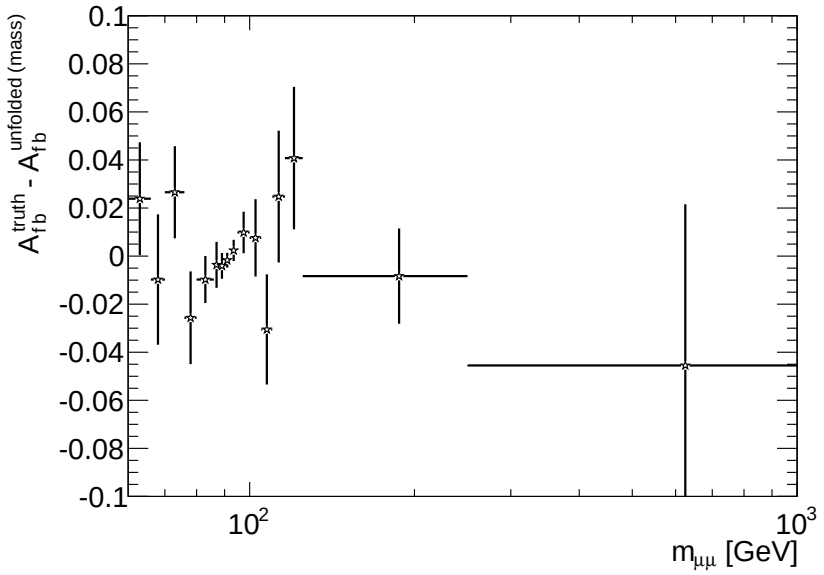

(b)

Figure 6.8: PYTHIA A_{fb} spectrum after mass bin migration correction, compared to the *true* PYTHIA prediction, for a statistically independent sample with respect the one used to derive the response matrices (a). In (b) the difference between the two is shown.

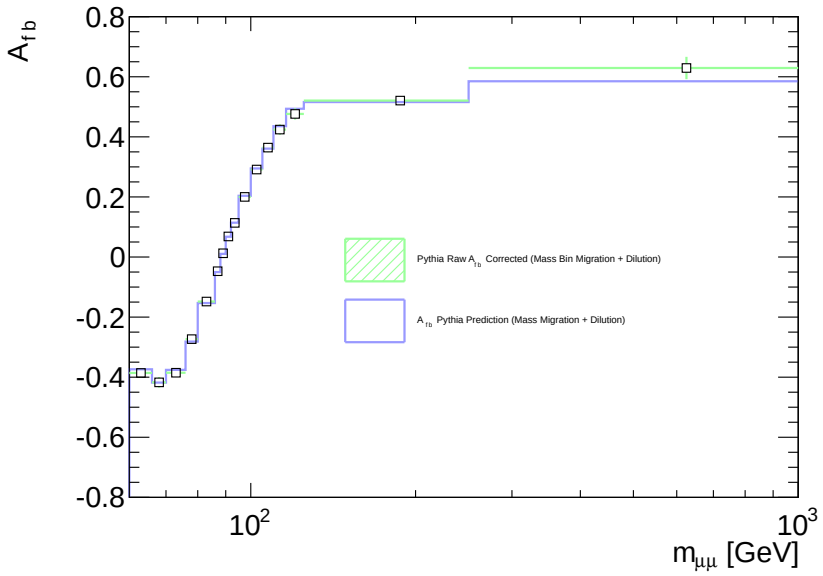

(a)

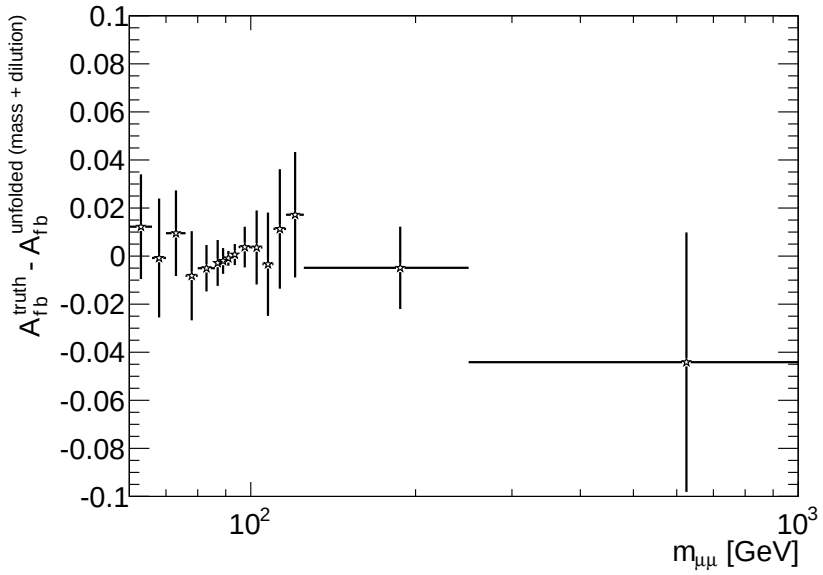

(b)

Figure 6.9: PYTHIA A_{fb} spectrum after mass bin migration and dilution corrections, compared to the *true* PYTHIA prediction, for a statistically independent sample with respect the one used to derive the response matrices (a). In (b) the difference between the two is shown.

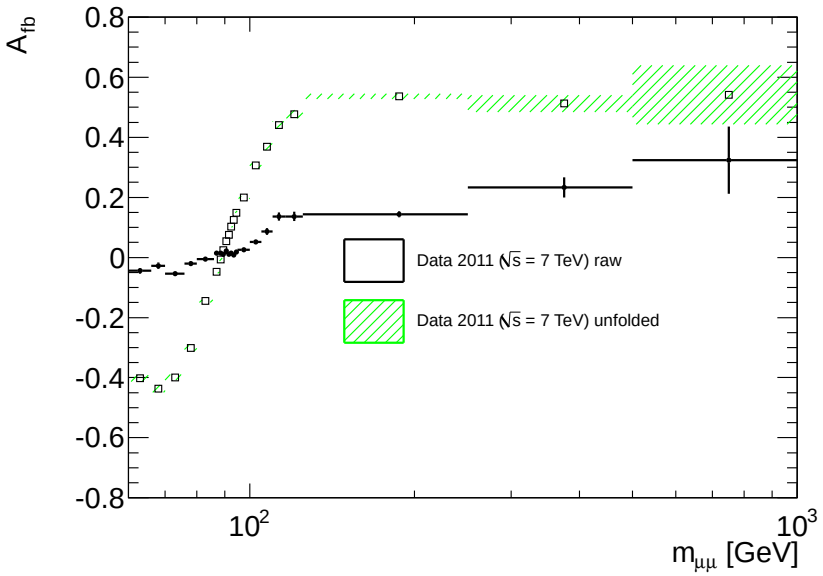

Figure 6.10: *Raw* and *unfolded* A_{fb} as a function of di-muon invariant mass.

The third column of Tab. 6.1 summarizes the standard deviation values obtained from the fit, for each mass bin.

6.6 Systematic Uncertainties

The systematic uncertainty on the asymmetry spectrum described above receives contributions from different sources:

- one specific algorithm was chosen for the unfolding. A different algorithm would have given a different *unfolded* distribution;

- the unfolding is completely MC-based and some specific MC samples were used. Different MC samples (e.g with different generator or PDFs) could in principle lead to a different *unfolded* spectrum;

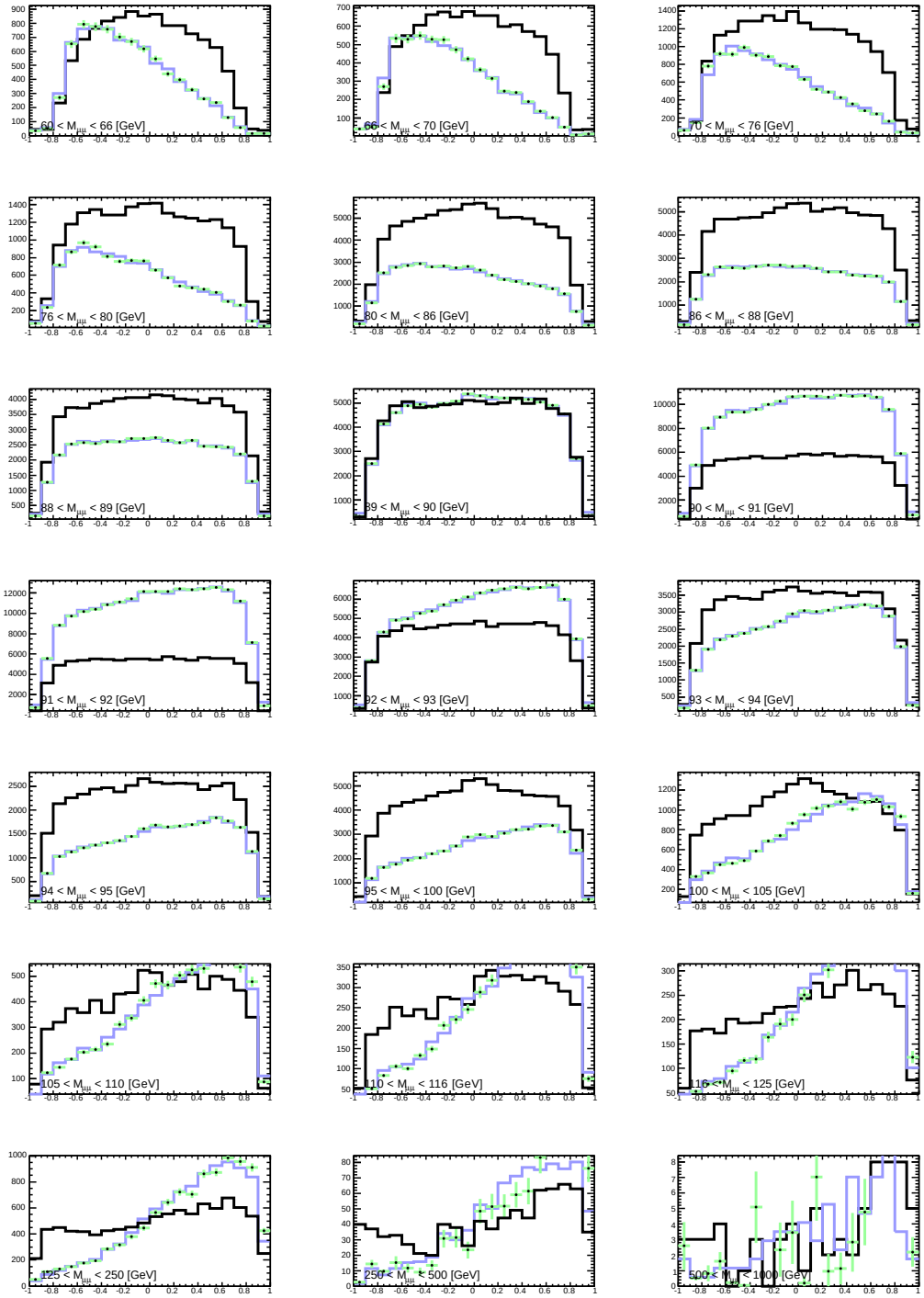

Figure 6.11: Data $\cos\theta^*$ distribution for each di-muon invariant mass bin. The *raw* (black), corrected (green) and *true* predicted (blu) A_{fb} distributions are shown.

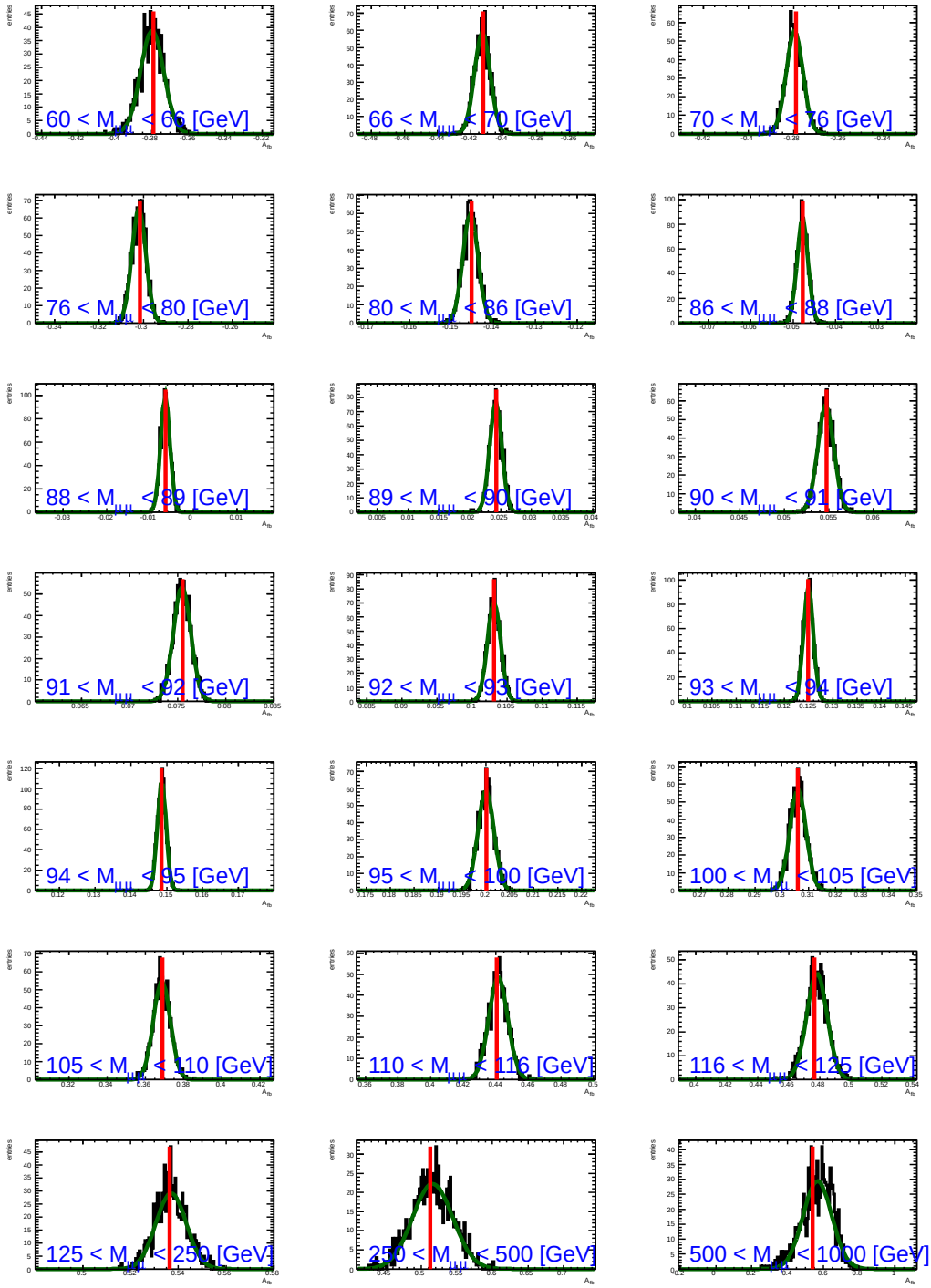

Figure 6.12: A_{fb} distribution obtained with pseudo-experiments fluctuating the *raw* A_{fb} measurements. The red line is the value obtained from the non fluctuated (reference) spectrum. A Gaussian fit is superimposed to the distributions.

Mass Bin $m_{\mu\mu}$[GeV]	A_{fb}	σ_{DATA}	σ_{MC}	$\sigma_{MC+DATA}$
60 - 66	-0.4023	0.0063	0.0079	0.0102
66 - 70	-0.4366	0.0047	0.0095	0.0093
70 - 76	-0.3989	0.0037	0.0070	0.0077
76 - 80	-0.3017	0.0032	0.0071	0.0075
80 - 86	-0.1452	0.0018	0.0038	0.0039
86 - 88	-0.0477	0.0013	0.0036	0.0037
88 - 89	-0.0064	0.0011	0.0036	0.0035
89 - 90	0.0243	0.0010	0.0025	0.0022
90 - 91	0.0547	0.0009	0.0016	0.0018
91 - 92	0.0755	0.0009	0.0016	0.0019
92 - 93	0.1032	0.0009	0.0021	0.0027
93 - 94	0.1249	0.0010	0.0030	0.0033
94 - 95	0.1486	0.0012	0.0041	0.0042
95 - 100	0.2001	0.0017	0.0031	0.0035
100 - 105	0.3060	0.0030	0.0055	0.0066
105 - 110	0.3688	0.0045	0.0084	0.0088
110 - 116	0.4407	0.0059	0.0089	0.0103
116 - 125	0.4766	0.0066	0.0099	0.0103
125 - 250	0.5363	0.0064	0.0072	0.0088
250 - 500	0.5125	0.0282	0.0282	0.0351
500 - 1000	0.5416	0.0803	0.0935	0.1260

Table 6.1: Summary of the A_{fb} *unfolded* values for each mass bin. Results obtained with pseudo-experiments are shown: σ_{DATA} represents the error obtained by fluctuating the *raw* A_{fb} spectrum; σ_{MC} is the result from fluctuating the response matrices; $\sigma_{MC+DATA}$ represents the one obtained when fluctuating both response matrices and *raw* A_{fb}.

- once the MC samples are chosen, they only provide a limited number of events, i.e. the statistical error on the response matrices used for unfolding propagates (as a systematic) to the error on the *unfolded* spectrum.

This section describes the methods used to assess the impact of each of these effects.

6.6.1 Comparison of Different Unfolding Algorithms

As already mentioned (cfr. Sec. 6.1) the RooUnfold toolkit has been used to perform the unfolding of the asymmetry spectrum in this analysis. One of its advantages is that it allows a straightforward comparison between different algorithms (cfr. App. A). Such a comparison has indeed been carried on and the results are shown in Tab. 6.2 and graphically in Fig. 6.13.

Mass Bin	A_{fb}			Error
$m_{\mu\mu}$[GeV]	Bayes	BinByBin	SVD	
60 - 66	-0.4023	-0.4018	-0.4120	0.0146
66 - 70	-0.4366	-0.4213	-0.4195	0.0093
70 - 76	-0.3989	-0.4095	-0.4110	0.0087
76 - 80	-0.3017	-0.3066	-0.3111	0.0094
80 - 86	-0.1452	-0.1454	-0.1678	0.0225
86 - 88	-0.0477	-0.0464	-0.0465	0.0013
88 - 89	-0.0064	-0.0081	0.0102	0.0166
89 - 90	0.0243	0.0255	0.0275	0.0032
90 - 91	0.0547	0.0618	0.0666	0.0118
91 - 92	0.0755	0.0756	0.0968	0.0213
92 - 93	0.1032	0.1009	0.1053	0.0022
93 - 94	0.1249	0.1227	0.1269	0.0023
94 - 95	0.1486	0.1486	0.1557	0.0072
95 - 100	0.2001	0.2018	0.1970	0.0030
100 - 105	0.3060	0.3038	0.3043	0.0022
105 - 110	0.3688	0.3644	0.3628	0.0060
110 - 116	0.4407	0.4491	0.4466	0.0083
116 - 125	0.4766	0.4747	0.4874	0.0108
125 - 250	0.5363	0.5352	0.5463	0.0100
250 - 500	0.5125	0.5290	0.5656	0.0531
500 - 1000	0.5416	0.5324	0.4453	0.0963

Table 6.2: A_{fb} *unfolded* spectrum, using different unfolding algorithms, for each mass bin. The last column shows the uncertainty, derived as described in the text, used as systematic error on the measurement.

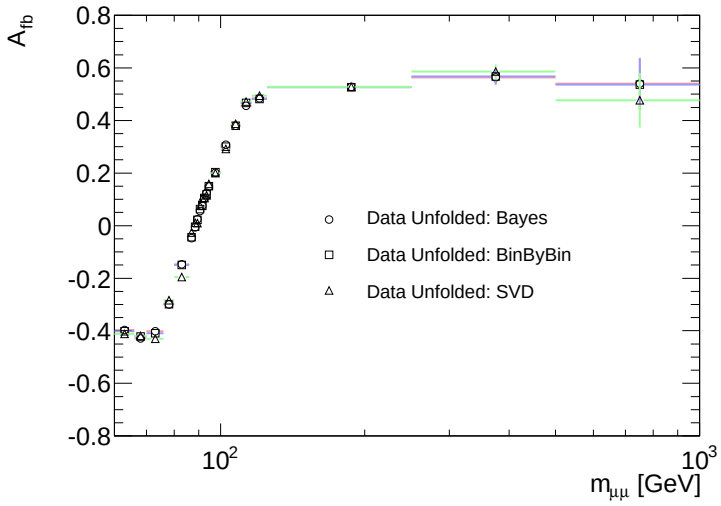

(a) Comparison of A_{fb} distribution with different unfolding algorithms

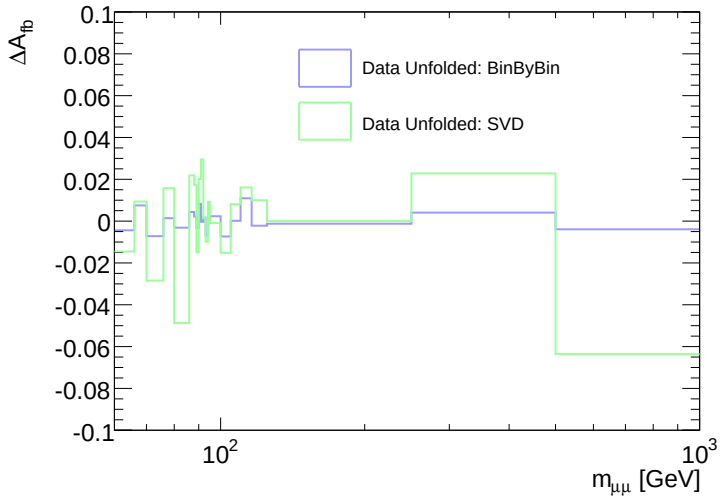

(b) Maximum difference between A_{fb} values obtained with different unfolding algorithms

Figure 6.13: A_{fb} corrected spectrum with different unfolding algorithms.

For each mass bin, I take as a reference value the one obtained from Bayesian unfolding. The maximum difference between any of the other algorithms and the reference is used as systematic error for that bin.

Fig. 6.14 shows the A_{fb} spectrum when only this systematic uncertainty is considered. The statistical error on the central value is obtained as described in Sec. 6.6.

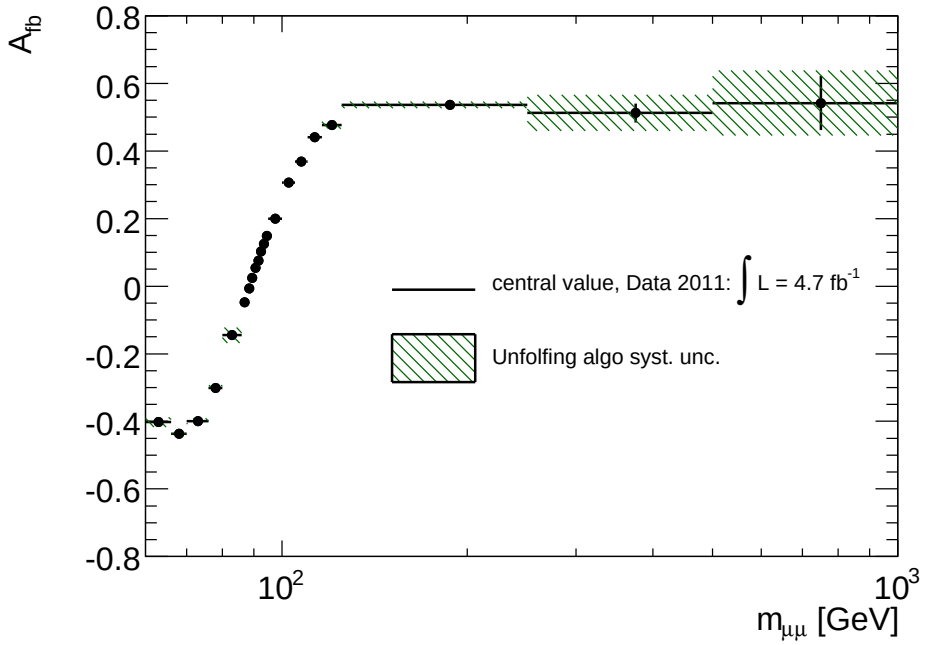

Figure 6.14: A_{fb} distribution with systematic uncertainty due to different unfolding algorithms.

6.6.2 Limited Statistic in Monte Carlo

This contribution to the systematic error is estimated in a way similar to what discussed in Sec. 6.5.1 for the statistical error. In this case, the response matrices used to perform the unfolding are fluctuated (while the input *raw* A_{fb} is not) and the resulting matrices are used to perform the unfolding. The resulting distributions of *unfolded* A_{fb} are shown in Fig. 6.15.

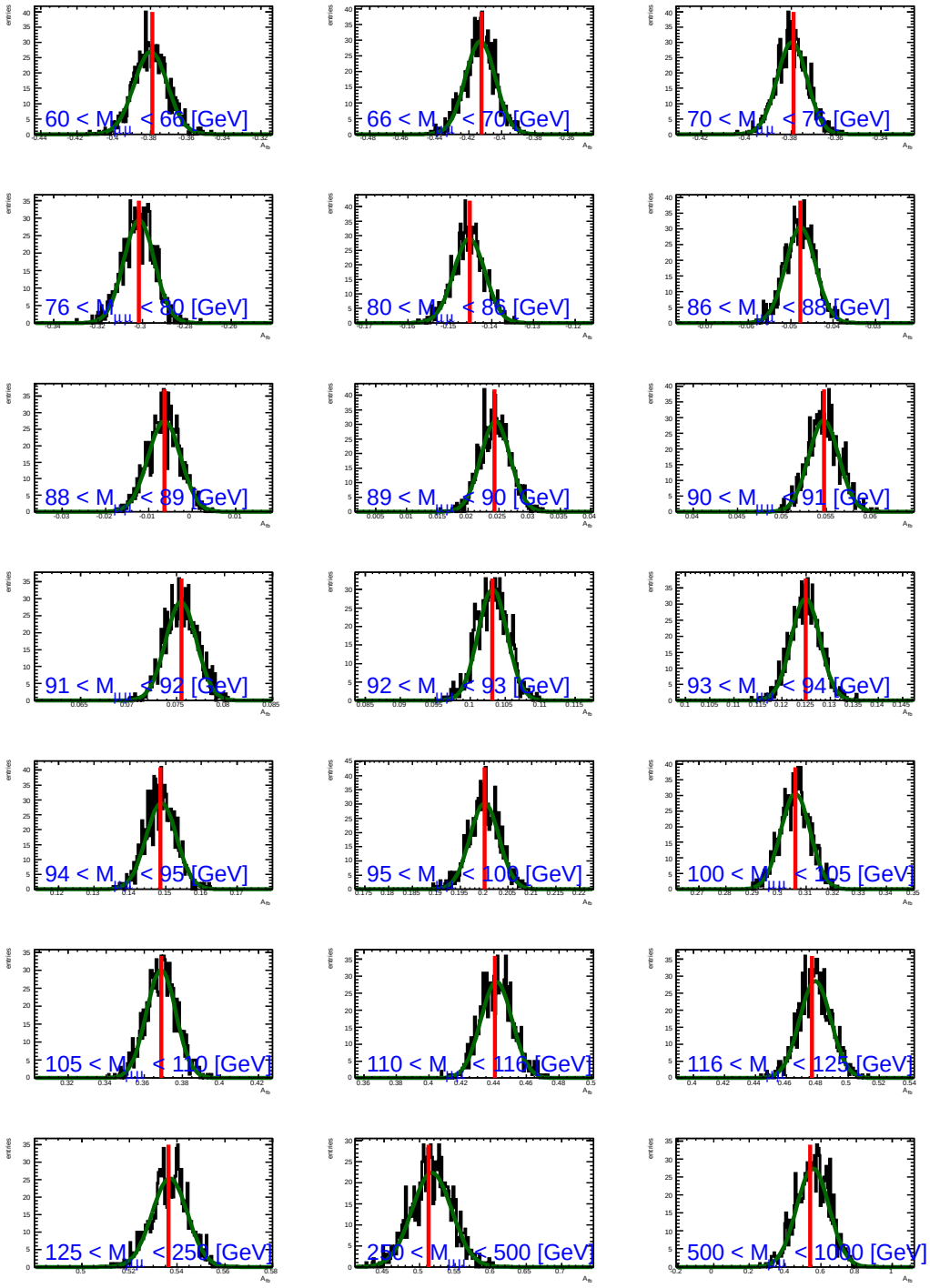

Figure 6.15: A_{fb} distribution obtained with pseudo-experiments fluctuating input matrix bin content according to a Poisson probability distribution.

As already discussed in 6.5.1, the standard deviation from a Gaussian fit to the *unfolded* A_{fb} distribution is taken as systematic error for each mass bin.

As a useful cross check and to validate this procedure against unexpected correlations, I also performed a test where both the response matrices ad the *raw* A_{fb} spectrum were fluctuated. As expected, the total standard deviation in this case is compatible with the sum in quadrature of the standard deviations obtained fluctuating separately the *raw* A_{fb} distribution and the response matrices. The distributions from this consistency check are shown in Fig. 6.16 and in Tab. 6.1.

Fig. 6.17 shows the A_{fb} spectrum when only the Monte Carlo statistic systematic uncertainty is considered. The statistical error on the central value is obtained as described in Sec. 6.6.

6.6.3 PDFs Uncertainties on A_{fb}

As discussed in Sec. 6.1 and Sec. 6.2, the corrections to A_{fb} are Monte Carlo based and thus the A_{fb} corrected (*unfolded*) value could be sensitive to the Parton Distribution Functions (PDFs) chosen to describe the probability density for finding a parton of flavor f with a certain longitudinal momentum fraction x at momentum transfer Q^2.

Because of the inherent non-perturbative effect in a QCD binding state, parton distribution functions cannot be obtained by perturbative QCD. Due to the limitations in present lattice QCD calculations, the known parton distribution functions are instead obtained using experimental data.

PDFs are essential inputs to make theoretical predictions at hadron collid-

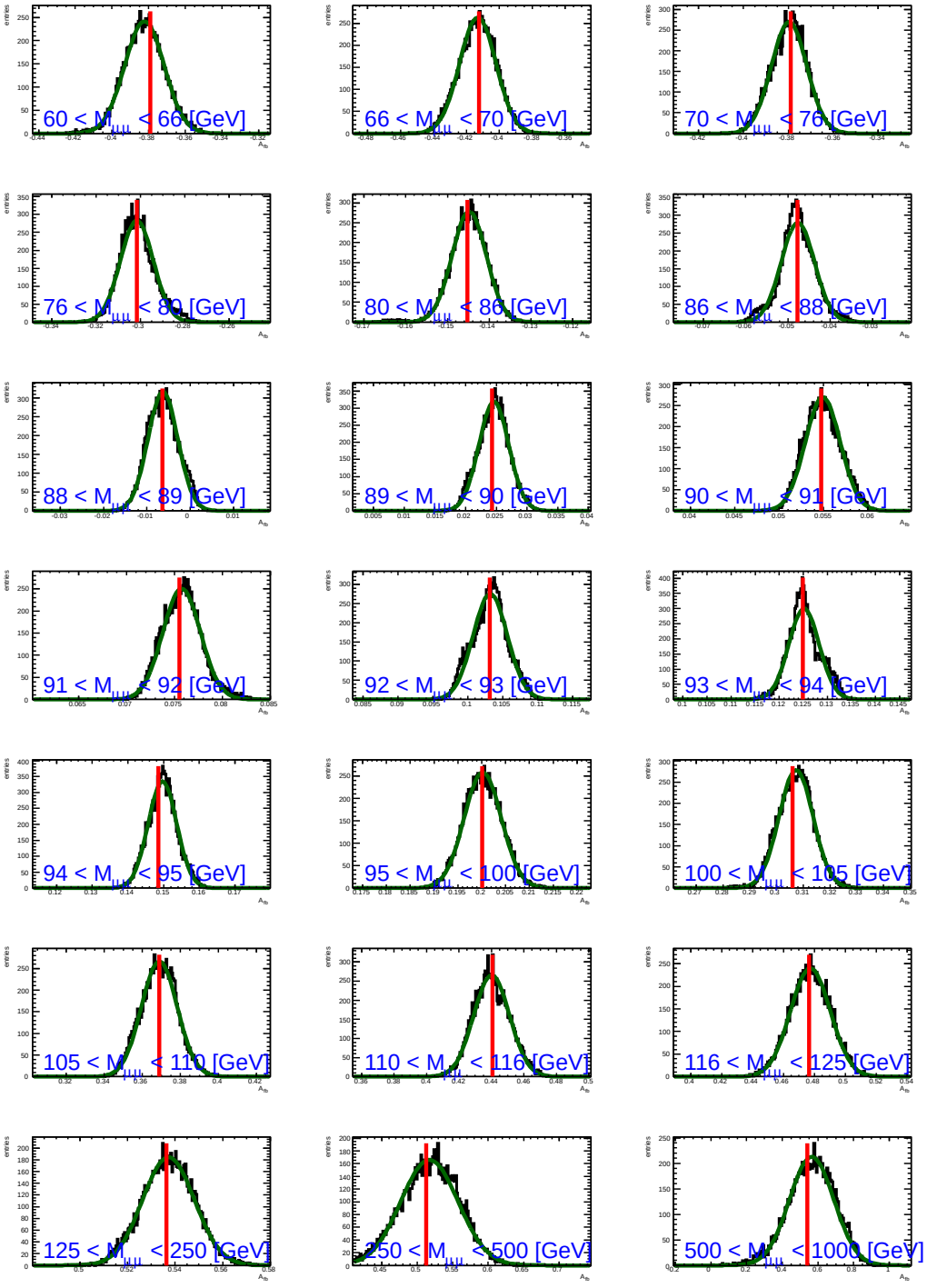

Figure 6.16: A_{fb} distribution obtained with pseudo-experiments fluctuating input matrix bin content and data histogram according to a Poisson probability distribution.

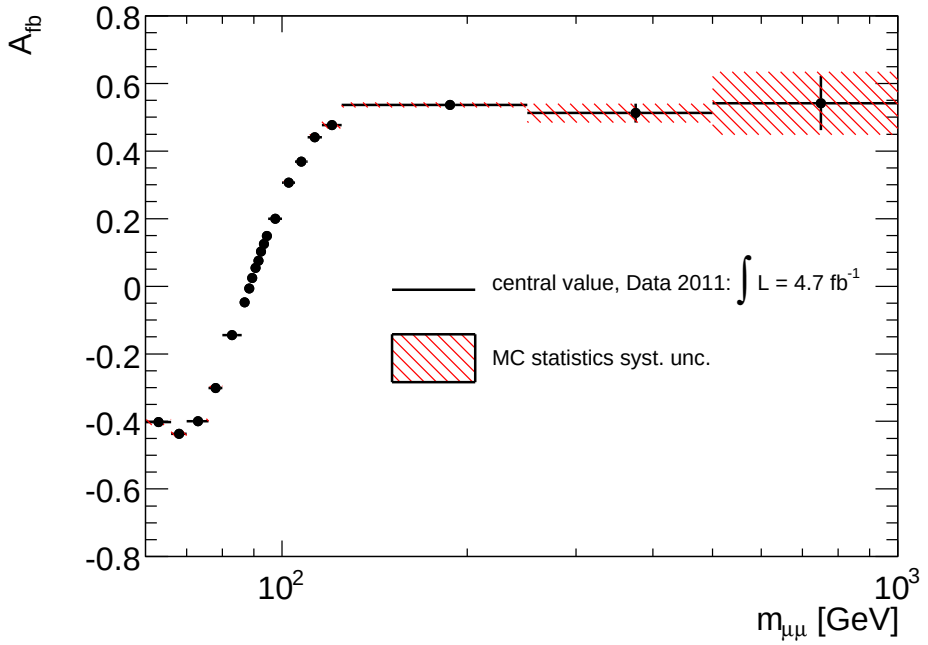

Figure 6.17: A_{fb} distribution with systematic error due to limited Monte Carlo statistic. The error bars represent the statistical error from data statistics, as obtained in section 6.5.1.

ers and experimentally determined Parton Distribution Functions are available from various groups worldwide. One of these groups is the CTEQ[1] [61] collaboration that provides information of best fit PDF and a set of error PDFs used to determine the uncertainty on any observable that depends on the PDFs.

In the Pythia sample used in the analysis, the MRSTMCal PDF was chosen. This PDF does not provide any error set, so the easiest way to obtain an error set is to reweight the actual sample according to the following prescription.

Suppose we generate Z/γ^* events with a particular PDF set: PDF set 1.

[1]CTEQ stands for *Coordinated Theoretical/Experimental project on QCD and phenomenology and tests of the Standard Model.*

Any event has the hard scale, $Q^2 = m_{Z/\gamma^*}$, and two primary partons of flavors f_1 and f_2, with momentum fractions x_1, x_2 according to the distributions of PDF set 1. These momentum fractions are applicable to the hard process before the parton showers are implemented in backward evolution in the MC. One can then evaluate the probability of picking up the same flavored partons with the same momentum fractions from an alternative PDF set, PDF set 2, at the same hard scale. Then the event weight is given by

$$w = \frac{f_{PDF_2}(x_1, f_1, Q^2) f_{PDF_2}(x_2, f_2, Q^2)}{f_{PDF_1}(x_1, f_1, Q^2) f_{PDF_1}(x_2, f_2, Q^2)} \tag{6.6.1}$$

where $f_{PDF_j}(x_i, f_i, Q^2)$, with $j = 1, 2$ and $i = 1, 2$, is the parton momentum distribution for flavor f_i, at scale Q^2, and momentum fraction x_i. In our case PDF 1 is MRSTMCal and PDF 2 is each of the 44 + 1 CTEQ6.6 NLO PDF error set. Each distribution relevant to the determination of the correction matrices is reweighed, event by event, and the resulting corrected A_{fb} is calculated.

The uncertainties on the A_{fb} have been estimated taking into account different contributions:

- the uncertainties within one PDF set. This was estimated using the 44 PDF error eigenvector sets (2 PDF sets for each of the 22 eigenvectors, along the ($\pm$) directions) of the CTEQ6.6 NLO PDF set, obtained from PDF reweighting of the sample generated using PYTHIA and the CTEQ6.6 NLO PDF set. The standard prescription has been used to calculate the error: for a given quantity X that depends on the PDFs,

the uncertainty is given by

$$\Delta X = \frac{1}{2}\sqrt{\sum_{i=1}^{N}\left(X_i^{(+)} - X_i^{(-)}\right)^2} \tag{6.6.2}$$

where the sum is over the number of 22 eigenvectors and $X_i^{(+)}$ and $X_i^{(-)}$ are the values of X computed from the two sets of PDFs along the $\pm$ direction of the i-th eigenvector;

- the differences between different PDFs sets. The uncertainty related to the choice of the PDF have been estimated as the maximum deviation between the A_{fb} evaluated using the MRSTMCal and the one calculated using CTEQ6.6 PDF set.

The results of this study are summarized in the Tab. 6.3, where the bin by bin A_{fb} values and the corresponding uncertainties arising from PDFs are reported.

Fig. 6.18 shows the *unfolded* asymmetry spectrum with statistical (error bars) and systematic error due to the CTEQ6.6 PDFs.

6.7 Measured A_{fb}

Fig. 6.19 shows the A_{fb} distribution after all corrections have been applied. It is also compared to the Monte Carlo physics-level expectation. The black band represents the sum in quadrature of all the systematic uncertainties discussed in the previous sections.

The PYTHIA predicted A_{fb}, with its related uncertainty and the fully cor-

Mass Bin m[GeV]	A_{fb} [MRSTMCal]	A_{fb} [CTEQ 6.6]	A_{fb}(CTEQ 6.6) - A_{fb}(LO**)	ΔA_{fb} [CTEQ 6.6 error set]
60 - 66	-0.4023	-0.3957	0.0067	0.0036
66 - 70	-0.4366	-0.4308	0.0057	0.0029
70 - 76	-0.3989	-0.3942	0.0047	0.0028
76 - 80	-0.3017	-0.2986	0.0030	0.0030
80 - 86	-0.1452	-0.1439	0.0014	0.0026
86 - 88	-0.0477	-0.0473	0.0005	0.0018
88 - 89	-0.0064	-0.0063	0.0001	0.0010
89 - 90	0.0243	0.0236	-0.0007	0.0010
90 - 91	0.0547	0.0539	-0.0008	0.0009
91 - 92	0.0755	0.0744	-0.0011	0.0009
92 - 93	0.1032	0.1013	-0.0019	0.0010
93 - 94	0.1249	0.1230	-0.0019	0.0011
94 - 95	0.1486	0.1459	-0.0026	0.0015
95 - 100	0.2001	0.1964	-0.0037	0.0019
100 - 105	0.3060	0.2990	-0.0070	0.0032
105 - 110	0.3688	0.3586	-0.0102	0.0045
110 - 116	0.4407	0.4304	-0.0103	0.0054
116 - 125	0.4766	0.4639	-0.0126	0.0061
125 - 250	0.5363	0.5195	-0.0168	0.0088
250 - 500	0.5125	0.4926	-0.0199	0.0153
500 - 1000	0.5416	0.5357	0.0058	0.0076

Table 6.3: Summary of the A_{fb} *unfolded* values, for each mass bin, obtained with PYTHIA Monte Carlo and two PDFs: MRSTMCal (LO**) and CTEQ 6.6 (NLO). The table reports also the maximum deviation between the A_{fb} evaluated using the MRSTMCal and the one calculated using CTEQ6.6 PDF set and in the last column the uncertainties within CTEQ6.6 PDF set calculated with the Eq. 6.6.2.

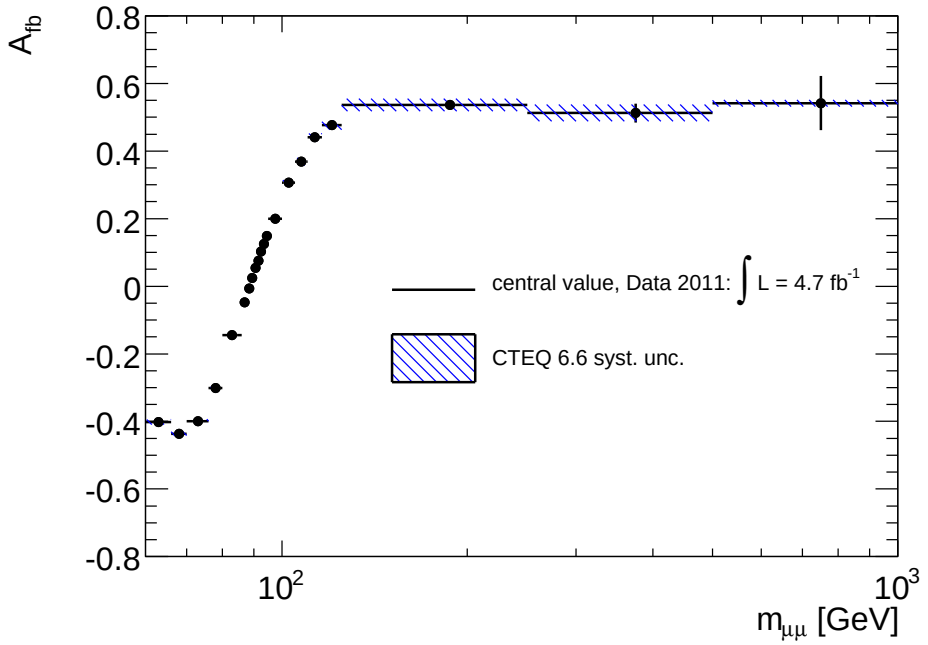

Figure 6.18: A_{fb} distribution with systematic uncertainty due to CTEQ 6.6 PDF error set.

rected A_{fb} data spectrum, is summarized in Tab. 6.4. For data, the statistical and systematic uncertainties are associated to the A_{fb} for each mass bin.

Fig. 6.20(a) (6.21(a)) shows the A_{fb} distribution after mass migration correction (all corrections) applied and it is compared to the Monte Carlo physics-level expectation. In Fig. 6.20(b) (6.21(b)) the difference between the two distributions is shown.

6.8 Extraction of $\sin^2\theta_{eff}$

The forward-backward asymmetry, as discussed in Chap. 1, is a straightforward measurement to prove the existence of New Physics scenarios (cfr. Sec. 1.4.2),

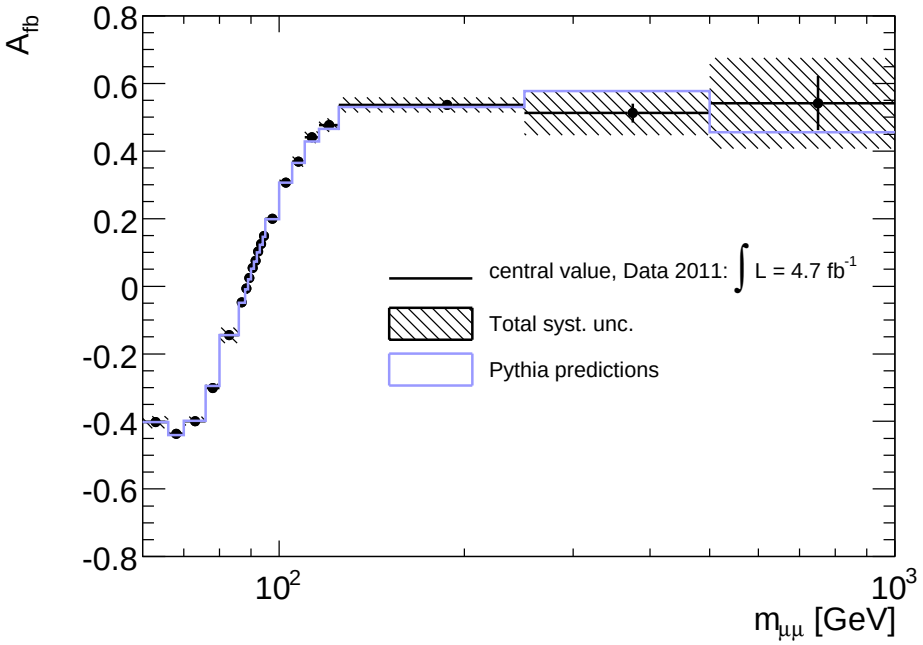

Figure 6.19: A_{fb} distribution with the total systematic uncertainty.

but also to test with extremely high precision the Standard Model fundamental parameters (cfr. Sec. 1.4.1).

Indeed, as Eq. 1.3.15 shows, the axial and axial-vector couplings that appear in the expression of the A_{fb} are directly related to the value of $\sin^2\theta_{eff}$.

Previous experiments have measured $\sin^2\theta_{eff}$ with high precision. The combined uncertainty on $\sin^2\theta_{eff}$ from LEP and SLC experiments is approximately 2.4×10^{-4}. At the Tevatron, with an integrated luminosity of 5 fb^{-1}, the statistical uncertainty is 8×10^{-4} for $\sin^2\theta_{eff}$ [59].

At LHC, with an integrated luminosity of 100 fb^{-1}, it should be possible to measure $\sin^2\theta_{eff}$ with a statistical uncertainty of [60]

$$\Delta \sin^2\theta_{eff} \sim 9 \times 10^{-5} \tag{6.8.1}$$

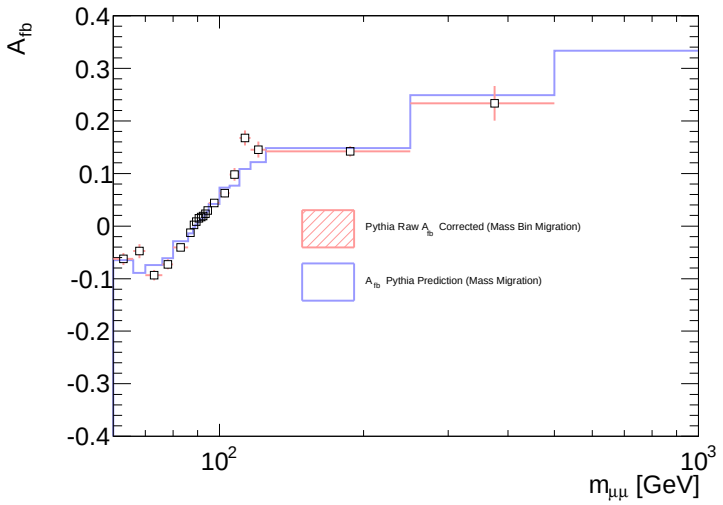

(a) A_{fb} distribution after applying mass bin migration correction

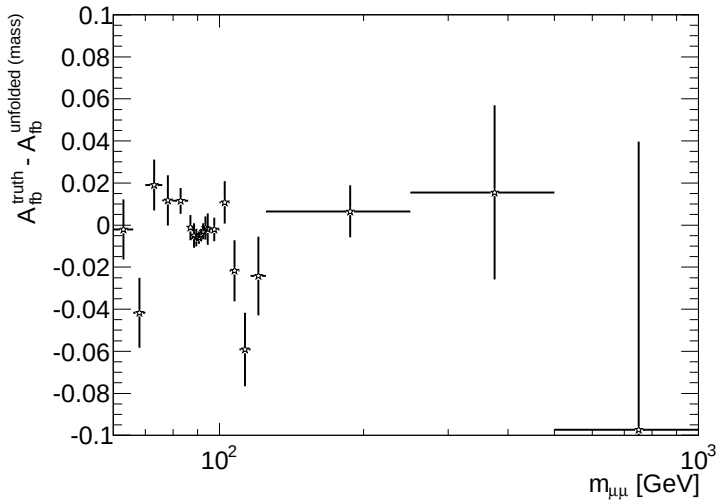

(b) Difference between PYTHIA predicted A_{fb} and A_{fb} corrected for mass bin migration

Figure 6.20: Comparison between PYTHIA predicted A_{fb} and the A_{fb} corrected for mass bin migration (a). In (b) the difference between the two is shown.

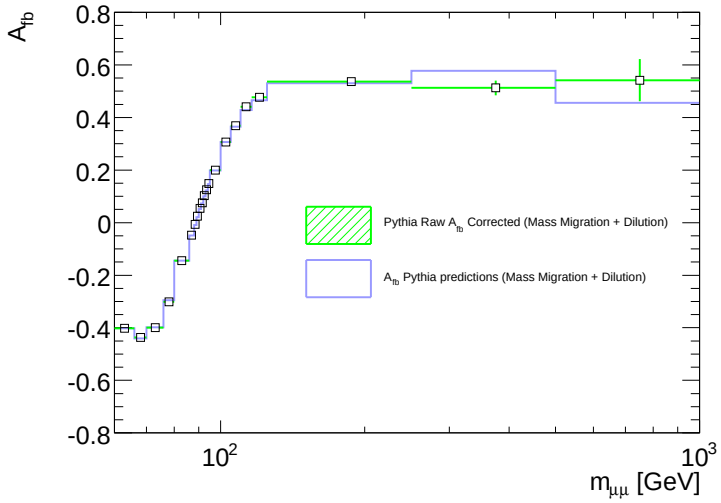

(a) A_{fb} distribution after applying mass bin migration correction and dilution

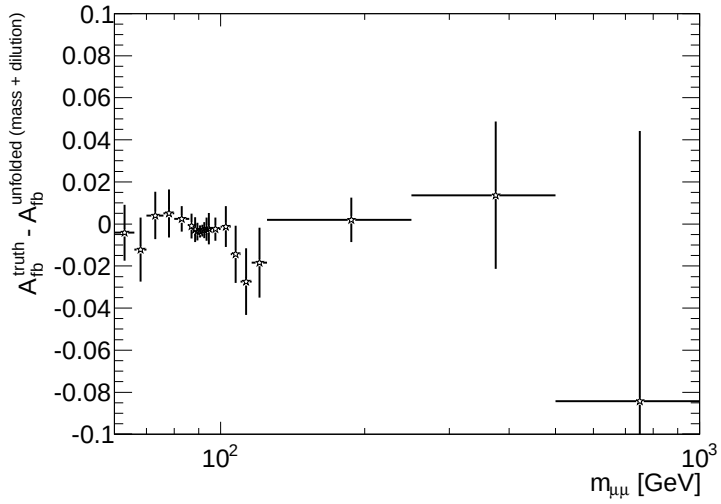

(b) Difference between PYTHIA predicted A_{fb} and A_{fb} corrected for mass bin migration and dilution

Figure 6.21: Comparison between PYTHIA predicted A_{fb} and the A_{fb} corrected for mass bin migration and dilution (a). Plot in (b) shows the difference between the two.

Mass Bin $m_{\mu\mu}$ [GeV]	A_{fb} PYTHIA prediction [MRSTMCal (LO**)]	A_{fb} Data Fully *unfolded*
60 - 66	-0.4017 ± 0.0081	-0.4023 ± 0.0063 ± 0.0179
66 - 70	-0.4410 ± 0.0090	-0.4366 ± 0.0047 ± 0.0115
70 - 76	-0.3982 ± 0.0066	-0.3989 ± 0.0037 ± 0.0125
76 - 80	-0.2951 ± 0.0067	-0.3017 ± 0.0032 ± 0.0126
80 - 86	-0.1442 ± 0.0036	-0.1452 ± 0.0018 ± 0.0231
86 - 88	-0.0490 ± 0.0035	-0.0477 ± 0.0013 ± 0.0043
88 - 89	-0.0089 ± 0.0034	-0.0064 ± 0.0011 ± 0.0171
89 - 90	0.0210 ± 0.0024	0.0243 ± 0.0010 ± 0.0042
90 - 91	0.0515 ± 0.0017	0.0547 ± 0.0009 ± 0.0120
91 - 92	0.0726 ± 0.0016	0.0755 ± 0.0009 ± 0.0214
92 - 93	0.1006 ± 0.0021	0.1032 ± 0.0009 ± 0.0037
93 - 94	0.1227 ± 0.0031	0.1249 ± 0.0010 ± 0.0044
94 - 95	0.1466 ± 0.0041	0.1486 ± 0.0012 ± 0.0088
95 - 100	0.1979 ± 0.0031	0.2001 ± 0.0017 ± 0.0060
100 - 105	0.3059 ± 0.0056	0.3060 ± 0.0030 ± 0.0097
105 - 110	0.3648 ± 0.0078	0.3688 ± 0.0045 ± 0.0152
110 - 116	0.4280 ± 0.0092	0.4407 ± 0.0059 ± 0.0169
116 - 125	0.4658 ± 0.0096	0.4766 ± 0.0066 ± 0.0202
125 - 250	0.5301 ± 0.0063	0.5363 ± 0.0064 ± 0.0226
250 - 500	0.5771 ± 0.0210	0.5125 ± 0.0282 ± 0.0651
500 - 1000	0.4561 ± 0.0833	0.5416 ± 0.0803 ± 0.1346

Table 6.4: Summary of the A_{fb} *unfolded* values, for each mass bin, compared with PYTHIA Monte Carlo expectation. The first uncertainty is statistical (calculated using pseudo-experiments) and the second is systematic.

This estimation has been obtained assuming full rapidity coverage for the muons. In the ATLAS detector, muons can only be detected for pseudorapidities $|\eta| < 2.5$. The finite rapidity range covered by the detector results in a reduction in the asymmetry. As a consequence, the uncertainty expected for $\sin^2\theta_{eff}$ with 100 fb^{-1} increases to

$$\Delta \sin^2 \theta_{eff} \sim 10^{-4} \tag{6.8.2}$$

The $\sin^2\theta_{eff}$ could be measured with different methods:

- a template fit on raw data, using Monte Carlo samples generated with different $\sin^2\theta_{eff}$ values;

- a direct fit of the shape of the asymmetry versus mass of the di-muon pair to its expected value around the Z pole.

With the template fit method, the effective weak mixing angle is extracted from the forward-backward asymmetry measurement without the need to correct the data. This is achieved by comparing the raw data asymmetry distribution to Monte Carlo assuming different values for the weak mixing angle. This comparison is done calculating a χ^2 value between data and Monte Carlo. Its minimum, which corresponds to the most probable value of $\sin^2\theta_{eff}$, is determined by fitting with a second order polynomial the distribution of the χ^2 versus the value of $\sin^2\theta_{eff}$.

The direct fit method requires the fully unfolded asymmetry shape, i.e. it needs correction for both mass bin migration and dilution (as Fig. 6.21(a) shows) and also a further correction to extend the A_{fb} measurement outside the fiducial volume defined by the Z/γ^* candidates event selection. In the following, this correction will be referred to as acceptance correction.

The fully corrected A_{fb} spectrum, including the acceptance correction, could be compared with the following analytical relation in order to directly measure, as a parameter of the fit, the $\sin^2\theta_{eff}$:

$$A_{fb} \equiv \frac{\int_0^1 \frac{\mathrm{d}\sigma}{\mathrm{d}\cos\theta}\,\mathrm{d}\cos\theta - \int_{-1}^0 \frac{\mathrm{d}\sigma}{\mathrm{d}\cos\theta}\,\mathrm{d}\cos\theta}{\int_{-1}^1 \frac{\mathrm{d}\sigma}{\mathrm{d}\cos\theta}\,\mathrm{d}\cos\theta} = \frac{B}{A} \tag{6.8.3}$$

Indeed, the terms A and B in Eq. 6.8.3, already described in Chap. 1 that I rewrite here for convenience:

$$A = Q_l^2 Q_q^2 + 2Q_l Q_q g_{Vq} g_{Vl} Re(\chi(s)) + ({g_{Vl}}^2 + {g_{Al}}^2)({g_{Vq}}^2 + {g_{Aq}}^2)|\chi(s)|^2 \quad (6.8.4)$$

$$B = \frac{3}{2} g_{Aq} g_{Al} (Q_l Q_q Re(\chi(s)) + 2 g_{Vq} g_{Vl} |\chi(s)|^2) \quad (6.8.5)$$

with the term $\chi(s)$ given by

$$\chi(s) = \frac{1}{\sin^2\theta_W \cos^2\theta_W} \frac{s}{s - m_Z^2 + i\Gamma_Z m_Z} \quad (6.8.6)$$

are related to the $\sin^2\theta_{eff}$ through the real effective couplings

$$g_{Vf} = \sqrt{\rho_f}(I_{3f} - 2Q_f \sin^2\theta_{Wf}^{eff}) \quad (6.8.7)$$

$$g_{Af} = \sqrt{\rho_f} I_{3f} \quad (6.8.8)$$

Studies to measure the $\sin^2\theta_{eff}$ with this method are ongoing. Preliminary results show the effectiveness of the method, comparable to those obtained with the template fit procedure.

Chapter 7

Conclusions and Outlook

The subject of this thesis is the measurement of the forward-backward asymmetry, A_{fb}, in $pp \to Z/\gamma^* \to \mu^+\mu^-$ events, at a center-of-mass energy of 7 TeV with about 5 fb^{-1} of data collected with the ATLAS experiment at LHC during the 2011 run. I am the main author of this analysis and I have built all the necessary tools to perform its first measurement in ATLAS.

In Chap. 1, I describe the theoretical framework of the Standard Model, emphasizing the parity violating nature of the electroweak interaction that produces, in the decay of $Z/\gamma^* \to \mu^+\mu^-$ events, an asymmetry in the emission angle of the muon with respect to the incoming quark direction in the rest frame of the Z/γ^*.

After the description of the LHC accelerator and of the ATLAS experiment in Chap. 2 and 3 respectively, I describe in Chap. 4 the procedure to select Z/γ^* candidates and I show the comparison of the Z/γ^* related quantities between collision data and simulated Monte Carlo samples. The differences between data and simulation are accounted for applying proper scale factors

(SFs) to correct the Monte Carlo simulation as described in Chap. 5. Finally, in Chap. 6, I describe in details the analysis to extract the A_{fb} measurement.

First of all, I have measured the *raw* A_{fb} mass spectrum (with no corrections applied) and then I have shown the comparison with the PYTHIA Monte Carlo expectation.

Later on I have described the method I have used to account for the necessary corrections in order to bring the measurement back to the physics level. In fact the measured A_{fb} is affected by the finite detector resolution, by the muon radiative emission and by the dilution due to the lack of knowledge on the direction of the emitted muon relative to the incoming quark. I have adopted a Monte Carlo response-matrix based unfolding and I have used the Bayesian iterative method to regularize the response matrices. Before applying the corrections on real data, I have tested the same techniques on Monte Carlo simulation, with two different Monte Carlo closure tests.

I have also study the systematic uncertainty affecting the asymmetry measurement due to following sources: the algorithm chosen for the unfolding, different Parton Distribution Functions (PDFs) and the limited available Monte Carlo statistics.

As a final result of my thesis, I present the fully corrected A_{fb} measurement versus the di-muon mass, $m_{\mu\mu}$, and I describe a method that I am presently using to extract the $\sin^2\theta_{eff}$. It consists in a direct fit of the shape of the asymmetry versus the mass of the di-muon pairs to its expected value at the Z pole. The ongoing studies show the effectiveness of the method with preliminary results comparable to those obtained with the template fit procedure.

Appendix A

RooUnfold Unfolding Methods

The RooUnfold package provides a common framework to evaluate and use different unfolding algorithms, side-by-side. It currently provides implementations or interfaces for the Iterative Bayes, Singular Value Decomposition, TUnfold methods, as well as bin-by-bin and matrix inversion reference methods.

Some details on each unfolding algorithm are discussed below.

A.1 Iterative Bayesian Theorem

The RooUnfoldBayes algorithm uses the method described by D'Agostini in [58]. Repeated application of Bayes' theorem is used to invert the response matrix. Regularization is achieved by stopping the iteration before reaching the "true" (but wildly fluctuating) inverse. The regularization parameter is just the number of iterations. In principle, this has to be tuned according to the sample statistics and binning. In practice, the results are fairly insensitive

to the precise setting used and four iterations are usually sufficient.

RooUnfoldBayes takes the training truth as its initial prior, rather than a flat distribution, as described by D'Agostini.

A.2 Singular Value Decomposition (SVD)

RooUnfoldSvd provides an interface to the TSVDUnfold class implemented in ROOT by Tackmann [62], which uses the method of Höcker and Kartvelishvili [63]. The response matrix is inverted using singular value decomposition, which allows for a linear implementation of the unfolding algorithm. The normalization to the number of events is retained in order to minimize uncertainties due to the size of the training sample. Regularization is performed using a smooth cut-off on small singular value contributions ($s_i^2 \to s_i^2/(s_i^2+s_i^2)$, where the kth singular value defines the cut-off), which correspond to high-frequency fluctuations.

The regularization needs to be tuned according to the distribution, binning, and sample statistics in order minimize the bias due to the choice of the training sample (which dominates at small k) while retaining small statistical fluctuations in the unfolding result (which grow at large k).

A.3 TUnfold

RooUnfoldTUnfold provides an interface to the TUnfold method implemented in ROOT by Schmitt [64]. TUnfold performs a matrix inversion with 0-, 1-, or 2-order polynomial regularization of neighboring bins. RooUnfold au-

tomatically takes care of packing 2D and 3D distributions and creating the appropriate regularization matrix required by TUnfold.

TUnfold can automatically determine an optimal regularization parameter (τ) by scanning the "L-curve" of $\log_{10}\chi^2$ vs $\log_{10}\tau$.

A.4 Unregolarized Algorithms

Two simple algorithms, RooUnfoldBinByBin, which applies MC correction factors with no inter-bin migration, and RooUnfoldInvert, which performs unregularized matrix inversion with singular value removal (TDecompSVD) are included for reference. These methods are not generally recommended: the former risks biases from the MC model, while the latter can give large bin-bin correlations and magnify statistical fluctuations.

Bibliography

[1] The ALICE Collaboration, *The ALICE experiment at the CERN LHC*, JINST 3 (2008) S08002.

[2] The LHCb collaboration, *The LHCb Detector at the LHC*, 2008 JINST 3 S08005

[3] The ATLAS Collaboration, *The ATLAS Experiment at the CERN Large Hadron Collider*, JINST 3 (2008) S08003;

[4] The CMS Collaboration, *The CMS experiment at the CERN LHC*, JINST 3 (2008) S08004

[5] S.L. Glashow (1961). *Partial-symmetries of weak interactions*. Nuclear Physics 22 (4): 579-588. Bibcode 1961NucPh..22..579G. doi:10.1016/0029-5582(61)90469-2.

[6] S. Weinberg (1967). *A Model of Leptons*. Physical Review Letters 19 (21): 1264-1266. Bibcode 1967PhRvL..19.1264W. doi:10.1103/PhysRevLett.19.1264.

[7] A. Salam (1968). N. Svartholm. ed. Elementary Particle Physics: Relativistic Groups and Analyticity. Eighth Nobel Symposium. Stockholm: Almquvist and Wiksell. pp. 367.

[8] ALEPH Collaboration, Eur. Phys. J. C 14, 1 (2000).

[9] D. Acosta et al.Phys. Rev. D 71, 052002 (2005).

[10] A. Bodek, A simple event weighting technique: Optimizing the measurement of the forward-backward asymmetry of Drell-Yan dilepton and top-antitop pairs at hadron colliders, arXiv:0911.2850v4 [hep-ex].

[11] S.L. Glashow, Nucl. Phys. B22 579 (1961); A. Salam and J.C. Ward, Phys. Rev. Lett. 13 168 (1994); S. Weinberg, Phys. Rev. Lett. 19 1264 (1967).

[12] M. Gell-Mann, Phys. Lett. 8, 214 (1964); G. Zweig, CERN preprint TH401 (1964).

[13] D. Karlen, Plenary talk "Experimental Status of the Standard Model" at the International Conference on High Energy Physics, ICHEP98, Cancouver, July 1998.

[14] K. Nakamura et al. (Particle Data Group), J. Phys. G 37, 075021 (2010) and 2011 partial update for the 2012 edition.

[15] B.W. Le and J. Zinn-Justin, Phys. Rev. D 5, 3121, 3137, 3155 (1972)

[16] G.T. Hooft and M. Veltman, Nucl. Phys. B 44, 189 (1972); Nucl. Phys. B 50. 318 (1972)

[17] F.J. Hasert et al. [Gargamelle Neutrino Collaboration], Phys. Lett. B 46, 138 (1973)

[18] A.C Benvenuti et al., Phys. Rev. Lett. 32, 800 (1974)

[19] M. Holder et al., Phys. Lett. B 71, 222 (1977)

[20] G. Arnison et al., Phys. Lett. 122B, 103 (1983); 126B, 398 (1983); 129B, 273 (1983); 134B, 469(1984); 147B, 241 (1984).

[21] F. Halzen and A D. Martin, Quarks and Leptons: An Introductory Course in Modern Particle Physics, JOHN WILEY & SONS.

[22] D. Perkins, "Introduction to High Energy Physics".

[23] V. Barger and R. Phillips, "Collider Physics", Addison Wesley, 1993.

[24] E. Fermi, Nuovo Cimento 11 (1934); Z. Phys. 88 (1934).

[25] R.M. Barnett et al., Phys. Rev. 54, 1 (1996).

[26] CERN-PPE/95-172, LEP Electroweak Working Group, 1995.

[27] `http://tevewwg.fnal.gov/`

[28] Evans, Lyndon, (ed.) and Bryant, Philip, (ed.), *LHC Machine*, JINST 3 (2008) S08001.

[29] Torbjorn Sjostrand, Stephen Mrenna and Peter Z. Skands. PYTHIA 6.4 Physics and Manual.

[30] J.C. Collins and D.E. Soper, Phys. Rev. D 16, 2219 (1977).

[31] Bodek A 2010 Eur. Phys. J. C67

[32] A. Sirlin, Phys. Rev. D22, 971 (1980); A. Sirlin, Phys. Rev. D29, 89 (1984); D.C. Kennedy et. al., Nucl. Phys. B321, 83 (1989); D.C. Kennedy and B.W. Lynn, Nucl. Phys. B322, 1 (1989); D.Yu. Bardin et. al., Z. Phys. C44, 493 (1989); W. hollik, Fortsch, Phys. 38, 165 (1990).

[33] V.A. Novikov, L.B. Okun, and M.I. Vysotsky, Nucl. Phys. B351, 35 (1993)

[34] G. 't Hooft, Nucl. Phys. B 61, 455â468 (1973); S.Weinberg, Phys. Rev. D 8, 3497â3509 (1973)

[35] G. Degrassi, S. Fanchiotti, and A. Sirlin, Nucl. Phys. B 351, 49 (1991)

[36] D.A Ross and M.J.G Veltman, Nucl. Phys. B95 135 (1975); A. Sirlin, Phys. Rev. D22 971-981 (1980).

[37] The LEP Collaboration ALEPH, DELPHI, L3, OPAL, the LEP Electroweak Working Group, and the SLD Heavy Flavour and Electroweak Groups, LEPEWWG/2003-02, Dec, 2003.

[38] T. Affolder et. al., CDF collaboration, Phys. Rev. Lett. 87, 131802 (2001).

[39] V.M. Abazov, et al, Phys. Rev. Lett. 101, 191801 (2008).

[40] G.P. Zeller et. al., NuTeV Collaboration, Phys. Rev. Lett. 88, 091802 (2002) [Erratumibid. 90, 239902 (2003)].

[41] F. Del Aguila, M. Quiros and F. Zwirner, Nucl. Phys. B 287, 419 (1987); J. L. Rosner, Phys. Rev. D 35, 2244 (1987); J. L. Rosner, Phys. Rev. D 54, 1078 (1996).

[42] H. Georgi and S.L. Glashow, Phys. Rev. Lett. 32, 438 (1974).

[43] H. Georgi in Proceedings of the 1974 Williamsburg DPF Meeting, ed. by C.E. Carlson (New York, AIP, 1975) p. 575; H. Fritzch and P. Minkowski, Ann.Phys.(N.Y.) 93, 192 (1975).

[44] J.L. Hewett and T.G. Rizzo, Phys. Rept. 183, 193 (1989).

[45] A. Leike, Phys. Rept. 317, 143 (1999).

[46] Rosner, J.L.: Phys. Rev. D 54, 1078 (1996)

[47] S. Myers. The LEP collider, from design to approval and commissioning. Presented at CERN Accelerator School: The LEP Collider from Design to Approval and Commissioning, Geneva, Switzerland, Nov 26, 1990, CAS: CERN accelerator school, 6th John Adams Memorial lecture.

[48] The ATLAS Collaboration, G. Aad et al., *Expected Performance of the ATLAS Experiment: Detector, Trigger and Physics*, CERN-OPEN 2008-020.

[49] The ATLAS Collaboration, G. Aad et al., *The ATLAS Muon Spectrometer Technical Design Report*, CERN/LHCC/97-22.

[50] J.M. Campbell, J.W. Huston, and W.J. Stirling. Hard Interactions of Quarks and Gluons: a Primer for LHC Physics. Rept.Prog.Phys., 70:89, 2007.

[51] The ATLAS Collaboration, G. Aad et al., *Luminosity Determination in pp Collisions at* $\sqrt{s}$ *= 7 TeV using the ATLAS Detector in 2011*, ATLAS-CONF-2011-116 JHEP, 05:026, 2006.

[52] Piotr Golonka and Zbigniew Was. PHOTOS Monte Carlo: A Precision tool for QED corrections in Z and W decays. Eur. Phys. J., C45:97â107, 2006.

[53] S. Agostinelli et al. GEANT4: A simulation toolkit. Nucl. Instrum. Meth., A506:250â303, 2003.

[54] Groom D.E. et al. Eur. Phys. J., C15:1, 2000.

[55] The ATLAS Collaboration, G. Aad et al., *Muon reconstruction efficiency in reprocessed 2011 LHC proton-proton collision data recorded with the ATLAS detector*.

[56] The ATLAS Collaboration, G. Aad et al., *ATLAS Muon Momentum Resolution in the First Pass Reconstruction of the 2010 p-p Collision Data at* $\sqrt{s}$ *= 7 TeV*, ATLAS-CONF-2011-046

[57] T. Adye, *Unfolding algorithms and tests using RooUnfold*, arXiv:1105.1160v1.

[58] G. D'Agostini, *A Multidimensional unfolding method based on Bayes' theorem*, Nucl. Instrum. Meth. A362 (1995) 487-498.

[59] V. M. Abazov *et al.* [D0 Collaboration], Phys. Rev. D **84** (2011) 012007.

[60] U. Baur, S. Keller, and W. Sakumoto, *QED radiative corrections to Z boson production and the forward-backward asymmetry at hadron colliders*, Phys. Rev. D 57 (1998) 199-215.

[61] P. Nadolsky et al., Implications of CTEQ global analysis for collider observables.

[62] K. Tackmann, *SVD-based unfolding: implementation and experience*, presented at PHYSTAT 2011 (CERN, Geneva, January 2011), to be published in a CERN Yellow Report

[63] A. Hocker and V. Kartvelishvili, *SVD Approach to Data Unfolding*, Nucl. Instrum. Meth. A 372 (1996) 469.

[64] The TUnfold package is available in ROOT [66] and documented in `http://www.desy.de/~sschmitt/tunfold.html`

[65] M. Herrero, "The Standard Model", hep-ph/9812242.

[66] R. Brun and F. Rademakers, *ROOT: An object oriented data analysis framework*, Nucl. Instrum. Meth. A 389 (1997) 81. See also `http://root.cern.ch/`

Aknowledgements

At the end of this manuscript, I would like to say few words of thanks to those who have always supported and encouraged me.

First of all, I would like to express my gratitude to Prof. Anna Di Ciaccio, for her precious advice and her constant presence during these years of work and, last but not least, for her patiently correction the first drafts of this manuscript.

Moreover, I would like to thank all the members of the ATLAS Tor Vergata group who have shared with me difficult and successful episodes of our project.

I am particularly grateful to Andrea Di Simone, who followed me during my research activity and that has always been ready to dispel my doubts in the drawing up of this thesis.

Special thanks are due to Roberto Di Nardo, Barbara Liberti and Giulio Aielli, for their precious collaboration and friendship in the last years.

I thank all the professors, in particular Prof. Rinaldo Santonico, colleagues and friends met in recent years and with whom I was able to confront and grow from both the professional and personal point of view: I am very happy to have worked with you.

Dr. Bogdan Malaescu deserves all my gratitude for his helpful hints in the

use of RooUnfold.

Finally, my gratefulness goes to my family and my friends, for their love, friendship and patient support without which I would never achieve this result.

To get to this point will, commitment and hard work have been necessary so let me ask one last thank to myself, accompanied by the promise that I will not stop here and I will continue to pursue more ambitious objectives and results: this thesis, in fact, is not only the conclusion of a journey, but also the introduction to my future.